Photo-Assisted Etching in Halogen Containing Plasmas

A Dissertation

Presented to

The Faculty of Department of Chemical and Biomolecular Engineering

University of Houston

In Partial Fulfillment of

the Requirements for the Degree

Doctor of Philosophy

in

Chemical Engineering

By

Shyam Sridhar

August 2016

Photo-Assisted Etching in Halogen Containing Plasmas

_____

Shyam Sridhar

Approved:

_____

Co-chair of the Committee
Dr. Demetre J. Economou, Professor,
Chemical and Biomolecular Engineering

_____

Co-chair of the Committee
Dr. Vincent M. Donnelly, Professor,
Chemical and Biomolecular Engineering

Committee Members:

_____

Dr. Peter Vekilov, Professor
Chemical and Biomolecular Engineering

_____

Dr. Jeffrey Rimer, Associate Professor
Chemical and Biomolecular Engineering

_____

Dr. Jiming Bao, Associate Professor
Electrical and Computer Engineering

_____

Dr. Paul Ruchhoeft, Associate Professor
Electrical and Computer Engineering

_____

Dr. Suresh K. Khator, Associate Dean
Cullen College of Engineering

_____

Dr. Michael P. Harold, Professor, Chair
Chemical and Biomolecular Engineering

Acknowledgements

I would like to express my deepest gratitude to my advisors Dr. Vincent Donnelly and Dr. Demetre Economou for their support, guidance, and encouragement throughout my graduate studies. I feel honored to be associated with two great stalwarts in the field of plasma processing. Their advice and guidance, both academic and non-academic, have been invaluable and is something that will be treasured for life.

I am very grateful to my fellow lab mates, Lei Liu and Dr. Weiye Zhu, for the great team effort. Their ideas and contributions have played a huge rule in shaping this dissertation. I would also like to thank former post-doctoral researchers Dr. Hyungjoo Shin, Dr. Erdinc Karakas, and Dr. Vladimir Samara for their advice and support at various times in the last few years. I also acknowledge former and current lab members: Dr. Ashutosh Srivastava, Dr. Siyuan Tian, Dr. Carol Chen, Dr. Paola Diomede, Sanbir Kaler, Qiaowei Lou, Tianyu Ma, Tyler List, and Eduardo Hernandez. It was a great pleasure working in the lab with them. I will cherish the fun times that made graduate school less stressful.

I would like to thank Dr. Peter Vekilov who has served on my committee since my PhD qualifying exam. He was very appreciative and provided valuable insights. I also thank Dr. Jeffrey Rimer, Dr. Paul Ruchhoeft, and Dr. Jiming Bao for being a part of my dissertation defense committee.

I would also like to acknowledge the department staff for their help and assistance on various issues. The administrative staffs (Ms. Patricia Cooks, Ms. My Dung-Lieu Ms.

Pamela Moses, Ms. Nicolette Solano, Ms. Yolanda Thomas, and Ms. Hira Ahmed) were very helpful and prompt in processing purchases, reimbursements, and paperwork. Special thanks to Mr. David Dawlearn for emphasizing on lab safety and reminding me to wear safety goggles. I would also like to thank all the machinists I worked with: Mr. Gerald Blosser, Mr. Mitchel Hawkins, and Mr. John Costales. None of the experiments would have been possible without their machine work.

Finally, I thank my parents and my sister for their selfless love, understanding, and encouragement. None of this would have been possible without their support.

Photo-Assisted Etching in Halogen Containing Plasmas

An Abstract

of a

Dissertation

Presented to

The Faculty of Department of Chemical and Biomolecular Engineering

University of Houston

In Partial Fulfillment of

the Requirements for the Degree

Doctor of Philosophy

in

Chemical Engineering

By

Shyam Sridhar

August 2016

Abstract

Plasma etching is indispensable in microelectronics manufacturing, due to its ability to precisely pattern feature with lateral dimensions of <10 nm. To advance this capability to etch layers with atomic fidelity, while also achieving ultra-high material selectivity, low ion energies (10s eV) are required. However, at low ion energies, an alternative etching pathway catalyzed by vacuum ultraviolet (VUV) photons generated in the plasma has been shown to be very important.

In this thesis, photo-assisted etching (PAE) was studied in various halogen containing plasmas. Cl_2, Br_2, HBr, Br_2/Cl_2, and HBr/Cl_2 feed gases diluted in Ar (50%–50% by volume) were used to study etching of p-type Si(100) in a radio frequency, inductively coupled, Faraday-shielded plasma. PAE was observed in all cases, with Br_2/Ar and HBr/Cl_2/Ar plasmas having the lowest and highest PAE rates, respectively. Etching rates measured under MgF_2, quartz, and opaque windows showed that high energy VUV photons are more effective in inducing PAE compared to low energy photons. Characterization of etched surfaces using Scanning Electron and Atomic Force Microscopy (SEM and AFM) revealed that photo-etched surfaces were rough, quite likely due to the inability of the photo-assisted process to remove contaminants from the surface. PAE in Cl_2/Ar plasmas resulted in the formation of 4-sided pyramidal features with bases that formed an angle of 45° with respect to <110> cleavage planes, suggesting that the PAE is sensitive to crystal orientation.

Various mechanisms have been proposed to explain photo-assisted etching of Si, including photo-generated carrier-mediated etching, and photon-induced damage (breaking of Si-Si bonds) caused by VUV photons irradiating the substrate. Optical Emission Spectroscopy was used to gain an insight into possible in-plasma PAE mechanisms. Emissions from Cl, Si, SiCl, and Ar were recorded as a function of power while etching p-Si in a 50%Cl_2/50%Ar plasma at a pressure of 60 mTorr with no substrate bias. The Si:Ar optical emission intensity ratio, I_{Si}/I_{Ar}

(proportional to the etching rate of Si), increased substantially with power. Accounting for the contribution to this signal from the dissociation of $SiCl_x$ (x=1-3) etch products, the residual increase in the emission indicated that the photo-assisted etching rate also increased with power. Time resolved emissions were also recorded in a pulsed plasma where power was modulated between 500W and 300W. I_{Si}/I_{Ar} was found to modulate with the instantaneous power. This rules out the photon-induced damage mechanism since, if this mechanism was dominant, the I_{Si}/I_{Ar} signal would not be modulated.

Table of Contents

List of Figures

List of Tables

Chapter 1 – Introduction

1.1 Plasmas in semiconductor processing

Plasmas have long been used in the semiconductor industry to deposit and remove material from the wafer surface. These processes are essential for the fabrication of nanoscale electronic devices. Etching in particular is a critical step in the fabrication of integrated circuits, allowing fine lithographic patterns to be precisely transferred onto thin films on a wafer. Plasma etching or reactive ion etching (RIE) occurs through a synergy between plasma driven chemical reactions and bombardment of ions normal to the wafer surface [1]. The directional nature of ions striking the wafer being etched gives rise to anisotropic etch profiles and precise pattern transfer.

The semiconductor industry is primarily driven by Moore's law: the number of transistors in an integrated circuit doubles every two years [2]. Continuation of Moore's law requires further shrinking of device feature sizes to < 10 nm and the use of advanced 3D circuit architectures among other solutions. These requirements pose a great challenge to existing plasma etching processes, especially with respect to achieving dimensional control on the order of a few Angstroms. Advanced control of etching precision potentially offered in techniques such as atomic layer etching (ALE) is needed to allow etching of ultrathin films with monolayer accuracy and no damage to underlying materials [3], [4].

Critical variables that determine the feasibility of ALE include: (i) the choice of the reactive gas, and (ii) energy of bombarding ions that assist in the chemical reaction

between the reactive gas and the substrate material being etched and desorption of etch products [3], [4]. The gas is chosen such that it does not spontaneously etch the material. This limitation can be overcome to some extent by reducing the temperature of the substrate to slow down the kinetics of the reaction between the reactive gas and the substrate material [4]. The ion energy must not be too high to damage the underlying crystalline substrate by physical sputtering nor too low to drive a synergistic etching reaction on the surface. The ion energy must be controlled so that the atomic layer etching process is self-limiting, i.e., no etching occurs in the absence of ion bombardment or when the reactive layer formed at the surface of the material being etched has already been removed by ion bombardment.

1.2 Control of the Ion Energy Distribution

Control of the ion energy distribution (IED) is one key to improving the precision of plasma etching processes. For ALE, mono-energetic IEDs are most desirable. Various methods have been reported to obtain nearly mono-energetic IEDs [5]–[7]. One such technique employs a Faraday shielded, inductively coupled plasma (ICP), where the power was modulated at 10 kHz with a duty cycle of 20% [8]. A synchronously pulsed DC bias (+24.4 V) was applied on a boundary electrode during the afterglow (power OFF) period. Figure 1.1 shows the time-averaged ion energy distribution. The narrow peak centered at ~24 V corresponds to the ion energy during the afterglow period when the pulsed DC bias was applied on the boundary electrode, whereas the short and broad peak corresponds to the energy of the ions when the plasma is ON. The position of the

nearly mono-energetic peak may be varied by changing the magnitude of the DC bias applied on the boundary electrode.

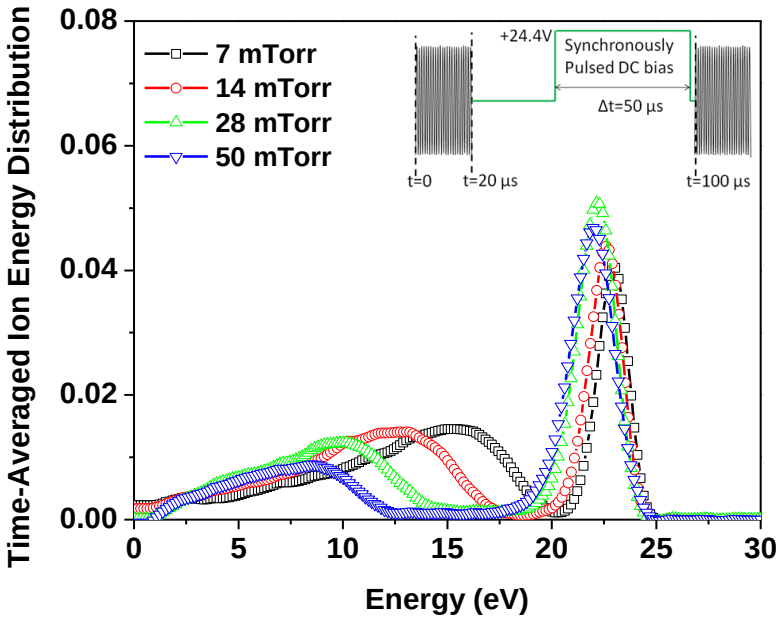

Figure 1.1: Control of ion energy distribution using a pulsed plasma and a synchronously biased boundary electrode [8].

1.3 Discovery of Photo-Assisted Etching in plasmas

Lowering the ion energy reduces ion assisted etching rates substantially. Low ion energies facilitate damage free, selective etching of materials. While studying etching of p-type silicon in a dilute Cl_2/Ar plasma using a nearly mono-energetic ion energy distribution, it was found that etching persisted at ion energies below the threshold for ion assisted etching (see Fig. 1.2). Experiments ruled out the possibility of etching by low energy ion assisted process and also by Ar metastables, which possibly have sufficient energy to promote etching. Reduction of the sub-threshold etching rate under a quartz window (which has a light transmission cutoff wavelength of ~170 nm) suggested that

vacuum ultra-violet (VUV) photons generated in the plasma played a major role in sub-threshold etching of silicon [9].

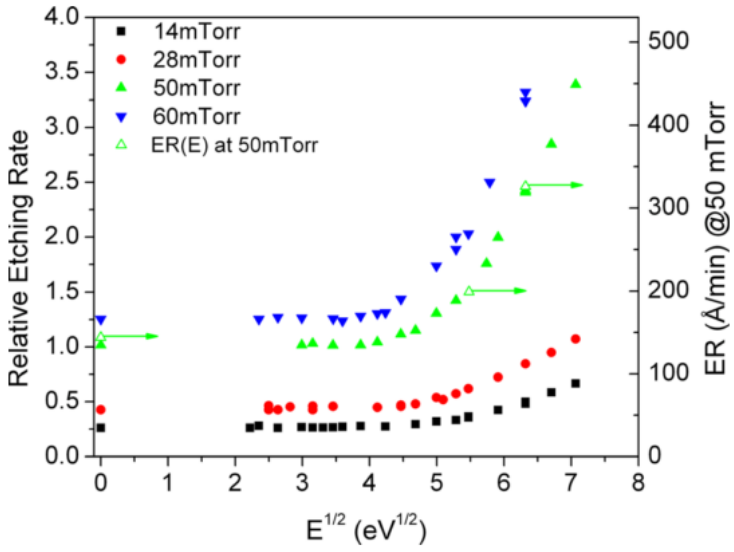

Figure 1.2: Silicon etching as a function of square root of ion energy in 1%Cl_2/99% Ar plasma. Sub threshold photo-assisted etching observed for ion energies less than 16eV [9].

Sub-threshold photo-assisted etching can be detrimental to processes that employ low ion energy to achieve high selective and low damage. The importance of photo-assisted etching as a competing etching mechanism at low ion energies could prove to be a major obstacle in the development of self-limiting etching processes such as atomic layer etching [3]. Hence it is imperative to understand the nature of plasma surface interactions, specifically regarding the role played by VUV photons. A mechanistic insight into photo-assisted etching mechanisms may provide clues to reduce photo-assisted etching relative to ion assisted etching.

Chapter 2 - Literature Review

2.1 Role of photons in etching

A material is etched when the reactive species adsorbs on the surface, reacts with it and the reaction products subsequently desorb. The etching rate is determined by the slowest of these processes. In reactive ion etching or plasma etching, energetic ion bombardment drives surface reactions by breaking bonds and assisting in desorption of the reaction products from the surface of the material. Similarly, energetic photons could induce reactions and promote desorption of the reaction products by direct or indirect excitation [10]. Direct excitation could involve excitation of gas phase species as well as species adsorbed on the surface. A high energy photon can excite a molecule in the gas phase (electronic excitation), often leading to dissociation, or interact with the species adsorbed on the surface causing the adsorbed species to break the bonds formed on the surface and desorb into the gas phase. Indirect excitation occurs through processes initiated by absorption of light by the substrate material [11]. For semiconductor materials, absorption of photons with energies larger than the band gap creates electron-hole pairs. These photo-generated carriers can have sufficient initial energy to enhance surface reactions [10].

Photons may play a significant role in aiding or enhancing either of the basic processes involved in etching (i.e., adsorption of reactive species, reaction at the surface, desorption of reaction product). To understand photo-assisted etching, it is important to

understand the fundamental mechanisms by which the photon influences these basic processes.

2.2 Photon interaction with gas phase species

Reactive gas molecules (e.g., Cl_2) can be excited and often dissociated by photons through electronic excitation. Photo-dissociation produces more reactive radicals [12]. Reactions involving the substrate with reactive gas molecules that may otherwise be endothermic are made possible through the formation of radicals. Excitation of gaseous species is an important phenomenon in laser induced etching, specifically when etching rate is governed by the flux of reactive atomic radicals that are produced by photon induced dissociation [13]. In a plasma, molecules are dissociated by electron impact and contributions to dissociation/excitation due to light absorption are generally thought to be negligible.

2.3 Direct excitation of the adsorbate

A photon can be absorbed by the adsorbate species through electronic transitions. The excited adsorbate can participate in any of the multiple relaxation processes. The excited species may have sufficient energy to enhance adsorbate-adsorbate, or adsorbate-adsorbent chemical interactions, break surface bonds, and desorb (etching reactions) or lose energy by relaxation processes in the adsorbate layer itself or to the underlying substrate. Relaxation processes include intralayer energy redistribution, coupling to electronic states of the substrate, or quenching in the substrate lattice. The probability that the excited species participate in any surface reaction depends on the time for which it

will stay excited. Adsorbate vibrational energy relaxation times have been measured using pulsed laser techniques [14]. For semiconductors, it has been determined that the lifetime of vibrationally excited species is less than 10 ps, if the vibration frequency is less than Debye frequency of substrate. For excitation frequency larger than the Debye frequency, relaxation requires non-resonant multi-phonon interactions resulting in larger lifetimes (> 50 ps) [15].

Laser induced etching of Si using SF_6 was attributed to direct excitation of adsorbed SF_6 [16]. Laser pulses from a CO_2 laser directed towards a silicon substrate saturated with 1-2 monolayers of physisorbed SF_6, were shown to drive a surface reaction between the adsorbed gas molecules and silicon substrate. The major product of the reaction (SiF_4) desorbing from the surface was detected by a mass spectrometer. It was shown that the surface reactions leading to etching (see below) was mainly due to the vibrationally excited SF_6^* formed by multiple photon absorption, as proposed in the following mechanism:

$$SF_6^* - Si\ (s) \rightarrow SiF_2\ (ads) + SF_4\ (g), \tag{2.1}$$

$$SiF_2 + SiF_2 \rightarrow SiF_4\ (ads) + Si, \tag{2.2}$$

$$SF_6^* + SiF_2 \rightarrow SiF_4\ (ads) + SiF_4\ (g), \text{ and} \tag{2.3}$$

$$SiF_4\ (ads) \rightarrow SiF_4\ (g). \tag{2.4}$$

Etching diminished substantially when the light was focused parallel to the silicon substrate due to the lack of reactive species. Absorption of intense infrared radiation by

the silicon substrate may also induce substrate lattice vibrations, and rearrangement of surface species in a way that assists in desorption of reaction products (equation 2.2).

2.4 Photon interaction with the substrate

In semiconductor materials, absorption of photons that have energy larger than the band gap leads to the formation of electron-hole pairs that have an excess kinetic energy equivalent to the difference between the band gap (E_g) and photon energy ($h\nu$). The cross section for this absorption is determined by the electronic band structure (direct or indirect band gap) of the material. The energetic photo-generated carriers can induce chemical reactions equivalent to oxidation (detachment of electron) or reduction (addition of electrons) reactions on the surface. Photo-generated carriers may also enhance adsorption of gas molecules on the surface as is known to occur for O_2 molecules on TiO_2 [17]. Examples of carrier mediated processes are discussed in section 2.6.

2.4.1 Creation of charge carriers

Photons with energy smaller than the band gap ($h\nu < E_g$) are not absorbed by the material, i.e., no electronic transitions occur from the valence band to the conduction band. However, intra-band free carrier transitions may occur at low photon energies where free carriers in the valence or conduction band absorb photon energy and are excited to higher energy level within the same band [18]. For photon energies just above the band gap, the electronic transition will be “direct” or “indirect”, depending on the material. For semiconductors with an indirect band gap (e.g., Si), the electronic transition from valence to conduction band also requires absorption of a phonon in order to change

the momentum of the valence band electron. Phonons are quanta of lattice vibration that have a very small energy and a large momentum. For an electronic transition to occur, the phonon must have a momentum vector in the same direction as the electronic transition. Also, since the phonons have a small but finite amount of energy, indirect transitions can occur at photon energies just below band gap energy. The requirement of lattice phonons for the "indirect" electronic transition to occur reduces the probability of light absorption through this mechanism compared to "direct" transitions. At photon energies larger than the "direct" band gap energy (3.3 eV for Si [19]), direct electronic transitions can occur, increasing light absorption.

Figures 2.1 and 2.2 show the absorption coefficient of silicon as a function of wavelength [20]. The attenuation of light due to absorption by the material can be expressed by the Beer-Lambert's equation

$$I(x) = I_o e^{-\alpha x}, \tag{2.5}$$

where I(x) denotes the intensity of light at a depth x from the surface of the material, α is the absorption coefficient of the material which depends on the wavelength of light being absorbed. For '1/e' drop in the light intensity, the penetration depth is equal to inverse of the absorption coefficient. The absorption coefficient of silicon is quite high for high energy photons, resulting in short penetration depths. For example, photons with wavelengths of 120 - 200 nm penetrate to a 1/e depth of 6 – 8nm, respectively.

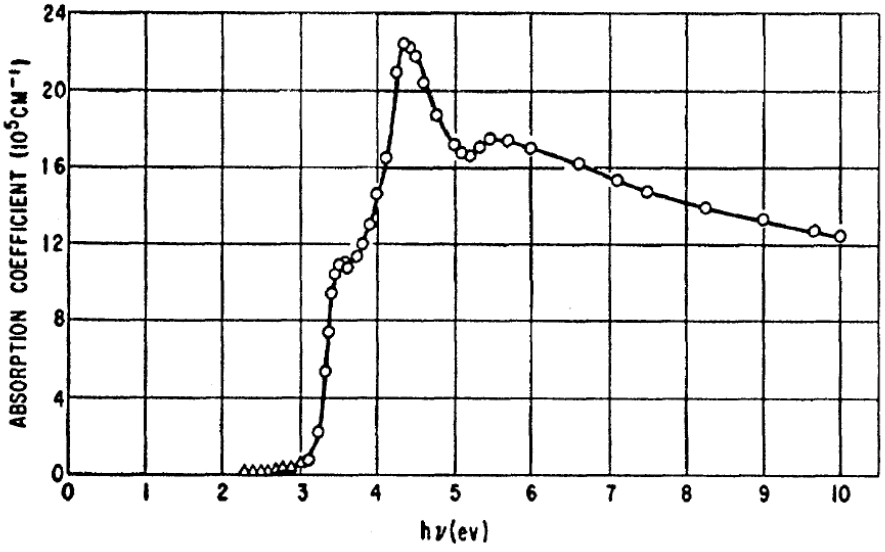

Figure 2.1: Absorption coefficient of silicon for photon energies greater than 2 eV [20].

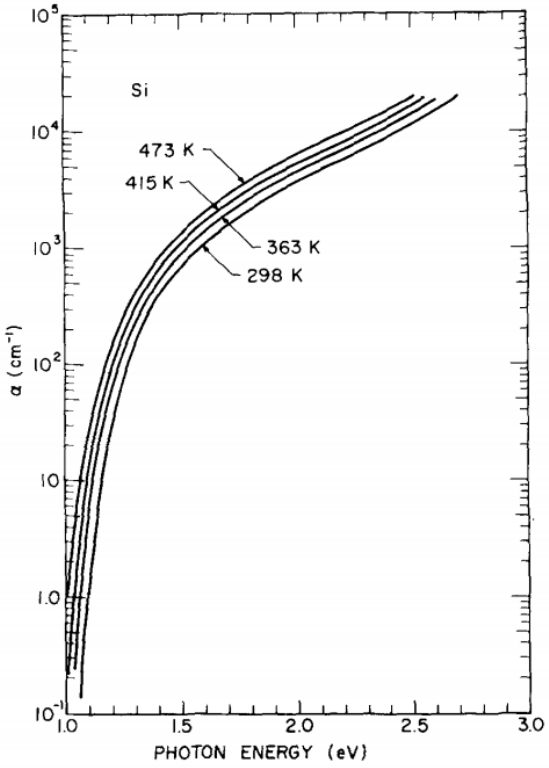

Figure 2.2: Absorption coefficient of silicon for photon energies less than 2.5 eV [21].

2.4.2 Loss of excess carrier energy

The energetic photo generated carriers lose energy through their interaction with phonons (carrier – phonon scattering). The time for this relaxation (t_{relax}) is weakly dependent on the energy of hot carriers for energies < 1eV [22], and is between 0.1 – 1 ps for low doping levels ($<10^{17}$ cm^{-3}) for which carrier-carrier collisions are negligible [23]. For high excitation densities larger than the background doping level, carrier-carrier collisions cannot be neglected [24]. However, carrier-carrier scattering does not serve to decrease the excess energy as both carriers involved in the collision are energetic. Hot carriers tend to diffuse through the lattice with an ambipolar diffusion coefficient (due to charge neutrality in the bulk) that is determined by the carrier phonon scattering. The photo generated carriers lose their excess kinetic energy rapidly and return to the band edge. Diffusion or carrier migration to the surface induced by band bending continues to occur simultaneously as the carriers lose energy and return to the band edge. Typical diffusion coefficient for a hole in p type Si at 300K in the absence of electric field is about 10 cm^2/s [25]. The distance that the energetic minority covers by diffusion in ~ 0.5 ps (the time it takes for the carrier to lose its excess energy) may be estimated (using equation 2.7 discussed below) to be ~ 20 nm.

2.4.3 Carrier Diffusion

Carriers continue to diffuse until they are lost by recombination. The diffusivity (*D)* of the charge carriers can be calculated from Einstein's relation [26]

$$D = \frac{kT\mu}{q}, \tag{2.6}$$

where k is the Boltzmann's constant, T is the substrate temperature, μ is the carrier (electron or hole) mobility, and q is electronic charge. Carrier diffusion is mainly a function of the internal/external electric field and temperature. At low fields, diffusion is nearly independent of the field, whereas high fields result in lower diffusivity [27]. Lower diffusivity at high temperature arises due to increased collisionality with the lattice. Diffusion length (Λ_{diff}) may be estimated as

$$\Lambda_{diff} = \sqrt{D t_{recomb}}, \tag{2.7}$$

where t_{recomb} is the carrier lifetime before they are lost by recombination.

2.4.4 Carrier loss by recombination

Recombination in the bulk occurs through one of the following mechanisms:

i) **Trap assisted Shockley-Read-Hall recombination** [28] – The presence of impurities (or dopants) in the lattice creates a localized trap state in the band gap, where an electron may be trapped. If a hole is also trapped before the electron moves into the conduction band, recombination occurs in the trap state. (Fig. 2.3(a)) The energy released due to recombination is transferred to the lattice.

ii) **Radiative recombination** [29] – This mode is accompanied by the emission of a photon with energy that corresponds to the energy release by recombination (Fig. 2.3(b)). This is not important for Si due to the indirect band gap.

iii) **Auger recombination** [30] – Three carriers are involved in this recombination process. A second electron or hole is excited by absorbing the energy released in the recombination process. The electron loses this energy eventually through a

series of collisions with the lattice. (Fig. 2.3 (c)) This mode is dominant in heavily doped materials and for high carrier densities.

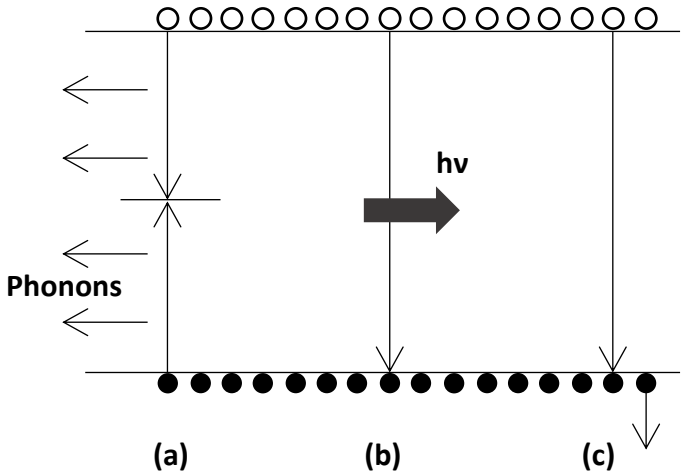

Figure 2.3: Different modes of recombination. (a) Shockley Read Hall Recombination, (b) Radiative Recombination, and (c) Auger Recombination.

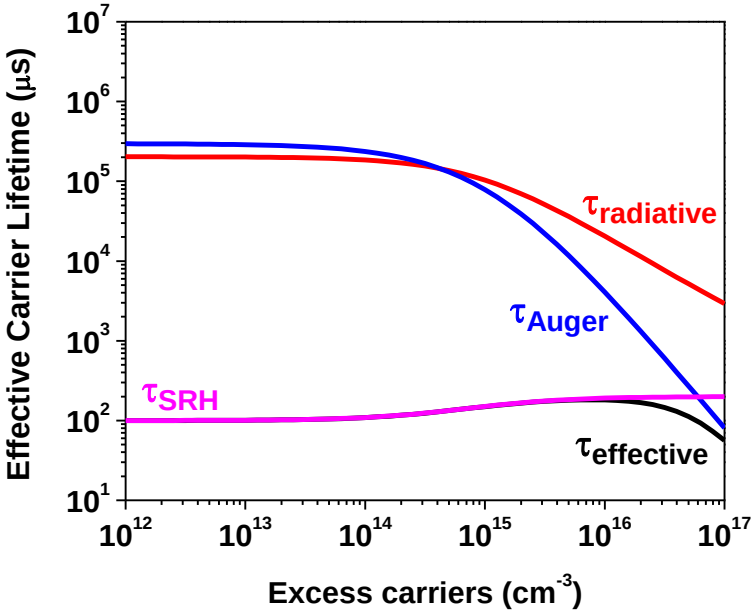

Figure 2.4: Effective carrier lifetimes as a function of excess carrier density in p-Si with a acceptor density of 10^{15} cm^{-3}[31].

The effective carrier lifetimes (not including surface recombination) as a function of excess carrier density is shown in Fig. 2.4 for a p-type silicon with an acceptor density of 10^{15} cm^{-3} [31]. The carrier lifetimes were computed using models from literature (Radiative recombination - Trupke et al. [32], Auger recombination - Richter et al. [30], SRH recombination - SRH equation [33] using a 100 μs lifetime for holes (τ_{po}) and electrons (τ_{no}) at low doping levels. Apparently, SRH mechanism is the most important carrier recombination mechanism in the bulk. At large induced carrier densities (>10^{17} cm^{-3}) the carrier lifetime is decided by Auger recombination.

2.4.5 Effect of Surface States

In addition to the bulk recombination processes discussed above, recombination can also occur at the surface. Due to abrupt termination of the lattice at the surface, electrically active sites (surface states) are created which act as recombination traps. Also, the surface is prone to contamination due to reaction with other species, or by damage from ion bombardment in a plasma. Surface states present at mid gap can act as recombination centers similar to SRH recombination. Surface recombination can reduce the lifetime of carriers significantly. It is also possible that the energy released on recombination can create a localized hot spot, promoting surface reactions or favoring desorption of surface species. The effective lifetime of the photo generated carriers before they recombine through any of the above mechanisms can be calculated as

$$\frac{1}{\tau_{effective}} = \frac{1}{\tau_{radiative}} + \frac{1}{\tau_{Auger}} + \frac{1}{\tau_{SRH}} + \frac{1}{\tau_{surface}}. \quad (2.8)$$

Surface recombination velocity depends on the quality of the surface. Surface passivation has been shown to increase carrier lifetimes. Si wafer pre-treatment using HF results in the formation of covalent Si-H bonds on the surface leaving no dangling bonds on the surface [34]. Low surface recombination velocity (~ 0.25 cm/s) observed on a HF treated Si surface has been attributed to the lack of dangling bonds on the surface which would otherwise act as recombination centers [35]. On the other hand surface damage can reduce carrier lifetimes. Kumaravelu et al. studied the effect of plasma induced damage on surface recombination velocities [36]. A textured silicon wafer was etched in a SF_6 plasma in reactive ion etch mode with the plasma operated at 200 W RF power (13.56 MHz) with RF biasing of the substrate (V_{dc} = -105 V). The minority carrier lifetimes measured after etching was substantially lower (nearly zero) compared to the lifetimes before etching. The very high carrier surface recombination rates were attributed to the damage caused by energetic ion bombardment. The plasma etching step was followed by a wet etch step where the plasma induced damage layer was etched away. It was found that removal of 2-3 μm of this damaged layer recovered the carrier lifetimes substantially [36].

2.4.6 Band Bending due to Surface States

Surface states can be “donor-like” or “acceptor-like” states depending on the position with respect to Fermi level. For an “acceptor like” surface state in n-doped semiconductor, electrons transfer from the bulk to the surface region, rendering the surface more negative compared to the bulk [37]. The formation of this space charge layer sets up an electric field, causing the bands to bend. At equilibrium, the strength of

the electric field is such that it opposes any further transfer of electrons from the bulk to the surface [38]. Typically, the density of surface states (10^{15} cm^{-2}) is much higher than the bulk dopant states, causing a pinning of the Fermi level by surface states [39]. Band bending can drastically reduce surface recombination rates as the band bending in the space charge layer imposes an energy barrier on the majority carriers to keep them from reaching the surface (see Fig. 2.5). Assuming the thickness of the semiconductor is much larger than depletion width (W), a 1-D Poisson's equation may be used to estimate W [39]

$$W = \sqrt{\frac{2\varepsilon_r \varepsilon_0 V}{eN}}, \tag{2.9}$$

where ε_r is the dielectric constant of the material, ε_o is the permittivity of free space, V is the energy barrier due to band bending, e is the elementary charge and N is the dopant density. It can be easily shown that the depletion width for Si with a dopant level of 10^{15} cm^{-3} ~ 800 nm. Comparing this with the penetration depth of a VUV photon (8nm), it is obvious that the transport of photo generated carriers will be influenced by the surface electric field.

When the surface is irradiated by photons with energy larger than the band gap, charged carriers are created. The photo-generated carriers move in different directions due to the nature of band bending. For the n-doped semiconductor with "acceptor-like" surface states considered above, the minority carriers (holes) move towards the surface aided by band bending, while electrons are pushed into the bulk. With increasing density of holes at the surface, the excess negative charge at the surface is neutralized, causing

the bands to flatten (so-called “flat band” condition, see Fig. 2.5). Under flat band conditions, surface recombination is the dominant mechanism for recombination. It has been shown that photon induced carriers can reduce band bending very effectively [40], and therefore enhance surface recombination.

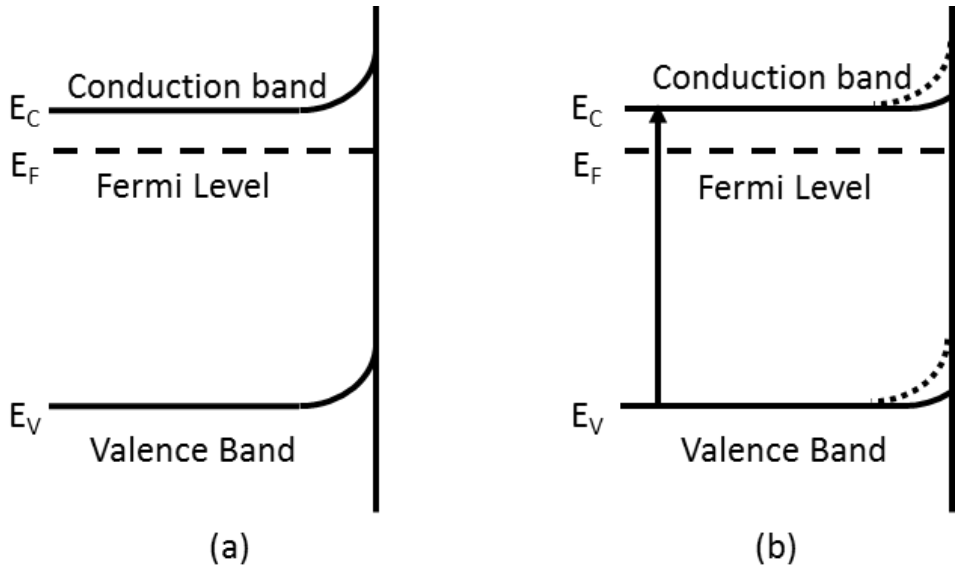

Figure 2.5: (a) Band bending in n-doped semiconductor, (b) Band flattening near surface caused by photon irradiation [41].

As discussed above, surface states influences the band structure of the solid, thereby influencing transport and recombination of carriers. Ozawa et al. studied the influence of band bending on carrier lifetimes on TiO_2 catalysts [42]. For a barrier of 0.4eV imposed due to band bending, the carrier lifetime was found to be several microseconds. Under flat band conditions, carrier lifetimes reduced dramatically to less than a nanosecond [42]. Passivation of p-Si by depositing a thin layer of Al_2O_3 has been shown to decrease surface recombination [43]. Negative charges accumulate at the Si-Al_2O_3 interface inducing band bending which poses a potential barrier for diffusion of

minority carriers to the surface, thus, increasing the carrier lifetime [43]. The influence of band bending on CO oxidation was studied on TiO_2 catalyst [44]. CO oxidation was inhibited by the O_2 adsorbed on the surface. The electron withdrawing O_2 induced an upward band bending that imposed a barrier on electrons from reaching the surface, thus inhibiting electron driven oxidation processes. Also, holes reaching the surface induced O_2 desorption, thus slowing down the oxidation reaction further. However, a partial coverage of Au over TiO_2 induced a downward band bending, which suppressed hole transport to the surface and enhanced CO oxidation [45].

2.5 Photon induced desorption

Photo-desorption is initiated through the photo-generated carriers or by inducing electronic transitions. Menzel-Gomer-Redhead (MGR) model is commonly used to explain desorption through electronic transitions [46], [47]. According to this model, a Frank Condon transition induced by highly energetic particles (e.g. photons) takes the adsorbate-adsorbent system into a repulsive potential energy state. The repulsive potential accelerates the adsorbate away from the surface. The accelerating adsorbate molecule may acquire sufficient kinetic energy to overcome the desorption barrier and hence desorb (see Fig. 2.6(a)). Antoniewicz proposed a modified version of MGR model where excitation results in the formation of an ionic state which is attracted towards the surface [48]. However, in close proximity to the surface, an electron may tunnel through the surface and neutralize the ion. The kinetic energy gained by the ionic species before neutralization may be sufficient to overcome the desorption barrier (see Fig. 2.6(b)) [48].

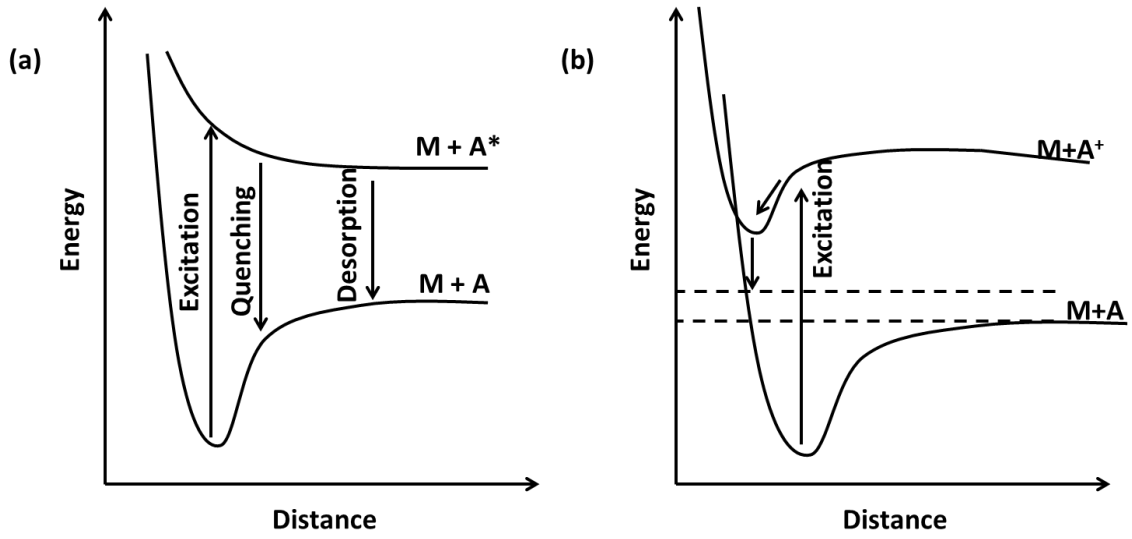

Figure 2.6: (a) MGR model, and (b) Antoniewicz model. Adapted from Reference [49]

In semiconductor materials, photo generated carriers can also induce desorption [13], [50], [51]. Carriers generated within recombination distance from the surface, reach the surface. The presence of electron withdrawing species adsorbed on the surface causes bands to bend upwards and accelerate holes towards the surface, where they can break the adsorbate-adsorbent bonds resulting in desorption. Ying and Ho studied NO desorption from Si (111). It was suggested that the hot holes generated by light radiation neutralized the NO^- species that were responsible for chemisorption, thus inducing desorption[51]. For Si etching in XeF_2, Houle proposed a photo-generated carrier induced desorption of SiF_3 as the main etch product [50]. Photon induced desorption of chlorinated silicon has been reported [52]–[55]. The main desorbing product was found to be $SiCl_2$ [52], [55]. Mechanisms involving photon generated charge carriers similar to that described above were proposed. The selective desorption of $SiCl_2$ suggested a site

specific desorption process. Hattori et al. attributed this selectivity to a larger energy requirement to desorb SiCl compared to $SiCl_x$ (x=2, 3) [55]. Calculations revealed that the bond energies for monochlorides and polychlorides was found to be ~4 eV and ~ 3eV respectively[56]. Low amounts of desorbing $SiCl_3$ was due to dissociative desorption of $SiCl_3$ which left Cl atom on the substrate [55], [56]. Chen et al. observed a linear increase in etching rate with laser fluence (wavelength = 193 nm) and reported an etching yield of 3.4×10^{-8} Si atoms per incident photon for a 33% chlorinated surface [57]. They proposed that desorption was a result of photon induced charge transfer (holes withdrawing bonding electrons or electrons added to anti-bonding levels), forming a repulsive state as described in the MGR model which ultimately led to photo-ejection of Si. Kirimura et al. observed a nonlinear dependence of desorption yield on laser fluence (wavelength = 400 nm), which was attributed to multi-photon excitation of the surface adsorbate. A multi-photon excitation was deemed necessary due to the lower photon energy compared to the bond energies of monochlorides and polychlorides [58].

For photo-generated carrier induced mechanisms to work, the charge transfer state (electronically excited state as in the case of MGR model) must be able to survive the period of bond extension leading to bond scission. From the above mechanism, it is apparent that a photon induced desorption process can be influenced by any parameter that influences the generation and transport of carriers. Desorption is also expected to be wavelength dependent due to a wavelength dependent photon absorption depth. For high energy photons, desorption rates could be independent of wavelength due to the small absorption depths.

2.6 Photo-assisted etching of silicon in the absence of a plasma

Etching of silicon induced by photons in a halogen gas environment has been studied in the past. Most of these studies used UV lasers; photo-assisted etching mechanisms in plasmas could be quite different. Synergistic mechanisms involving neutrals, photons, ions, and electrons could occur, making it an extremely complex process in a plasma environment.

2.6.1 Enhancement due to thermal effects

For high laser fluence (energy per unit area), it is very likely that the energy incident on the wafer can cause the temperature of the surface of the wafer to reach or even exceed its melting point. In such cases, etching is predominantly due to thermal effects. For example, Baller et al. recorded the mass spectra and time of flight distributions of the species desorbing off the surface while etching silicon in a chlorine environment irradiated with 308 nm and 248nm photons [54]. A Maxwell Boltzmann fit to the time of flight distributions gave the temperature of the desorbing species in the range of 1400 – 4000 K. It was postulated that the high temperatures were a result of a larger absorption cross section for SiCl compared to Si at the wavelengths studied. High temperature thermal processes are not of interest here, since the photon fluences are much too low to cause significant heating.

2.6.2 Field Assisted Diffusion

Okano et al. demonstrated the photo-assisted etching of undoped and p^+ and n^+ doped polysilicon due to UV irradiation from a He-Xe lamp [59]. Etching rates were

found to be highest in the n+ doped poly silicon, followed by undoped and p+ doped silicon. It was also observed that etching of n-doped silicon increased with increasing doping levels (see Fig. 2.7). Mass spectra revealed $SiCl_x$ (x =1,2) to be the main etch product in the etching of undoped poly-Si, whereas $SiCl_4$ was the main etch product in the etching of n-doped poly-Si [59]. They proposed a mechanism based on field assisted diffusion of the Cl^- ions on the surface into bulk Si to explain enhancement of etching by light irradiation.

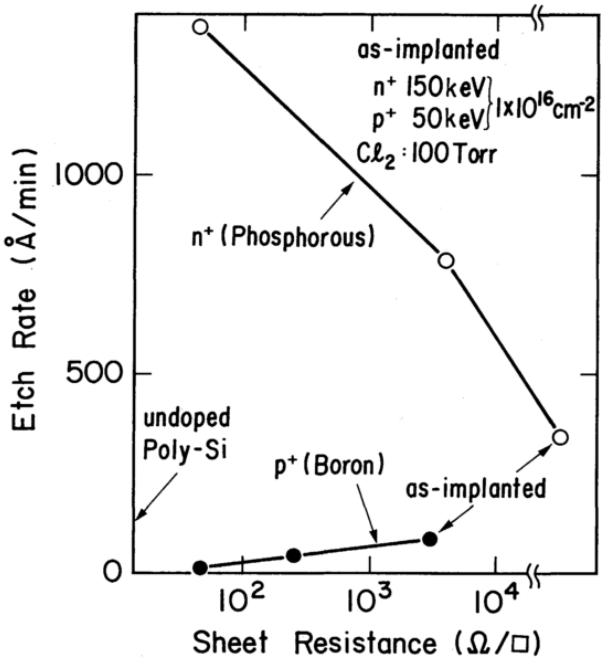

Figure 2.7: Etching rates as a function of sheet resistance for n-type and p-type Si [59].

Field assisted diffusion proposed by Mott and Cabrera was initially proposed to understand the growth of thin oxides on metal surfaces. This theory was then extended to explain the dependence of etching rates on dopant type in different halogen containing

plasmas [60]–[63]. High etching rates have been observed for etching n-type silicon compared to p-type or undoped silicon in halogen containing plasmas [62], [63]. Similar results were obtained for etching Si with Cl atoms [64]. Higher etching rates were attributed to a charge transfer mechanism [65]. The high electronegativity of chlorine led to the formation of Cl^- ions on the surface by the transfer of electrons from the silicon substrate to the physisorbed Cl atoms. The formation of negative ions leaves an equal positive charge on the silicon substrate. The negative ions subsequently diffused into the lattice under the influence of the electric field, promoting reaction and opening up new sites on the surface for adsorption [64], [65]. The need for electrons to form negative ions which then diffuse in the electric field implies that the reaction rates in undoped or p-type poly-Si would be slow.

A similar mechanism was invoked to explain the enhancement in etching on irradiation with light [59]. Electron-hole pairs are created when photons with energy larger than the band gap are absorbed. A Cl atom on the surface captures a photo-generated electron to form Cl^- which diffuses into the lattice and enhances etching reactions, as described above. The number density of photo-generated electrons is still quite low for undoped poly-Si compared to n-doped Si. Also, electrons created near the surface only participate in the surface reactions. Thus, the etching rates in undoped poly-Si were lower [59]. The differences observed in the product distribution with respect to doping were attributed to the differences in the carrier densities. In the case of n+ doped (i.e. highly doped) poly-Si, a large electron number density enables the diffusion of Cl^- into the lattice, increasing the concentration of etchant atoms on the surface resulting in highly chlorinated etch product ($SiCl_4$). Fewer photo-induced electrons are available for

the etching reaction compared to n+ doped poly-Si, and etching is limited by the rate of electron transfer from Si to Cl. The lower electron density lowers the diffusion of Cl^- into the lattice, which increases the fraction of $SiCl_x$ (x=1,2) relative to $SiCl_4$.

Winters and Haarer also developed a field assisted diffusion model to explain the enhanced etching of highly doped n-type Si(111) by a molecular beam of XeF_2 [66]. They successfully related etching to the strength of the surface electric field, which develops as a consequence of F atom adsorption on Si. Electrons from Si are transferred to adsorbed F atoms as long as the affinity level at the surface is below the Fermi level of silicon. Formation of F^- at the surface (due to the high electron affinity of F atoms) produces a surface electric field causing bands to bend upwards. (See Fig 2.8) The strength of the electric field (proportional to the number density of F^-) is controlled by the requirement that the electron affinity level must match the Fermi level at the surface and hence limited by the doping level of Si. The field strength determines the extent of band bending, and is determined as the difference between the Fermi level and the electron affinity level at the interface between Si and the fluorosilyl layer.

This model may be further modified to incorporate the effect of light irradiation on etching by considering the changes on the electronic band structure due to irradiation. The formation of F^- at the surface induces an electric field causing electronic bands to bend upwards in n-doped Si. Irradiation with light larger than the band gap energy induces photo-generated carriers. Due to the band bending, the majority carriers (electrons) are swept into the bulk, whereas the minority carriers (holes) reach the surface and neutralize the excess negative charge, thus reducing the band bending and producing

near flat band conditions (See Fig. 2.5). Under flat band conditions, the difference between the Fermi level and the electron affinity level (electric field) increases, enhancing field assisted diffusion and etching rates [66].

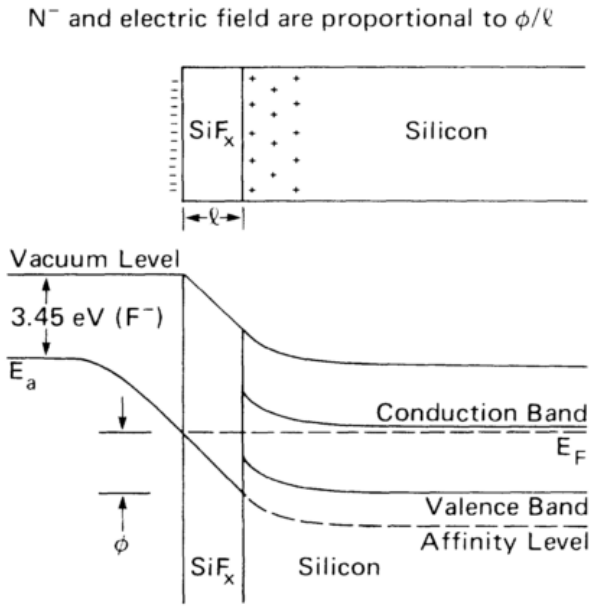

Figure 2.8: Band Bending due to the presence of F- on the surface [66].

2.6.3 Non-thermal enhancement – role of carriers

At lower laser fluence, non-thermal effects contribute to the enhancement of etching. Sesselmann et al. studied photo-assisted etching using XeCl (308nm) and KrF (248nm) lasers [13]. A wavelength dependent etching was observed with other factors such as gas pressure, gas flow rate and laser fluence affecting the etch rate. A pressure dependence on photo-assisted etching rates was observed for 308 nm radiation; etching rates were found to be higher at higher pressures due to enhanced surface chlorination caused by effective photodissociation of Cl_2 in the gas phase. With 248 nm radiation,

etching rates were found to have a stronger dependence on laser fluence and a weaker dependence on pressure compared to 308 nm radiation, suggesting that etching was mainly by a carrier-mediated process. It was also suggested that enhanced photo-desorption by direct bond breaking of Si (4.64 eV) and SiCl (4.72eV) in the chlorinated surface layer was possible at lower wavelengths (high energy photons). Bäuerle's group investigated photo-assisted etching using pulsed[67] and continuous irradiation[68] for different photon energies. It was found that etching was non thermal at low laser fluences, and increased with increasing photon energies. Etching was a result of interaction between photo generated carriers and Cl radicals produced by gas phase dissociation of Cl_2. Jackman et al. [69] studied the interaction of chlorine with Si (100) in the presence and absence of UV radiation emitted by a mercury lamp. They showed the formation of two adsorbed states: i) a strongly bound (β state) chlorinated layer with a higher activation energy for desorption (235 kJ/mol), and ii) a weakly bound (α state) chlorinated layer with an activation energy of 115 kJ/mol. Through their experiments, they found that UV irradiation induced a conversion of the β state to the weakly bound α state (presumably through a mechanism involving carriers), hence reducing the activation energy for desorption and enhancing etching.

Houle studied photo-assisted etching of silicon with XeF_2 gas and suggested a non-thermal mechanism involving photon induced charge carriers to explain enhanced etching [70]–[73]. Systematic experiments were carried out to understand the role played by photons in the fundamental processes involved in etching. XeF_2 is known to etch silicon spontaneously in the absence of both energetic ions and light. The major etch product of this spontaneous reaction is SiF_4 [74]. This was found to be true even at low

light intensities [73]. As the light intensity increased, the main desorbing product was found to be SiF_3 with a corresponding decrease in SiF_4. (See Fig. 2.9) In fact, a substantial increase in the etching rate was observed only for laser power greater than two watts. Enhanced etching due to a carrier enhanced adsorption of XeF_2 with illumination was ruled out as the signal of unreacted XeF_2 increased for low light intensities indicating that irradiation of light in fact, inhibits the chemisorption of XeF_2 on silicon. At higher powers, the inhibition effect was not ruled out. However, enhanced sticking of XeF_2 due to enhanced removal of the fluorinated layer resulted in a drop of the XeF_2 signal.

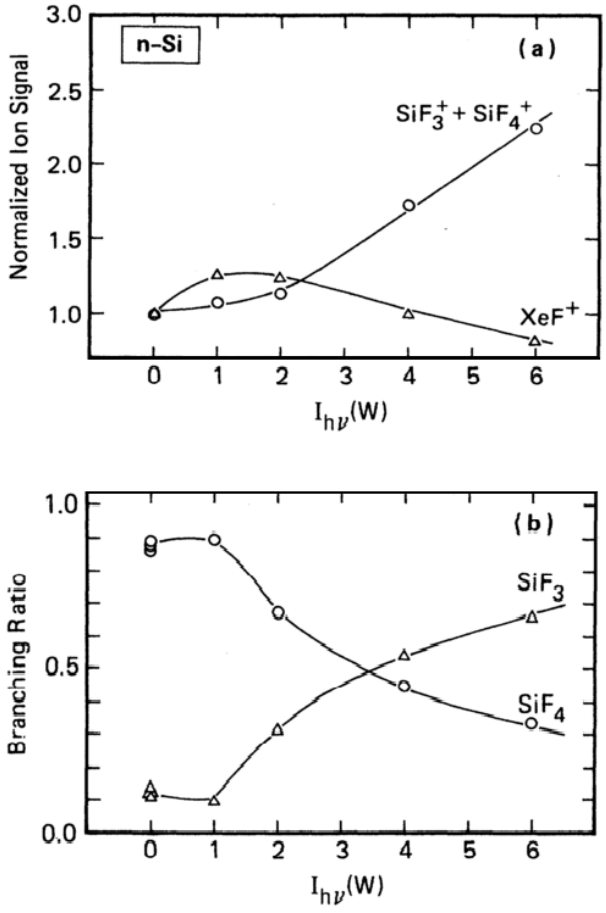

Figure 2.9: (a) Unreacted XeF_2 and etch product signals for laser etching of n-type silicon, (b) branching ratio of the major products [73].

Field assisted diffusion discussed earlier was used to explain the enhanced etching of Si in XeF_2 in the absence of irradiation [66]. Through their model, it was concluded that the strength of the doping dependent electric field could predict trends in the etching rate. However, if this mechanism were applicable, then all the etch products must show a similar dependence on the light intensity. The data showed an enhancement of SiF_3 only with light intensity (I). Evidently, field assisted diffusion cannot be a rate determining process in etching although it may be occurring in the background. With SiF_3 being the major etch product, the reaction scheme proposed earlier [71] based on the light enhanced formation of Si-F bonds had to be modified. The new proposed sequence of reactions involving photon stimulated desorption is as follows [73]:

$$F + e \rightarrow F^-, \tag{2.7}$$

$$F^- + h \rightarrow F, \tag{2.8}$$

$$-Si-SiF_3 + h \rightarrow -Si^+-SiF_3, \tag{2.9}$$

$$-Si^+-SiF_3 + e \rightarrow -Si-SiF_3, \text{ and} \tag{2.10}$$

$$-Si^+-SiF_3 + F^- \rightarrow -Si-F + SiF_3, \tag{2.11}$$

This model predicted an I^2 dependence of desorbed product which compared well with the measured dependence of $I^{1.6}$ [73]. The selective formation of SiF_3 was also explained in the mechanism. The capture of a photo-generated hole by the Si places a positive charge on the Si (equation 2.9). The F^- formed by the capture of photo-generated electrons attacks the Si to which the SiF_3 group is attached forming Si-F bond and

releasing the SiF_3 group.

Schwentner et al. studied photo induced etching of Cu and GaAs in chlorine gas [75], [76] as well as Si in XeF_2 [77]–[80] using synchrotron radiation in the vacuum UV range. Different window materials (quartz, LiF, CaF_2) were used to study the wavelength dependence on photo-assisted etching. Etching yields were found to be dependent on wavelength, with high etching yields at lower wavelengths. A high quantum efficiency of 10 atoms removed per impinging photon at 120nm wavelength was estimated for Si etching in XeF_2 (See Fig. 2.10) [77], [78] . For etching of GaAs in Cl_2, quantum efficiency (number of Ga and As atoms removed per incident photon) of ~ 100 was reported at wavelengths around 120nm. [81] The high quantum efficiency for etching implies an enhancement in one or all the basic processes involved in etching [77] i.e.,

$$q = q_{excitation} \times q_{reaction} \times q_{desorption}, \tag{2.12}$$

where $q_{excitation}$ is the probability of photon absorption that can start a reaction, $q_{reaction}$ is the probability of the reaction, and $q_{desorption}$ is the desorption probability of the reaction products.

For an assumed value for $q_{desorption} = 1$ (for volatile etch products), $q_{reaction}$ was estimated to be ~ 10^5 from the pore sizes of silicon etched by single photon events. Given the overall etching quantum efficiency of ~ 10, $q_{excitation}$ is of the order ~ 10^{-4}. This implies that although the probability of photon absorbing on the surface and triggering a surface reaction is quite small, however, when it does trigger a reaction, 10^5 silicon atoms are etched. The high etching yields at low wavelengths was attributed to direct excitation

of the fluorosilyl layer through electronic transitions. Photons have sufficient energy to excite charge transfer excitations to enable formation of F^- and SiF_x^+ which are key intermediate species that participate in the etching reaction [66], [73]. The specific electronic transitions of the species in the SiF_x layer were not identified. However, the wavelength dependence of quantum yields may provide clues to identify the possible electronic excitations.

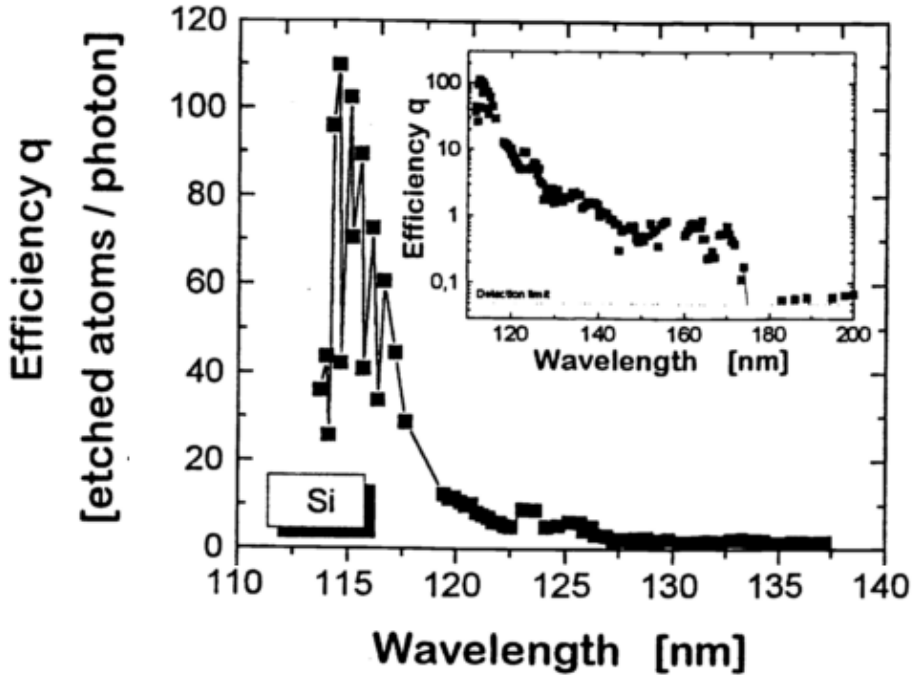

Figure 2.10: Quantum yield for etching of Si in XeF_2 as a function of wavelength [82].

2.6.4 Enhancement by Photon induced defects

VUV photons with energy greater than 7 eV have sufficient energy to break chemical bonds directly and create defects on the surface. Photon induced defects can provide new sites for adsorption that enable the formation of a halogenated layer, thus

enhancing the etching reaction. The formation of dangling bond defects caused by breaking of weak Si-Si bonds on exposure to light is well documented in amorphous Si [83]. A reduction in conductivity was observed when the substrate was exposed to light (Staebler Wronski Effect). Samukawa et al. [84] during their experiments with neutral chlorine beams found that exposure of silicon to UV photons (200 – 380nm) increased the etching rate of silicon. No enhancement in etching was observed when visible light (λ > 400 nm) was used. The enhanced etching was attributed to photon generated defects in a 10 nm surface region, which promoted the reaction between silicon and chlorine.

2.7 VUV radiation effects in plasma processing

Plasma generated VUV photons have been reported to cause damage by creating positive charges or interface traps [85] in SiO_2 thin films resulting in poor electrical characteristics [86]–[88]. Yunogami et al. found that the positive charge generation increased with the incident photon energy for energies larger than the band gap of SiO_2, and the increase in the positive charge generation was found to be proportional to the difference between photon energy and band gap [89]. The creation of a positive charge was attributed to photo-generated holes that can avoid recombination and get trapped in the SiO_2-Si interface, thereby creating a positive charge. VUV induced damage on SiO_2 [87] was found to enhance the rate of oxide stripping using HF (wet etch) after a plasma etching step. During the wet etch process, a high etching rate was observed in the first few seconds after the sample was dipped in HF, suggesting that the photon damage was restricted to the surface. Samukawa et al. used “on wafer monitoring” to measure the hole currents induced by VUV photons generated in plasmas [88]. A reduction of induced hole

currents in pulsed plasmas indicated that pulsed plasmas can be used to reduce VUV damage effects. More recently, VUV photons have been found to damage low-k porous SiCOH films [90]–[92]. VUV photons easily penetrate SiCOH films and break Si-C bonds, producing methyl groups at the surface which further react with oxygen resulting in demethylation [91]. VUV photons have also been shown to induce chemical changes in photoresist material [93]–[95]. Pargon et al. showed that the chemical modifications resulting in polymer rearrangement can smoothen linewidth roughness of the 193 nm photoresist [93].

Chapter 3 - Apparatus and Methods

The experimental apparatus and methods used in this study are described in this chapter. The experimental apparatus and methods described below were not necessarily used at the same time. Any specific changes to the experimental setup, including the use of specific diagnostic tools will be stated in the relevant chapters.

3.1 Experimental Setup

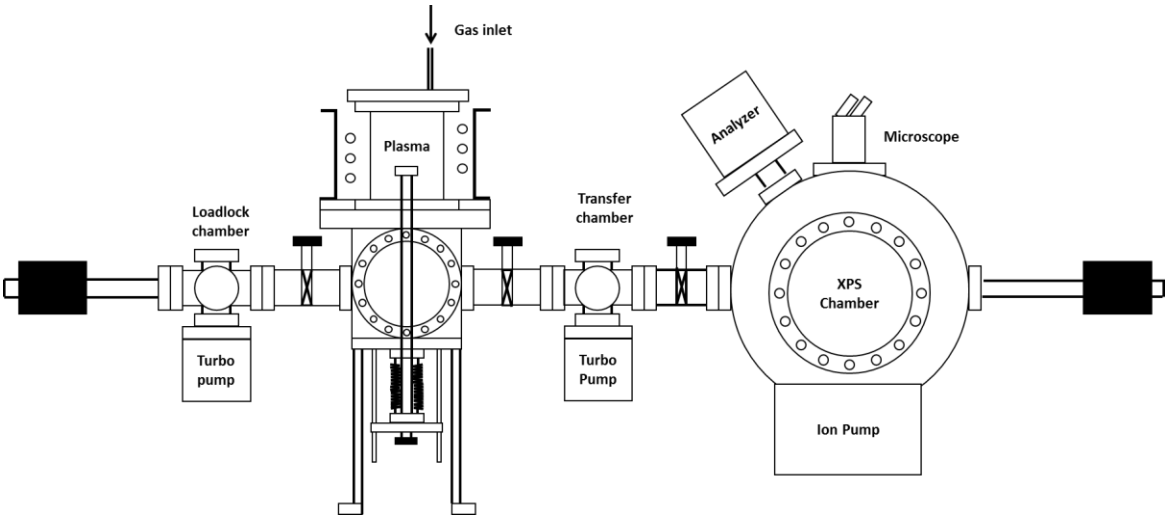

Figure 3.1: Plan of the experimental apparatus

The experimental setup (Fig. 3.1) consists of a load-lock chamber into which the substrate to be etched is introduced and subsequently transferred in vacuum, to the plasma chamber where it is etched. After etching, the sample is then transferred in vacuum, through the transfer chamber into a chamber housing the X-ray Photoelectron Spectrometer (XPS) for surface analysis if required. In addition to XPS analysis, other surface characterization techniques including Atomic Force Microscopy (AFM),

Scanning Electron Microscopy (SEM) were also used. Plasma diagnostic techniques including Optical Emission Spectroscopy (OES), and Langmuir Probe were employed to obtain both qualitative and quantitative information about plasma parameters. A detailed description of the experimental apparatus and methods used are discussed below.

3.1.1 Inductively Coupled Plasma Source

In an Inductively Coupled Plasma (ICP) source, a radio frequency sinusoidal voltage (13.56 MHz) is applied to a solenoidal coil, which typically surrounds an insulating chamber in which the plasma is ignited. RF voltage on the coil induces a RF magnetic field, which in turn induces an azimuthal RF electric field inside the chamber. Subsequently, electrons inside the chamber are accelerated and gain sufficient energy to drive ionization of the gas atoms/molecules leading to the production of a plasma. A Faraday shield may be introduced between the high voltage coil and the plasma source tube to minimize any capacitive coupling between the high voltage coil and the plasma. High plasma densities (10^{12} cm^{-3}) are achieved in an ICP etchers at very low pressures (1-10 mTorr) enabling higher etching rates and faster processing. In addition to high plasma density, the use of a separate power source to energize the ions bombarding the material being etched allows for independent control of plasma density and ion energy.

The plasma chamber is comprised of a 4 in. diameter, 7 in. long alumina tube ICP source placed on an ultra-high vacuum (UHV) stainless steel cubic chamber, supported by a water cooled adaptor flange. It was powered by a 3-turn water-cooled copper coil wound around the tube as shown (Fig. 3.2). A Faraday shield was placed between the coil and the alumina tube, to minimize capacitive coupling between the high voltage coil and

the plasma. A water cooled doughnut shaped sample stage was mounted from the bottom flange of the cubic chamber. The sample stage may be RF or DC biased for high energy ion bombardment. The doughnut shaped hole (Φ = 1 in.) on the stage allows for a rod on which the sample holder is mounted, to move the sample up to a stage that is located in the plasma discharge region. The temperature of the cooling water that flows through the rod may be adjusted to control the temperature of the sample holder. The load lock and transfer chambers are connected to the UHV cubic chamber to allow for sample transfer into and out of the plasma chamber. The back face of the cube is connected to a 4 way standard cross connection to which the turbo pump, pressure gauges and a viewport (to allow for OES) are attached. The front face of the cubic chamber is sealed by a viewport.

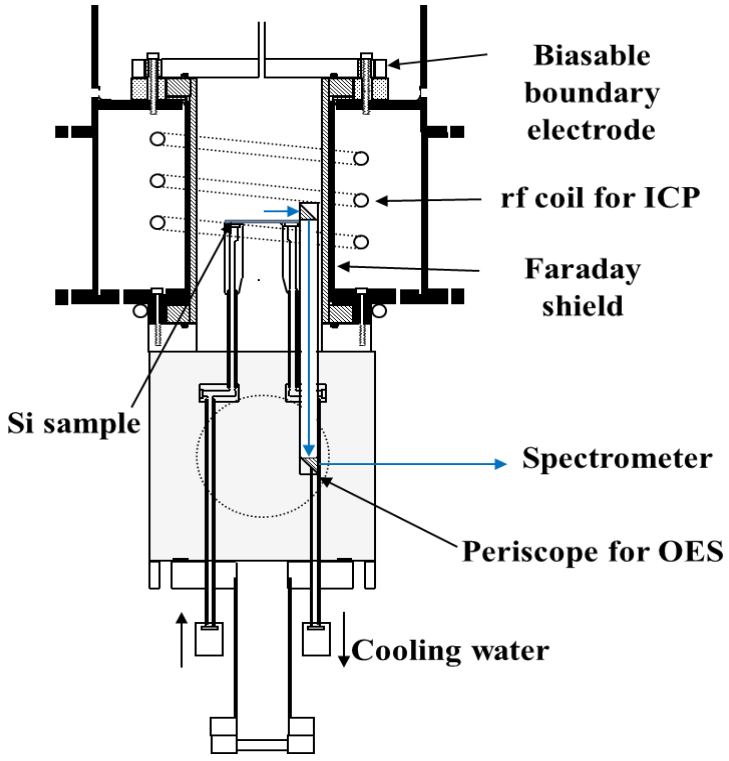

Figure 3.2: Inductively Coupled Plasma source with a biasable boundary electrode.

A controlled flow of process gas was injected into the plasma chamber through a nozzle on the top flange. This flange may be grounded or biased and is referred to as the boundary electrode. Mass flow controllers were used to control the gas flow rates. On some occasions, a needle valve was employed to introduce small quantities of gases into the plasma chamber. The process gas was pumped out of the plasma chamber using a turbo molecular pump with a pumping speed of 300 l/s (Ebara ET300W) backed by a dry pump or an oil pump. The pressure in the chamber was monitored using a capacitance manometer (MKS 629, full range 100 mTorr) located downstream of the plasma just above the pumping port. The pressures quoted in the text have been corrected to account for the pressure drop between the plasma discharge region and the point at which the pressure was being measured and hence indicate the pressure in the plasma discharge region.

3.1.2 Continuous or Pulse modulated plasma power

The plasma was powered either continuously or modulated. In the power modulated plasma (commonly referred to as pulsed plasma) the applied power was rapidly switched “ON” and ”OFF” at a predetermined pulsing frequency and duty cycle. The duty cycle is the percentage of the time for which the plasma is ‘ON’.

To generate a continuous plasma, a RF (frequency = 13.56 MHz) sinusoidal waveform generated by a function generator was fed to a RF power amplifier (ENI A500). The voltage from the amplifier was then applied on the ICP coil through an L-type matching network that was used to match the impedance of the plasma in series with the matching network (load impedance) to the 50 Ω output impedance of the RF power

supply. Under 'matched' conditions, the efficiency of power transferred to the plasma was maximized. In-line power meters placed before the matching network were used to monitor the net power (Net power = Forward – reflected power) delivered to the matching network. Plasma power may be varied by changing the amplitude of the waveform generated by the function generator.

To generate a pulsed plasma, an amplitude modulation is performed on the sinusoidal waveform before being fed to the RF power amplifier. A pulse/square waveform was generated by a separate function generator (Berkeley Nucleonics Corporation, model 645) with a peak-to-peak voltage of at least 5V, with a predetermined frequency and duty cycle. This pulse was used to modulate the 13.56 MHz sinusoidal waveform. The amplitude modulated signal was then fed into the RF power amplifier. An oscilloscope (Agilent DSO 7034B) was used to monitor the signal waveforms.

3.2 Plasma Diagnostics

3.2.1 Optical Emission Spectroscopy

Optical Emission Spectroscopy (OES) was used to record the plasma emission spectrum between 200-900 nm or to monitor the emission intensities of select atomic lines (e.g. Si, Cl, Ar etc.) or molecular bands (e.g. Cl_2) that appear in the spectrum. The Emission intensity (I) due to an electron impact excitation process is proportional to density of excited state species (n^*) and is given by [96]

$$I \propto n^* \propto n \int_{E_0}^{\infty} \sigma(E)\varepsilon(E)dE, \qquad (3.1)$$

where, n is the neutral number density, $\sigma(E)$ is the electron impact excitation cross section, and $\varepsilon(E)$ is the electron energy distribution function (EEDF).

A periscope comprising of two right angled prisms, was used to collect light from a region that spans about 1 cm above the sample stage. The light collected from this region above the sample was deflected onto an optical setup, which focused the light on a vertically oriented entrance slit of a monochromator (EU-700 series, Heath Co.). Hence, The intensities recorded are actually integrated over the 1 cm collection region in which light was collected. The entrance slit opening was set to 100 μm for which the resolution is about 2Å. The monochromator contains a 1200 grooves/mm rotatable diffraction grating. The dispersed light was detected by a GaAs photomultiplier tube (RCA C31034).

Time resolved emissions from different species were recorded during silicon etching in a pulsed plasma as a way to measure the modulation of photo-assisted etching rates of silicon. For time resolved emission measurements, current from the photo multiplier tube is measured as the voltage drop across a 3 kΩ resistor using an oscilloscope. The use of a kΩ resistor gives an RC time constant of ~ 0.3μs, which is very small for all practical purposes. Typically, the voltage measured is very small especially when the emission intensity is very low. Hence, for those cases, the entrance slit opening of the monochromator is set to 500 μm for which the resolution is 10 Å. Such poor resolution does not have any bearing on the results since the monitored lines do not overlap with any other lines.

3.2.2 Langmuir probe

A Langmuir probe is one of the most common plasma diagnostic tool that is used to measure various plasma parameters (e.g., electron density, electron temperature, EEPF etc.). It consists of a thin tungsten or platinum wire immersed in the plasma. The wire collects an electron or ion current from the plasma depending on the voltage applied on it. The current – voltage characteristic curves so obtained can then be carefully analyzed to extract plasma parameters. The Langmuir probe is an intrusive diagnostic (the probe is introduced into the plasma) and therefore, care must be taken to design the probe in a way that does not perturb the plasma too much. Due to its simplicity of design and use, Langmuir probes find widespread use in academia and industry. However, interpretation of the I-V characteristic may be challenging.

A commercial Langmuir probe (Scientific Systems Smartprobe) was used to measure the plasma parameters in this study. The Langmuir probe was attached to the bottom flange of the cubic chamber replacing the sample transfer rod. The Langmuir probe can be moved vertically along the axis of the plasma chamber. Most of the measurements were obtained in the bulk plasma at a location ~1 cm above the sample stage. The probe tip was made of a 0.18 mm diameter tungsten wire with a length of 6.5 mm, but only 1.5mm was actually exposed to the plasma. The remaining 5 mm of the wire was covered using a ceramic tube (0.5 mm outside diameter). The probe holder is located far away from the location at which measurements are taken and thus minimize any perturbation of the plasma by the probe holder. A reference probe that floats at the plasma potential is used to track and compensate for any drift in the plasma potential due

to a poor current return path to ground. RF plasmas also typically require the use of RF filters/chokes in the probe circuit to filter the oscillations of the plasma potential. The filtering is achieved by using a pair of chokes (inductors) connected very close to the probe tip that resonate at the RF driving frequency. The inductors increase the probe to ground impedance with respect to the plasma to probe sheath impedance, ensuring that RF component of the voltage appears across the probe to ground impedance. Fast acquisition electronics enabled averaging of 100's of IV curves to minimize noise. Time resolved measurements of a pulsed plasma were made possible by using an external trigger signal to synchronize data acquisition with the pulsed power supply.

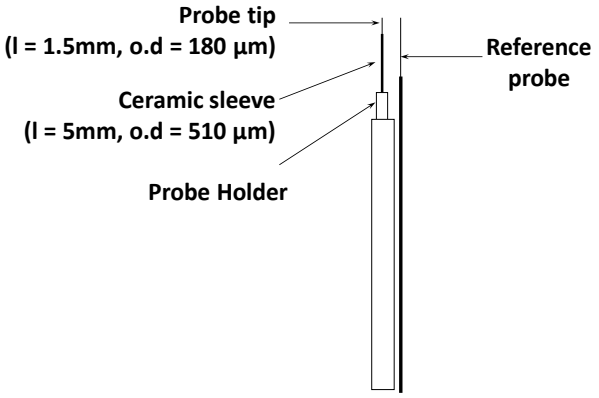

Figure 3.3: Langmuir Probe

The IV curves were then analyzed to extract plasma parameters. The Electron Energy Probability Function ($f_p(\varepsilon)$) was obtained from the second derivative of the probe electron current I_e [97]

$$f_p(\varepsilon) = \frac{2m_e}{e^2 A}\sqrt{\frac{2}{m_e}}\, d^2 I_e / d\varepsilon^2. \tag{3.2}$$

In eq. (3.2), m_e is the electron mass, A is the probe exposed area, ε is the electron energy (ε is related to probe voltage (V_{probe}) and plasma potential (V_{plasma}) as $\varepsilon = V_{plasma} - V_{probe}$), and e is the elementary charge. The electron density (n_e), and the average electron energy $<\varepsilon>$ were calculated by integrating the electron energy probability function as

$$n_e = \int_0^\infty \varepsilon^{0.5} f_p(\varepsilon) d\varepsilon \text{ and} \tag{3.3}$$

$$< \varepsilon > = \frac{1}{n_e} \int_0^\infty \varepsilon^{1.5} f_p(\varepsilon) d\varepsilon. \tag{3.4}$$

The effective electron temperature (T_e) was computed as $2/3 < \varepsilon >$. The ion density (n_i^+) was obtained using Laframboise's orbital motion-limited (OML) theory for a collisionless sheath [98]

$$n_i^+ = \xi \left(\frac{r_p}{\lambda_d}, \frac{V - V_p}{kT_e} \right) \frac{I_i^+}{eA} \sqrt{\frac{2\pi M_i}{kT_e}}, \tag{3.5}$$

where ξ is a correction factor that depends on a dimensionless potential and the ratio of cylindrical probe radius (r_p) to plasma Debye length (λ_d), I_i^+ is the ion saturation current, and M_i is the ion mass.

3.3 Surface Characterization

3.3.1 X-Ray Photoelectron Spectroscopy

X-ray Photoelectron Spectroscopy (XPS) is a surface sensitive analytical technique that is used to obtain quantitative measurements of elemental compositions in the top 3-5 nm from the surface of the sample being analyzed. An X-ray Photoelectron

Spectrometer manufactured by Surface Science Instruments using an Al x-ray source was used for the analysis. Monochromatic x-ray beam (λ = 0.83 nm which corresponds to a photon energy of 1486.6 eV) is produced by diffracting and focusing the x-rays on to the sample using a quartz crystal. The sample may be manipulated in the x-, y-, and z-directions to perform surface analysis over different regions of the sample. The sample may also be tilted with respect to the incident beam to allow for angle resolved XPS that reveals the depth profile of chemical species. In this study, spectra were obtained for x-ray take-off angle of 30° which corresponds to an analysis depth of about 1 nm for silicon. The photo electrons ejected from the sample is detected by a hemispherical analyzer. The system is also equipped with an electron flood gun that is used to neutralize the charge developed on an insulating sample during analysis.

Low resolution survey spectra were obtained for binding energy spanning 0 – 1000 eV using an x-ray beam with a diameter of 800 μm. Elements are identified from the position of the peaks (binding energy) and their compositions are calculated from the area of the peaks along with the appropriate sensitivity factors. In this study, XPS was used to analyze the cleaned silicon coupons before etching to ensure cleanliness of the sample. The samples were analyzed after etching in a halogen containing plasma to determine the surface halogen coverage. High resolution spectra of silicon were also obtained to reveal the silicon halide products formed on the surface.

3.3.3 Atomic Force Microscopy

An Atomic Force Microscope (Veeco CP-II) operating at atmospheric pressure was used to examine the surface morphology of the coupons etched in different halogen

containing plasmas with and without applied bias. Images were obtained in contact mode using high resolution silicon nitride probes (MSCT AUNM, k = 0.1 - 6 N/m, tip radius = 10 nm). Some images were also obtained in non-contact mode using silicon probes (RTESPA, k = 20-80 N/m). To ensure good images, images of a calibration grating sample were obtained and calibration of the piezo scanner was performed at regular intervals. Probes were also changed frequently to ensure tip sharpness and eliminate tip related image artefacts.

Multiple 5 μm x 5 μm images with a resolution of 256 pixels per line were obtained by scanning over different areas of the etched coupon. The images acquired required by flattening to compensate for sample tilt and bowing of the piezo tube. Image flattening was performed by subtracting a second order polynomial curve fit from the acquired line profile for the entire image. In some cases, the etched features were masked before the flattening was performed to minimize furrow type artefacts. The AFM images were then used to calculate the root mean square roughness (*R*) by

$$R = \sqrt{\sum_{n=1}^{N} \frac{(z_n - \bar{z})^2}{N-1}}, \tag{3.6}$$

where *N* is the number of data points in the selected region, z_n is the height of data point 'n', and $\bar{z}$ is the mean height of all data points in the selected region.

Chapter 4 – Photo-Assisted Etching in Chlorine and Bromine Containing Plasmas

In plasma photo-assisted etching (PAE) might disrupt the self-limiting nature of precise etching techniques such as atomic layer etching. Its relative importance as an etching mechanism at low ion energies could be problematic to achieving highly selective and low damage etching. This study was undertaken to: (a) explore the importance of PAE in some of the most commonly used halogen based plasmas, (b) study the characteristics and mechanism of PAE, and (c) develop insights into the role played by VUV photons in enhancing etching.

4.1 Experimental Setup

The experimental setup has been described in detail in the previous chapter (see Figs. 3.1 and 3.2). A controlled flow of a halogen gas (Cl_2, Br_2, HBr, Br_2/ Cl_2, HBr/ Cl_2) diluted in Ar with a dilution ratio of 0.5, was injected into the plasma chamber through a nozzle on the top flange (also referred to as the boundary electrode). The process gas was pumped out of the plasma chamber using a turbo molecular pump. The plasma was operated continuously at 400W RF power (13.56 MHz) at a pressure of 60 mTorr. Negative DC bias pulses (rectangular pulse at 10 kHz with a 50% duty cycle) were applied on the sample to accelerate ions impinging on the substrate. The ion bombardment energy (sum of the plasma potential and the applied DC bias) was varied by changing the value of DC bias on the sample. At 60mTorr, the ion bombardment energy in the absence of substrate bias would correspond to the plasma potential which is

expected to be quite low (< 7 V). Ions at such low energies are incapable of causing any etching as the ion assisted etching threshold of Si has been reported to be ≥ 16 eV.

A sample coupon (~1.5 cm^2) cut from a p-type Si (100) wafer (doping level ~ 10^{15} cm^{-3}) was UV ozone treated to remove impurities and then dipped in HF to remove the oxide layer. Despite the best efforts to reduce contamination, XPS analysis of the cleaned samples revealed < 3% of C and < 1% O (presumably oxide layer was not etched away completely after HF treatment) on the surface. The sample was quickly mounted on a 1 in. diameter sample holder and transferred into the plasma reactor through the load-lock chamber. After etching, the processed sample was transferred in vacuum to the X-ray photoelectron spectrometer (XPS) for surface composition analysis. In selected cases, the sample was then removed from XPS chamber and transferred to an atmospheric pressure AFM (Veeco CPII) to examine the surface morphology of the etched silicon samples.

Optical Emission Spectroscopy (OES) was used to obtain the relative etching rates of silicon as a function of ion bombardment energy by monitoring the emission intensity of Si (288.1 nm). Emission intensity depends on electron density, excitation cross section and the electron energy distribution. For a constant plasma power and pressure, electron density and energy distribution is not expected to change. Therefore, as long as the plasma operates under a fixed set of conditions with bias being the only variable parameter, any change in the Si emission intensity with bias is a result of a change in the etching rate of silicon. Absolute etching rates were measured using a masked silicon coupon. The mask consisted of a small piece of silicon covering the

silicon sample. Etching around the mask results in the formation of a step, the height of which was measured using a stylus profilometer.

4.2 Results

4.2.1 Si etching in different halogen containing plasmas

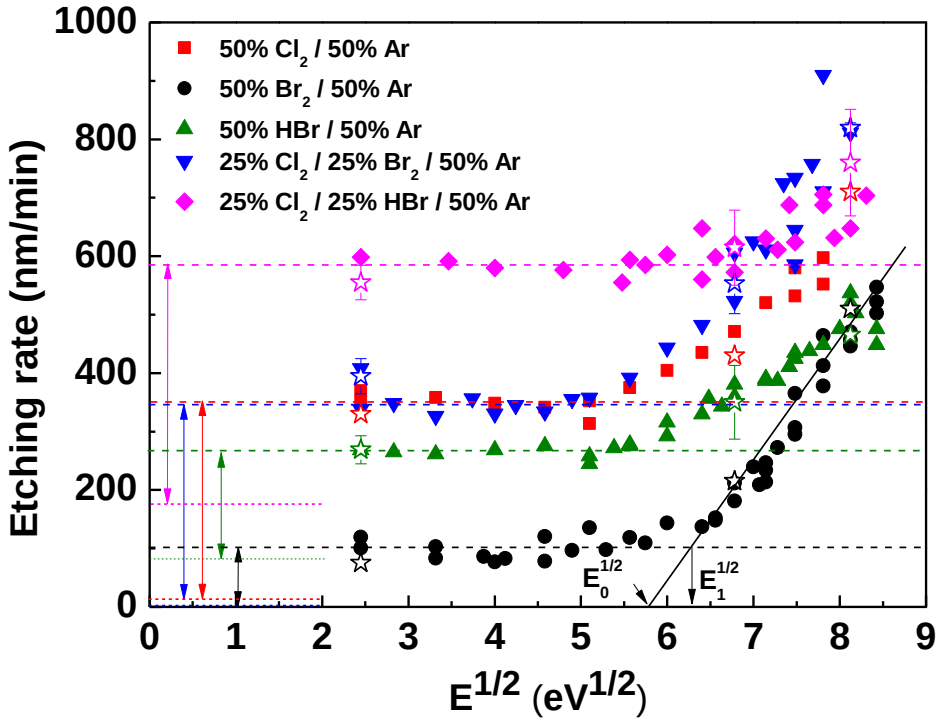

Figure 4.1: Etching rates as a function of the square root of ion energy. The double headed arrows represent net photo-assisted etching rate after subtracting isotropic chemical etching.

Relative etching rates of silicon in different plasmas were measured by varying the ion bombardment energy (Fig. 4.1). For ion energies beyond a particular threshold value, the etching rates increases linearly (etching rate $\propto E^{0.5}$). The apparent ion-assisted

etching threshold, defined as the point of intersection of two straight lines fit to the two linear portions of the curve, is shown as E_1 in Fig. 4.1. A more common way to determine the ion-assisted etching threshold (indicated by E_0) is to extrapolate to zero the straight line of the ion-assisted etching regime (where etching rate $\propto E^{0.5}$). The different thresholds for the different gas chemistries reflect the relative reactivity of the different halogen gases. The increase in etching rates for ion energies greater than the threshold is due to energetic ion bombardment that assists in etching by breaking bonds and promoting the desorption of etch product. For ion energies below the ion-assisted etching threshold, silicon etched at a constant rate independent of ion energy. This constant etching was mainly due to photo-assisted etching (PAE) by light generated in the plasma, after ruling out other possible mechanisms involving low energy ions/metastable species, and isotropic chemical etching by Cl atoms [9]. However, substantial mask undercutting was seen for silicon etching in HBr containing plasmas. It is apparent from Figure 4.2(a) and Figure 4.2(c) that there is a substantial undercutting of the mask (dashed white lines). Etching in the horizontal direction (indicated by the horizontal arrow) is small, but not negligible compared to etching in the vertical direction (indicated by the vertical arrow). Figures 4.2(b) and 4.2(d) show that etching under the mask is negligible in the case of 50%Cl_2/50%Ar and 50%Br_2/50%Ar plasmas. This is expected as halogen atoms (Cl, Br) do not chemically etch p-type silicon at room temperature [64]. In HBr containing plasmas, anisotropic etching profiles have been reported and isotropic profiles are not common [99]–[102]. The anisotropic profiles may be a result of the erosion of the photoresist mask or chamber materials that help in forming a protective layer on the sidewalls, thus preventing isotropic etching. In HBr containing plasmas, it is possible

that H atoms could etch Si isotropically, as it is known to occur [103]–[108]. The lack of horizontal etching in the latter cases suggests that horizontal etching (mask undercut) is probably due to H-atoms originating from HBr.

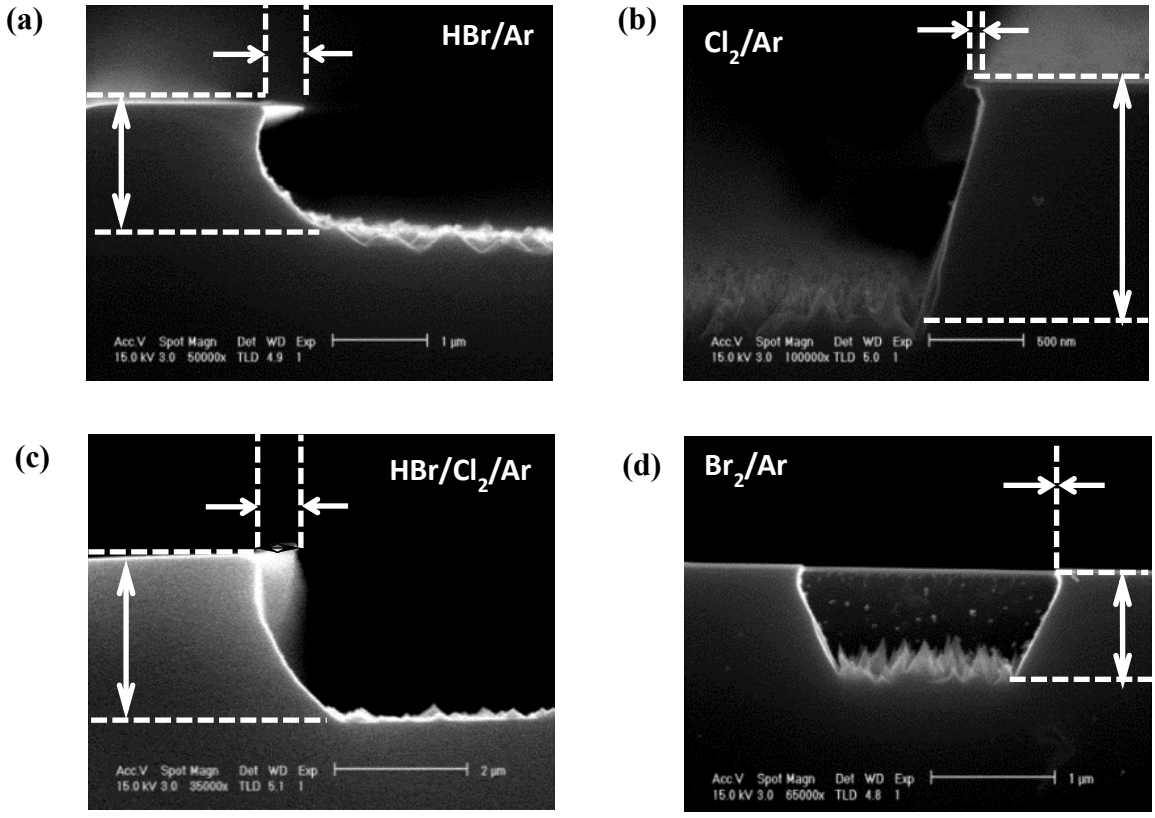

Figure 4.2: Cross section SEM of masked p-silicon etched in different halogen plasmas at 0V bias. Horizontal arrows indicate the chemical etching and the vertical arrows indicate photo-assisted etching in addition to chemical etching.

The 'true' photo-assisted etching rates (colored arrows in Figure. 4.1 and Table 4.1) were obtained by subtracting the isotropic chemical etching component from the total sub-threshold etching. PAE rates were found to be lowest in 50%Br_2/50%Ar plasma. On the other hand, the highest PAE rates were observed in 25%HBr/25%Cl_2/50%Ar

plasma. The measured PAE rates matched quite well with the product of the observed Ar emission intensity (750.4nm) and the total halogen surface coverage. Here, the Ar emission at 750.4 nm was used as an indicator of the VUV photon flux irradiating the sample. VUV photon flux striking the surface can be measured from the plasma VUV emission spectrum. Strong VUV emission lines in a halogen/argon plasma are typically observed at 104.8 nm and 106.6 nm (Ar), 134.7 nm and 137.9 nm (Cl), and 148.8 nm and 157.5 nm (Br). Although VUV emission spectra was not recorded, the intensity of Ar VUV emission (photon energy ~12eV) mentioned above should be proportional to the intensity of emission from the high energy Ar $2p^1$ state (~ 13.5 eV) at 750.4 nm. The halogen coverage on the etched samples was obtained by X-ray photoelectron spectra taken at a 30º takeoff angle (Table 4.1). The product of the observed Ar emission intensity (750.4nm) and the total halogen surface coverage matched well with the experimentally measured photo-assisted etching rates (Fig. 4.3).

Table 4.1: Photo-assisted etching rate, Ar (750.4 nm) emission intensities, and surface halogen coverages measured using XPS.

Plasma	**I_{Ar} 750.4 nm (a.u)**	**Halogen Coverage**			**PAE Rate (nm/min)**
		Cl	**Br**	**Cl + Br**	
Cl_2/Ar	0.221	0.181	0	0.181	330
Br_2/Ar	0.138	0	0.091	0.091	99
HBr/Ar	0.205	0	0.103	0.103	185
Cl_2Br_2/Ar	0.262	0.107	0.025	0.132	333
Cl_2/HBr/Ar	0.272	0.109	0.027	0.136	395

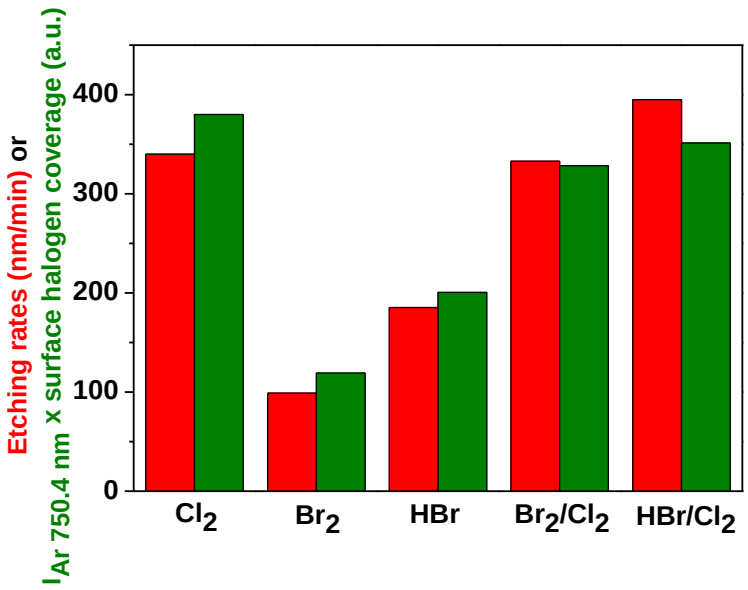

Figure 4.3: Etching rates at 0V bias in different plasmas indicated by the red columns. The green column is the product of surface halogen coverage and Ar (750.4nm) emission intensity.

4.3 Wavelength dependence of Photo-assisted etching

The dependence of photo-assisted etching on wavelength was investigated by measuring the etching rate of silicon placed under windows with different light transmission characteristics. For example, a lithium fluoride (LiF) window transmits ~10% at 105 nm; magnesium fluoride (MgF_2) transmits 50% at 125 nm and transmission rapidly falls to 0% at 110 nm; UV grade fused silica windows do not transmit wavelengths < 170 nm. All these window materials are opaque to Ar VUV emission at 104.8nm and 106.6nm which are likely major contributors to the total VUV radiation and etching rate of silicon. Hence, a 50% Cl_2-50% Kr gas mixture was used in this study instead of 50% Cl_2-50% Ar, as Kr VUV lines at 116.5 nm and 123.6 nm are transmitted partially by MgF_2. Since Kr has a lower ionization potential (14 eV) compared to Ar

(15.8 eV), the electron temperature and plasma potential in a 50% Cl_2/50% Kr plasma will be lower. At 60 mTorr, the plasma potential (and ion energy) would be expected to be lower than that for 50% Cl_2/Ar plasmas. Hence, there should be no etching caused by sub-threshold ion bombardment.

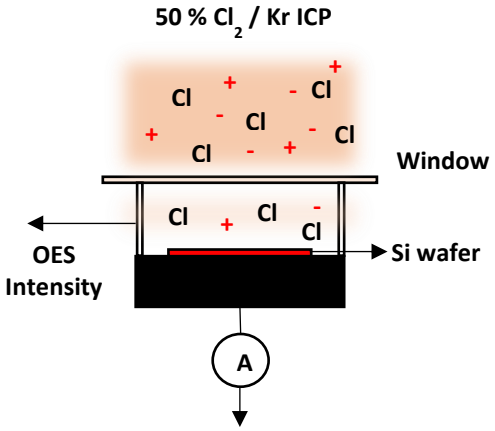

Figure 4.4: Silicon etching under a transmitting window material. The ion current to the grounded stage was measured using an ammeter and the emission signals were recorded from the region between the window and Si wafer.

Photo-assisted etching rates of a masked silicon sample placed under different windows (Fused silica, MgF_2, opaque. see Fig. 4.4) were obtained by measuring the etch depth using a stylus profilometer after etching. These were compared to etching without any window (transmits all wavelengths). The presence of the window above the Si substrate lowers the plasma density in the region between the Si substrate and the window. To estimate the reduction in plasma density, current to the grounded sample stage were measured by applying a positive bias (+60 V) on the top boundary electrode. A positive bias on the boundary electrode increases the plasma potential, preventing electrons from reaching the grounded stage. Thus, the current measured on the grounded stage consists only of the ion current. This ion current is proportional to the density of

ions in the region between the Si substrate and the window material. Emissions from Cl (792.4 nm) and Kr (768.5 nm) were also recorded from the region just above the sample parallel to the window.

The ion current density (current per unit area), Cl and Kr emissions under different window materials are shown in Table 4.2. Ion current density (proportional to ion density) dropped by a factor of ~ 7 when a window was placed above the sample. Absolute emission intensities of Cl and Kr were also found to be a factor of 7-9 lower compared to that in the absence of a window. This result is consistent with the lowering of ion density also by a similar factor, suggesting that the plasma density in the region between the sample and the window was lowered by about 7 times by introducing the window. However, the I_{Cl}/I_{Kr} ratio (proportional to the Cl density) remained constant, implying that the Cl number density is not affected by the presence of the window.

Table 4.2: Etching rate, absolute atomic emission intensities of Cl (792.4nm) and Kr (768.5nm), Cl/Kr ratio, and ion current density measured under different windows when p-Si is etched at 0V bias.

Window material	**Etching rate (nm/min)**	**Cl 792.4nm (a.u)**	**Kr 768.5nm (a.u)**	**Cl/Kr**	**Ion current density (mA/cm^2)**
No window	**235 ± 20**	**1.3**	**2.79**	**0.465**	**13.1**
MgF_2	**19.4 ± 2.3**	**0.143**	**0.308**	**0.464**	**2.4**
Quartz	**13.5 ± 0.8**	**0.181**	**0.498**	**0.363**	**2**
Opaque	**11.4 ± 0.9**	**0.134**	**0.388**	**0.345**	**1.8**

Based on the transmission characteristics of the windows used, etching rates (ER) were ordered as follows: $ER_{windowless} >> ER_{MgF2} > ER_{quartz} \sim ER_{opaque}$. The etch rate is not zero beneath the opaque window because light scatters off the bottom of the window, and also because low intensity plasma is generated between the sample and the window. It may also be noted that the etching rate under the opaque window was about 20 times lower compared to etching without any window, while the reduction in ion density was ~7 times. Also, the Cl neutral density remained unaffected by the presence of the window. These observations confirm that the sub-threshold etching is not due to low energy ions or Cl neutrals.

The etching rate under a quartz window was essentially the same as that under an opaque window, suggesting that photons with wavelength > 170nm are not effective in inducing etching. The etching rate under the MgF_2 window was ~12 times lower than the etching rate without any window. This reduction in etching is much lower compared to the reduction in VUV transmission by MgF_2. Krypton VUV lines that are partially transmitted (~ 50% around 125 nm) and possibly Cl VUV lines (134.7nm and 137.9nm) that are transmitted at a much higher level through the MgF_2 window. It must be noted that a yellow tint was formed on the MgF_2 window after operating in the plasma. This may be due to the formation of color centers in MgF_2 when exposed to a plasma. The formation of color centers may also affect the transmission of light. If there was indeed a reduction in transmission of VUV light, it is possible that photo-assisted etching was suppressed. Based on the reduction in etching, it seems that Kr VUV lines (poorly transmitted through MgF_2) at lower wavelengths are more effective in inducing etching compared to Cl VUV lines. More experiments need to be done to clarify the relative

contribution of the various VUV lines to photo-assisted etching. Nevertheless, the results indicate the role of VUV radiation (specifically lower wavelength) in etching.

Etching rates of silicon under different windows were obtained as a function of ion energy (Fig. 4.5). Etching rates at an ion energy of 80 eV under the different windows after subtracting the photo-assisted etching component were calculated (Table 4.3). It may be noted that etching rates at high ion energies are nearly independent of the window material, after subtracting the photo-assisted etching component. The reduction in ion-assisted etching rates by a factor of eight under the window is consistent with the drop in ion density (measured by ion current to the stage) by a similar factor.

Table 4.3: Photo-assisted Etching (PAE) rate and Ion assisted etching (IAE) rate at 80 eV after subtracting the PAE component under different window materials.

Window	**PAE rate (nm/min)**	**IAE at 80 eV (nm/min)**
No window	**235 ± 20**	**255**
MgF_2	**19.4 ± 2.3**	**31**
Fused Silica	**13.5 ± 0.8**	**37**
Opaque	**11.4 ± 0.9**	**33**

Etching under different windows due to ion bombardment alone is expected to be the same. Adding the photo-assisted etching contribution, it is expected that overall etching at 80 eV should be higher underneath MgF_2 window in comparison to quartz and opaque windows. However, the ion assisted etching rate under the MgF_2 window was nearly the same as that under an opaque or fused Silica window in spite of the photo-assisted etching rate under MgF_2 being higher. The reduction in ion assisted etching rate under the MgF_2 window at high ion energy implies a suppression of etching or a negative

synergy effect due to photons transmitted by MgF_2. Also, it is clear from Fig. 4.5 that the apparent ion-assisted etching threshold depends on the material of the window. Quartz and opaque windows show similar threshold (16 eV), whereas magnesium fluoride and no window have a similar threshold (36 eV).

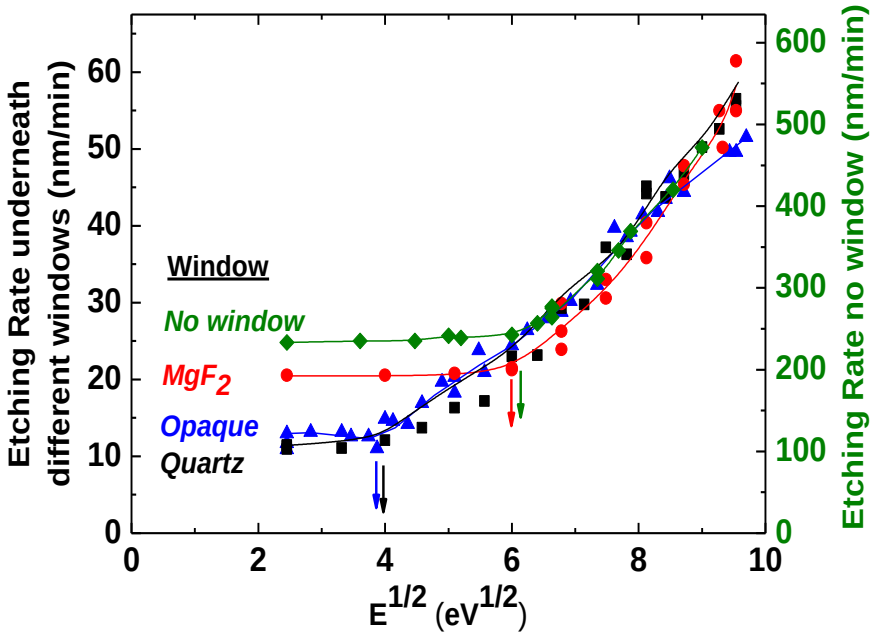

Figure 4.5: Etching rate under different window materials as a function of the square root of ion energy.

A plausible explanation for the negative synergy effect and the shift in apparent thresholds is as follows: Just above the ion-assisted etching threshold ($\mathbf{E_{th}}$), ion bombardment disrupts the silicon lattice by breaking Si-Si bonds. The damaged lattice results in an increase in the rate of recombination of electron-hole pairs, which reduces the density of photogenerated carriers and suppresses photo-assisted etching (Figure 4.6). A similar mechanism was found to be responsible for the suppression of photoluminescence of GaAs that was processed by ion bombardment [109], [110]. As ion

energy increases beyond the threshold for ion-assisted etching, PAE is suppressed even further. The net effect of suppressing photo-assisted etching with increasing ion bombardment causes an apparent shift in the threshold energy ($\mathbf{E_{th,apparent}}$). At ion energies beyond this apparent threshold, PAE is not important and ion-assisted etching is the dominant mechanism. The suppression of PAE due to ion bombardment also explains the near equivalence of etching rate at high energies under different windows, where etching is mainly due to ion bombardment and not due to photons.

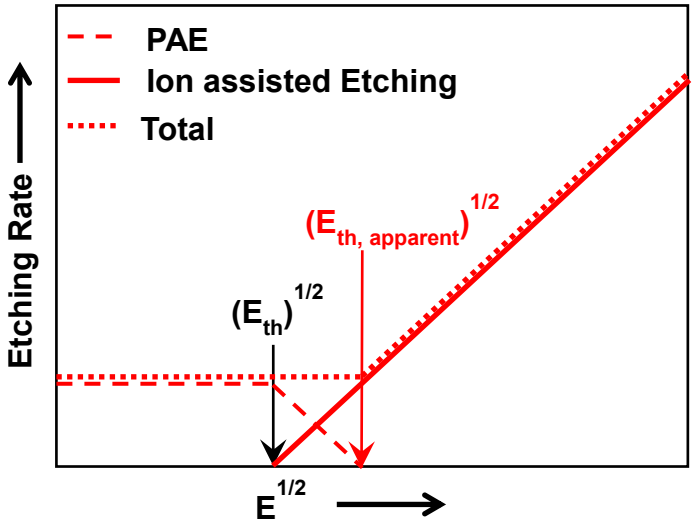

Figure 4.6: Suppression of PAE due to ion bombardment for $E_{ion} > E_{th}$

4.4 Surface morphology and roughness

It is evident from the SEM cross section images (Figure 4.2) that the bottom of the etched trenches is quite rough. The rough morphology is probably caused by the masking action of contaminants on the surface (e.g. residual native oxide and carbonaceous deposits), that remain on the surface even after cleaning. XPS analysis of

clean, pre-etched samples revealed 3-5% oxygen and 3-5% carbon on the surface. In addition to residual contaminants, it is also possible for materials inside the plasma chamber to erode and deposit on the sample (e.g. erosion of quartz window). These deposited materials can also act as micro masks on the sample surface. For the experimental conditions used in this study (high pressure, 0V substrate bias), the energy of ions bombarding the substrate is expected to quite low (approximately equal to the plasma potential). At such low energies, it is impossible to sputter away contaminants, which act as micro-masks, preventing etching of silicon underneath and imparting roughness to the surface.

Atomic force microscopy (AFM) was used to examine surfaces etched in different plasmas. Samples were etched - with and without applied bias - for different times to understand the evolution of surface roughness. 5 μm x 5 μm images of the etched surface were obtained mostly in contact mode AFM; some images were also obtained by non-contact imaging mode. The only image processing technique applied was background correction to compensate for the bowing of the piezo tube. The roughness of the etched silicon wafers was then calculated using equation described in previous chapter.

Silicon wafers etched in 50%Cl_2/50%Ar plasma without applied bias were found to be relatively smooth, except for a few pyramid-shaped hillocks (Figure 4.7) that were interspersed on the surface. Starting with a pre-etch roughness of 0.44 nm, the roughness (excluding the pyramidal features) increased to 0.65 nm, 0.85 nm, or 1.5 nm after 30 s, 60 s, or 120 s of etching, respectively. Etching with a DC bias of -40V applied to the sample

stage resulted in rougher surfaces, the roughness being 1.35 nm, 1.05 nm, or 6.18 nm after 30 s, 60 s, or 120 s of etching, respectively.

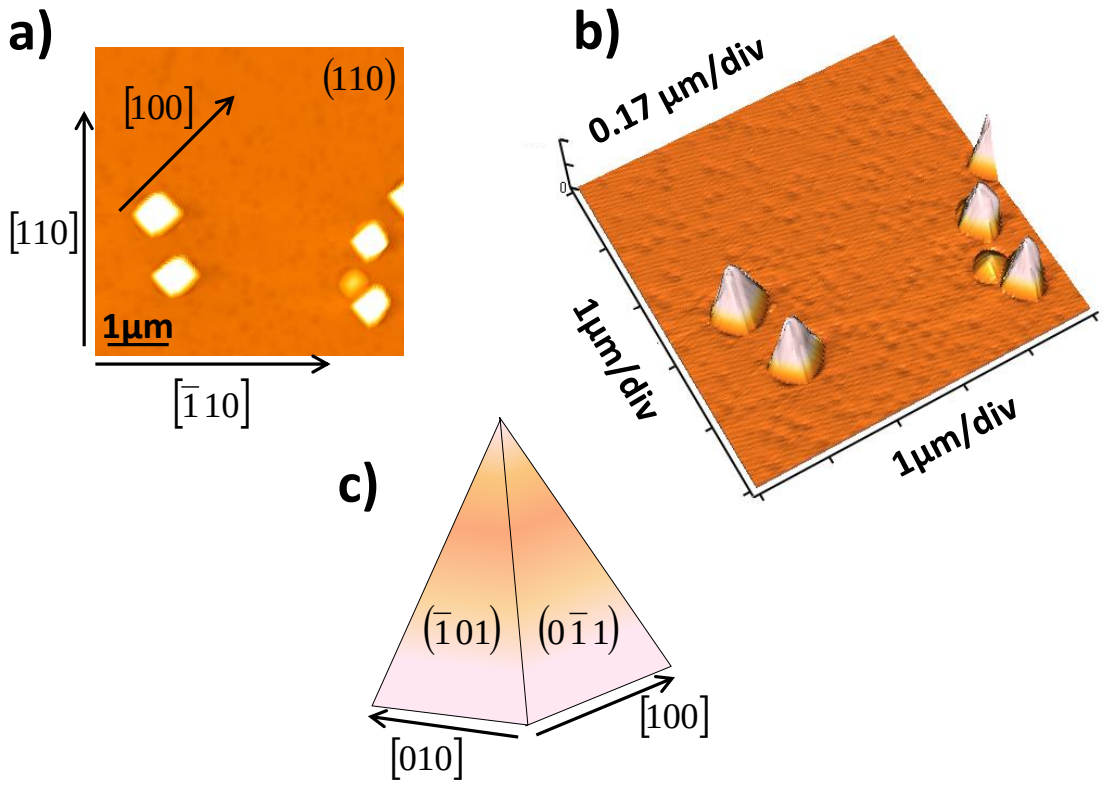

Figure 4.7: (a) 25 µm^2 AFM image of p-Si etched in 50% Cl_2/50%Ar plasma at 0V bias for 2 minutes. (b) 3-D view showing the pyramidal features. (c) {110} planes that form the faces of the pyramidal feature.

The formation of well-defined pyramidal structures during etching suggests that PAE depends on the orientation of crystallographic planes. Analysis of the AFM images showed that the base of the pyramidal features are oriented at 45° to the {110} cleavage planes and hence lie on the <100> direction. Line profiles obtained along the lateral edge and along the facets of the pyramid perpendicular to the base were used to measure

angles with respect to the wafer surface. These angles were found to be 39.2° + 3.7° and 47.4° + 4.8° respectively, which are close to 35° and 45°angles, if the pyramidal features formed by {110} planes (see Figure 3.8). Thus, PAE is strongly dependent on the orientation of crystallographic plane, with {100} planes etching faster compared to the {110} planes giving rise to the formation of well-defined pyramidal features. Similar crystallographic etching of silicon by chlorine atoms has already been reported[59], [111]. The (100) plane of lightly doped p-type Si etched about 30 times faster than the (111). This was attributed to steric hindrance on a closely packed Si(111) surface which reduces the number of favorable adsorption sites and penetration of relatively large Cl atoms into the Si lattice[27].

The RMS roughness (R) for substrates etched in different plasmas followed the order: R(50%Br_2/50%Ar) > R(50%HBr/50%Ar) > R(25%HBr/25%Cl_2/50% Ar) > R(50%Cl_2/50%Ar). The line profiles of the etched surfaces are shown in Figure 4.8. Silicon etched in 50%Br_2-50%Ar exhibited the worst roughness; ~20 nm after 30 s of etching, remaining nearly the same after 60 s and 120 s of etching. Etching with a DC bias of -40V on the sample, resulted in roughness that was about the same or just slightly higher, compared to the roughness of samples that were etched without bias. At a low ion energy of 40 eV, PAE could still be a major contribution to the total etching.

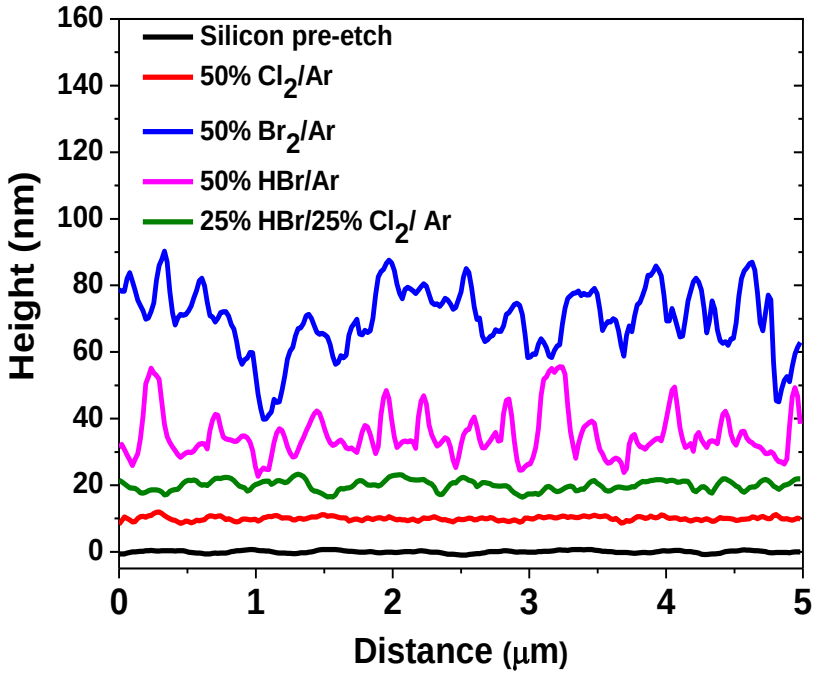

Figure 4.8: Line profiles of p-Si etched in different halogen containing plasmas. The profiles have been shifted for clarity.

4.5 Photo-assisted etching yields

Low etching yields (atoms of silicon etched per incident photon) have been reported for photon (laser) enhanced etching in a halogen environment. Sesselmann et al. [13] reported an etching yield of 3.3 x 10^{-4} Si atoms/photon at 248 nm and 6.46 x 10^{-6} Si atoms/photon at 308 nm using pulsed excimer lasers. Yields of 2.8 x 10^{-6} Si atoms per photon and 2.1 x 10^{-6} Si atoms per photon were reported at 488 nm and 514 nm using Ar+ excimer laser in chlorine atmosphere at 750 torr [68]. Woodworth et al. measured an absolute photon flux of 3.5 x 10^{16} $cm^{-2}s^{-1}$ integrated in 70-130 nm region, for a plasma power density of 0.6 W/cm^2 [112]. For our reactor dimensions (length = 0.178 m diameter = 0.087 m) and power used in this study (420 W), the power density works out to 0.7 W/cm^2. Hence, the photon flux in our case is expected to be similar to the value

measured by Woodworth et al. A photo-assisted etching rate of 330 nm/min (in 50% Cl_2-50% Ar plasma) corresponds to a silicon flux of 4 x 10^{16} $cm^{-2}s^{-1}$. The etching yield was then calculated to be about one silicon atom etched per incident photon. The calculated yield is quite high and is similar to the numbers reported by Schwentner et al. in the etching of silicon with XeF_2 [79], indicating that the enhancement in etching is likely due to the photo-generated carriers.

4.6 Photo-assisted etching – Role of photo-generated carriers:

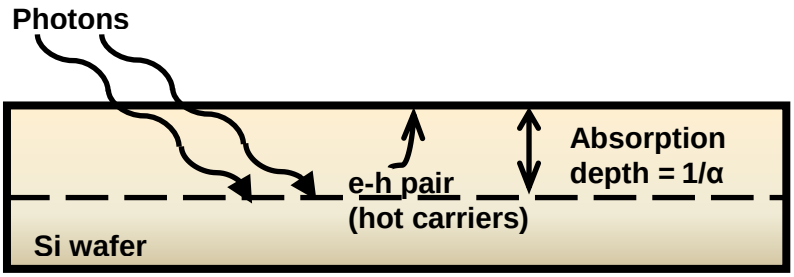

Figure 4.9: Formation of hot carriers by photon absorption.

Role of photons in laser induced etching has been discussed earlier (Chapter 2). One possible mechanism that could explain the large yields involves the role of energetic carriers (electrons/holes) in photo-assisted etching. Photons incident on any material are absorbed by the material. The penetration depth of the photons is inversely proportional to the absorption coefficient, which is a function of photon energy (or wavelength). For VUV radiation (photon energy > 7eV), the "1/e" penetration depth in silicon is ~ 8 nm as the absorption coefficient does not change much at high photon energies (see Fig. 2.1). Electron-hole pairs are created near the surface when photons of energy larger than the

band gap of silicon (1.1 V) impinge on the surface (Figure 4.9). The electrons and holes created are quite energetic, and the partitioning of the excess energy is given by [113]

$$\Delta E_e = \frac{h\nu - E_g}{1+\frac{m_e^*}{m_h^*}} \text{ and} \tag{4.1}$$

$$\Delta E_h = \frac{h\nu - E_g}{1+\frac{m_h^*}{m_e^*}}, \tag{4.2}$$

where m_e^* and m_h^* are the effective masses of the electron and hole, respectively, and *Eg* is the bandgap (1.12 eV for Si at room temperature). m_e^*/m_e and m_h^*/m_e for Si, based on the density of states, are 1.08 and 0.56, respectively,[114] with m_e being the electron rest mass. Hence, ΔE_e = 0.34($h\nu - E_g$) and ΔE_h = 0.66($h\nu - E_g$); it is obvious that smaller wavelengths result in the formation of hot carriers. For 120 nm radiation, the energy of photo-generated electron and hole are 3.14 eV and 6.1 eV respectively.

The photo-generated hot carriers lose their energy quite rapidly (~1 ps) through carrier phonon interactions and equilibrate to the lattice temperature [23]. At the same time, they can also diffuse through the lattice in any direction, or drift under the influence of an electric field. Carrier Diffusivity was estimated from the carrier mobility at 300 K for doping level of 10^{15} cm^{-3} ($D_{electron} \approx 40$ cm^2/s, $D_{hole} \approx 25$ cm^2/s) using Einstein's relation [115]. The difference in carrier mobilities creates an electric field causing band bending, which can further affect carrier diffusion. Neglecting the effect of band bending for the moment, the distance that the hot carriers diffuse in the time needed for carrier thermalization is ~ 36 nm (holes) and ~ 60 nm (electrons) using equation 2.7. These distances are much larger than 8 nm penetration depth of the photon. Thus, it is possible

that a considerable fraction of hot carriers can reach the surface before they thermalize to lattice temperature. These hot carriers may still possess sufficient energy to enhance surface processes (reaction, desorption). The hot carriers that do not diffuse towards the surface may thermalize in the bulk. The thermalized carriers continue to diffuse until they are lost due to recombination.

Based on the above discussion, it is apparent that any radiation which has a wavelength smaller than the band gap wavelength (~ 1100 nm) must be capable of generating hot carriers. From Fig. 2.1, the threshold for light absorption for Si is about 2 eV, with absorption rising considerably over 3.2 eV (~ 415 nm). Absorption reaches a maximum at a photon energy of 4.5 eV (~ 275 nm). Beyond 4.5 eV, absorption drops and continues to drop slowly with photon energy. This indicates that all radiation below 415 nm must be able to induce hot carriers. However, based on the low etching rates observed under the fused silica window, it is obvious that photo-assisted etching is quite inefficient at wavelengths greater than 170 nm. Optical emission spectrum recorded during silicon etching is shown in Chapter 6 (Fig. 5.1). Apparently, there is very little photoemission occurring in the 200-400 nm range. Thus, the contribution to photo-assisted etching in our plasmas is mainly from radiation < 200 nm, which is also consistent with the higher etching rates observed under the MgF_2 window.

In the above discussion regarding the creation of hot carriers, effects of band bending were neglected. Presence of surface states (e.g. dangling bonds) can cause a pinning of the Fermi level resulting in band bending. For a p-type semiconductor, bands

bend downward (Fig. 4.10). This downward band bending imposes a barrier on the photo generated holes to keep them from reaching the surface.

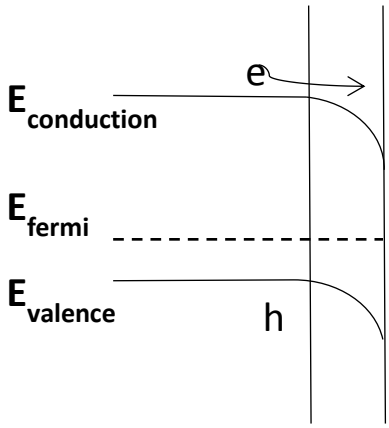

Figure 4.10: Band bending of p-type silicon due to pinning of surface states

The band bending imposes an energy barrier (E_b) on holes. On the other hand, electrons are accelerated by

$$E_b \approx \tfrac{1}{2}E_g + k_B T ln[N_A/N_V], \tag{4.3}$$

where N_V = 1.8 x 10^{19} cm^{-3} is the density of states at the top of the valence band, k_B is the Boltzmann constant, T is substrate temperature, and N_A (acceptor number density) ≈ 10^{15} for the Si samples used. E_b is thus calculated to be ~0.3 eV. Electrons generated by VUV photons (ΔE_e ~ 3eV) acquire additional energy (0.3 eV) due to band bending. Due to their high energy, they have a low probability of undergoing recombination with holes before reaching the surface. These electrons, however, still do not have sufficient energy to break Si-Si bonds (4 eV) and cause etching. On the other hand, holes generated by VUV photons have sufficient energy (~ 6 eV) to overcome the energy barrier due to band bending (~0.3 eV), and could to reach the surface. Band bending will also influenced by

the electron withdrawing Cl atoms adsorbed on the surface, electric fields imposed on the sample (substrate bias, sheath potential in the plasma), and incident photon radiation. Due to the various factors involved, it can be very difficult to predict the extent of band bending (upward, downward or flat band condition) present during etching.

For etching to occur, photo-generated carriers must reach the surface. However, it is possible that they can undergo recombination in the bulk or at the surface before taking part in the etching reactions. The various bulk recombination mechanisms (radiative, Auger, Shockley-Read-Hall recombination) and effective lifetimes has been discussed (Ch. 2, Section 2.4.4). At low excess carrier concentrations, the trap assisted Shockley-Read-Hall recombination is dominant. The effective carrier lifetime is ~ 10 - 100 μs. In addition to bulk recombination, surface recombination rates must also be considered here. Silicon etched in high density plasmas have shown to exhibit very short carrier lifetimes indicating very high surface recombination probability. Hence surface recombination is likely to be the dominant recombination mechanism. Increased surface recombination may be the reason for the suppression of photo-assisted etching with increasing ion energy (Fig. 4.5). Si etched under sub-threshold etching conditions was found to be very rough especially in Br_2/Ar plasmas. It is only likely that a number of recombination sites were introduced on the roughened surface. Perhaps, this is another reason for observing very low photo-assisted etching rates in 50% Br_2/Ar plasmas.

On reaching the surface, the energetic carriers may participate in etching reactions. Energetic holes may weaken Si-Si back bonds facilitating desorption of the etch product ($SiCl_x$). The hole could also rupture a strained Si-Si bond releasing

additional electrons, facilitating in the chemisorption of chlorine to form a chlorinated layer. The exact nature of the mechanism requires knowledge of the main etching products desorbing from the surface. The energetics of desorption process would determine the major desorption product. Thus, surface reactions induced by VUV photon-generated holes could explain the high etching yields.

Chapter 5 – Further Insights into the mechanism of in-plasma photo-assisted etching using optical emission spectroscopy

5.1 Introduction

A number of studies have been carried out to elucidate the role of UV photons in etching silicon *in the absence of plasma*. Photo-assisted etching of silicon in a halogen environment has been studied extensively using UV lasers as the light source. Most of these studies attributed photo-assisted etching to the creation of electron-hole pairs and reactions of these carriers at the surface [59], [73]. Other researchers have proposed that VUV photons possess sufficient energy (> 7eV) to enhance photo-desorption, thereby facilitating etching [13]. Photon induced damage was reported for thin films of SiO_2[86], and SiCOH [91], [92] due to scission of Si-O and Si-C bonds, respectively. UV irradiation was found to enhance etching of silicon using a chlorine atom beam, and was attributed to generation of crystal defects that promoted silicon etching by Cl atoms in the damaged layer [84].

The two processes discussed above should behave differently in that carrier-mediated etching should cease rapidly after the plasma is extinguished and photo-generated carriers decay rapidly, while etching caused by defects should continue after the plasma is extinguished until the damaged layer etches away. This can be verified by modulating the plasma power between two different values at a rate that is much faster than that required to remove a monolayer. Defects (broken Si-Si bonds) created by VUV photons when the plasma is operated at a higher power, would remain even after the

plasma power is turned down, as it takes longer for the plasma to etch one monolayer compared to the power modulation period. The defect sites would therefore not be modulated, nor would the Cl number density [116], and etching would continue at a high rate even after plasma power is turned down (when surface damage due to VUV photons is presumably lower).

On the other hand, if etching were mediated by photo-generated carriers, then etching would be proportional to the instantaneous carrier density. If the carrier recombination occurs at a rate that is higher than the power modulation frequency, then carrier density should be modulated in proportion to light intensity. Minority carrier recombination near the surface will dominate, and be fast on these highly defective surface layers. Minority carrier lifetimes of ~10 μs have been reported [117] on native oxide covered Si surfaces, hence carrier lifetimes in plasma-exposed Si will be <<10 μs. Light intensity is proportional to the product of plasma electron density (n_e) and the electron impact excitation rate coefficient for producing emission, which is a function of electron temperature (T_e). T_e should be nearly independent of power and n_e will be proportional to power. Therefore, a carrier-mediated PAE etching rate should be proportional to power over much of the modulation period. A concerted, photo-stimulated desorption process will behave in a similar manner.

In this work, we use optical emission spectroscopy (OES), in an effort to gain insight into the mechanism of in-plasma photo-assisted etching of Si. The light intensity of key emitting radicals was monitored in both continuous wave and pulsed plasmas.

5.2 Experimental

The apparatus consisted of a Faraday shielded inductively coupled plasma (ICP) powered by a 3 turn copper coil, as described previously [9]. Radio frequency (RF) power (13.56 MHz) was delivered to the plasma by a RF amplifier (ENI A500) that was driven by a function generator (HP 3325A). For some experiments, the plasma was modulated between a "high" and "low" power at 1 kHz with 50% duty cycle. A Cl_2/Ar gas mixture was fed through the electrically grounded top flange. The fraction of chlorine in the gas mixture was varied between 10% and 71% by changing Ar flow rate for a fixed Cl_2 flow of 25 sccm. A needle valve was employed to introduce a trace amount of $SiCl_4$ gas for some experiments. The pressure downstream from the ICP source was measured using a capacitance manometer (MKS 629). Pressure above the sample (corrected for the pressure drop between the ICP source and the point at which the measurement was made) was maintained at 60 mTorr using a throttle valve. At this pressure, with no bias applied to the substrate, it is expected that very few ions will have energies above the ion-assisted etching threshold of silicon (~ 16 eV) [118].

The sample to be etched (p-Si (100), resistivity = 5-50 ohm/cm) was cleaved into small pieces (approximately 1.5 cm^2), cleaned with acetone and methanol to remove carbon contaminants, followed by dipping in 48% HF to strip the native oxide, and was dried by blowing dry nitrogen. The cleaned sample was fixed to a 1" diameter stainless steel sample holder using carbon tape to ensure good electrical contact. The sample holder was mounted on a water cooled rod that served to maintain the sample at a fixed temperature, and transferred into the plasma, where it was held against a grounded stage.

OES was used to monitor the light intensity of key emitting species (Si-288.1 nm, Ar-750.4 nm, Cl-724 nm, SiCl-280.3 nm, and Cl_2 band centered at 305 nm). A periscope, comprising of two right angle prisms (1 × 1 cm along the perpendicular faces), was employed to collect light integrated over a region ~1 cm above the Si surface. The light was imaged with lenses (magnification slightly smaller than 1:1) onto a 1 cm long, vertically oriented entrance slit of a monochromator. The scanning monochromator had a 1200 grooves/mm diffraction grating which, combined with entrance and exit slit widths of 100 μm, produced a resolution of 2 Å full width at half maximum (FWHM). The dispersed light was detected by a GaAs photomultiplier tube (RCA C31034). For time resolved emission measurements, current from the photomultiplier tube was measured as the voltage drop across a 3 kΩ resistor using an oscilloscope. The system RC time constant of ~ 0.3μs, was very small compared to the time of flight (~10 μs) of etching products across the 1 cm region over which light was collected. For low intensity emissions (e.g., Si), the slits of the monochromator were set to 500 μm, yielding a resolution of 10 Å FWHM.

5.3 Results and Discussion

5.3.1 Silicon Etching in Cl_2/Ar plasmas with continuous wave (cw) power

A p-type silicon substrate was etched in a 50%Cl_2/50%Ar plasma at a pressure of 60 mTorr without substrate bias. The contribution of ion-assisted etching was negligible under these conditions. In addition, Cl atoms do not etch p-type silicon spontaneously at room temperature [111]. Hence, photo-assisted etching was the prevailing mode of etching [9], [118]. An emission spectrum recorded while etching at a power of 350W is

shown in Fig. 5.1. SiCl peaks at 280.3 and 282.1 nm and a Si peak at 288.1 nm are observed due to etching of the Si substrate, as observed previously [9], [118]. (It should be pointed out that if the bare Si substrate is replaced with a SiO_2-coated Si sample, the Si and SiCl emissions are not detected.) The broad emission band corresponding to $SiCl_2$ (band centered ~ 323.5 nm) is not observed, and emission corresponding to $SiCl_3$ (band centered at ~385.5 nm) is not clearly distinguished from other broad emitters in this region (Cl_2 and Cl_2^+). Cl_2 emission bands near 255 and 305 nm can also be seen clearly. Several lines expected for Ar are observed between 700 and 900 nm, where the vast majority of emission is from Cl.

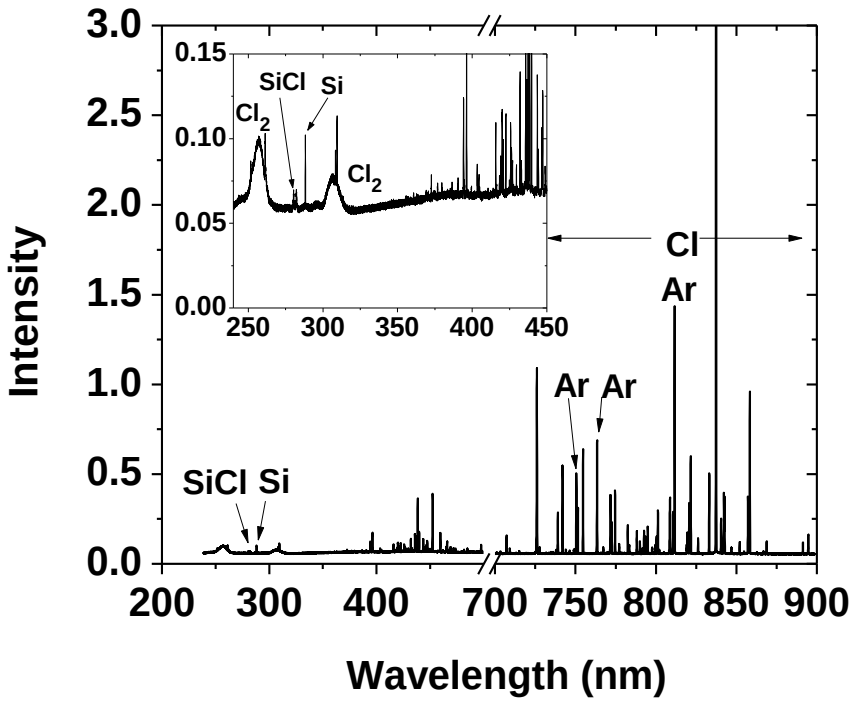

Figure 5.1: Optical emission spectrum (200-900 nm) recorded while etching silicon in 50%Cl_2/50%Ar plasma. ICP Power = 350 W.

Optical emissions from SiCl (280.3 nm), Si (288.1 nm), Cl (792.4 nm) and Ar (750.4 nm) were recorded as a function of power and gas composition (Fig. 5.2). Not surprisingly, the Ar emission intensity increases with power and %Ar in the feed gas. The super-linear increase in intensity with increasing %Ar is attributed mainly to the increasing electron-to-Cl^- number density ratio between 29% and 90% Ar. Also, since the Ar 750.4 nm emission is produced when the 4p'[1/2] level at 13.48 eV decays to the 4s'[1/2]^o level at 11.83 eV, that in turn decays to the ground state by emitting the most intense of the VUV Ar emissions at 104.8 nm, it follows that the relative intensity of the Ar VUV emission is expected to depend on power in a manner similar to that for the 750.4 nm emission shown in Fig. 5.2.

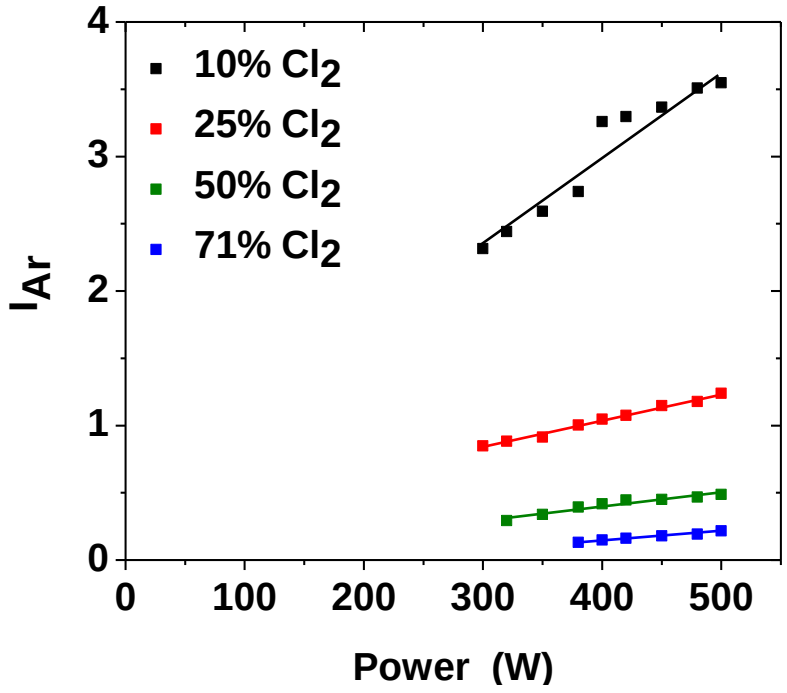

Figure 5.2: Ar (750.4 nm) intensity as a function of power at a total pressure of 60 mTorr for different gas compositions.

Cl/Ar emission intensity ratios (I_{Cl}/I_{Ar}) are presented in Fig. 5.3. Since the Cl_2 feed gas is probably substantially dissociated, and the electron temperature is rather low at 60 mTorr, the higher-energy process of dissociative excitation of Cl_2 to produce Cl emission [119] is expected to be negligible. Hence, I_{Cl}/I_{Ar} is expected to be proportional to Cl number density. At a given power, I_{Cl}/I_{Ar} scales nearly with the Cl_2 to Ar feed gas ratio. At higher %Cl_2, I_{Cl}/I_{Ar} increases sub-linearly with power, as might be expected. For chlorine addition <50%, however, I_{Cl}/I_{Ar} is independent of power, suggesting that Cl_2 is mostly dissociated into Cl, as observed elsewhere [119], [120].

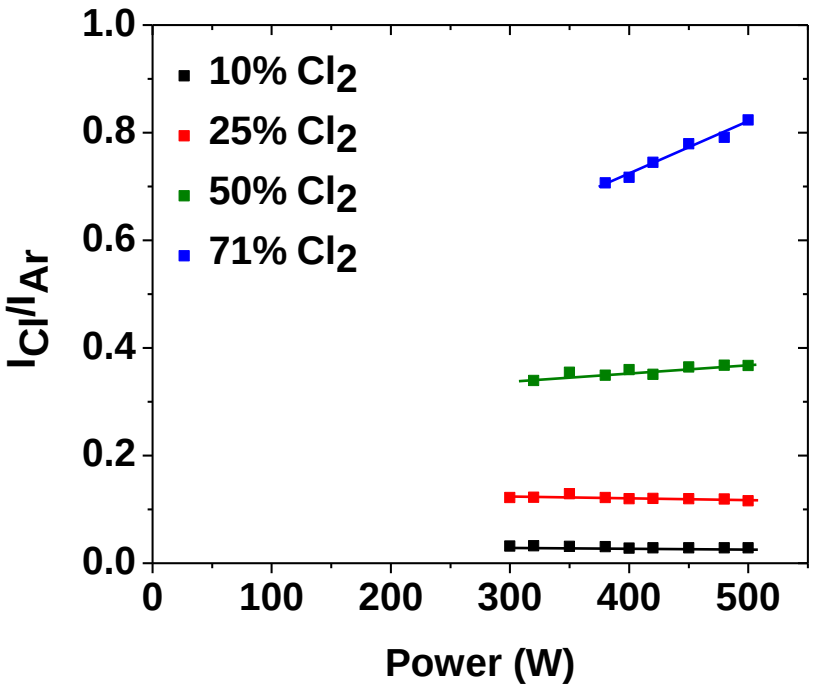

Figure 5.3: I_{Cl}/I_{Ar} as a function of power for different gas compositions.

Emission intensity ratios for Si/Ar (I_{Si}/I_{Ar}) and SiCl/Ar (I_{SiCl}/I_{Ar}) are presented in Figs. 5.4 and 5.5, respectively. Si and SiCl emission intensities are expected to arise, at least in part, from electron impact excitation of these species, and to therefore scale, at

least qualitatively, with their relative number densities in the plasma. These emissions can also come from electron-impact dissociative excitation of more highly chlorinated species such as $SiCl_2$. Previously it was shown that Si emission intensity was directly proportional to etching rate, which was varied by changing substrate bias power at constant ICP power, pressure, and feed gas composition [9], [118]. In the present study, I_{Si}/I_{Ar} increases with power, especially at higher Cl_2 percentages. Since the VUV photon flux to the substrate increases with power between 300 and 500 W (assumed proportional to the 750.4 nm Ar line intensity), the increase in I_{Si}/I_{Ar} likely reflects an increasing photo-assisted Si etching rate.

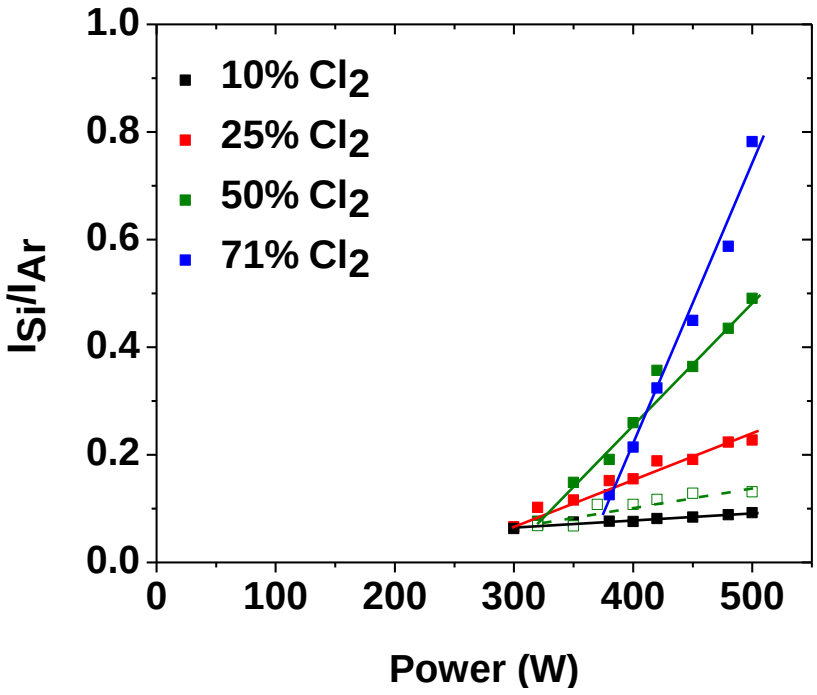

Figure 5.4: I_{Si}/I_{Ar} as a function of power for different gas compositions. Open squares denote I_{Si}/I_{Ar} when a trace amount of $SiCl_4$ gas was added to the gas mixture with no Si substrate present.

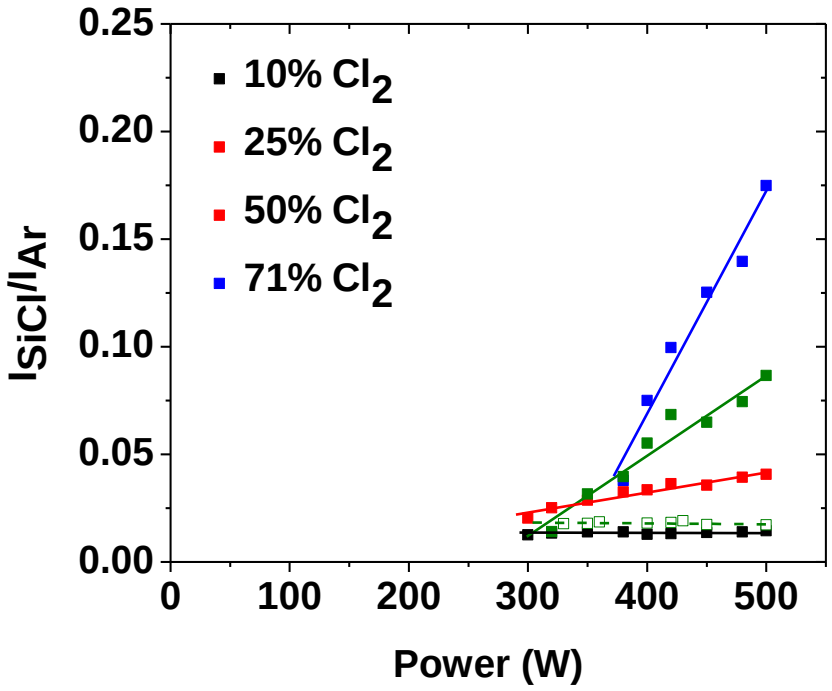

Figure 5.5: I_{SiCl}/I_{Ar} as a function of power for different gas compositions at 60 mTorr without substrate bias. Open squares denote I_{SiCl}/I_{Ar} when a trace amount of $SiCl_4$ gas was added to the gas mixture with no Si substrate present.

It is also expected that some of the $SiCl_x$ (x=1-4) etching products increasingly dissociate (eventually producing Si) with increasing power, contributing to an increase in I_{Si}/I_{Ar}. To determine how much of the rise in I_{Si}/I_{Ar} with increasing power is due to the increasing dissociation of $SiCl_x$ (x=1-4) etching products (eventually producing Si), a trace amount of $SiCl_4$ gas was introduced in a 50%Cl_2/50%Ar gas mixture, with no Si substrate present, to simulate the dissociation of $SiCl_x$ etching products. At 320 W, a flow of 0.3 sccm $SiCl_4$ was found to produce a I_{Si}/I_{Ar} value equal to that observed during Si etching in a 320 W 50%Cl_2/50%Ar plasma. As power was then increased from 320 to 500 W, I_{Si}/I_{Ar} increased ~2-fold (red open squares in Fig. 5.4). During Si etching (with no added $SiCl_4$), however, I_{Si}/I_{Ar} increased ~6.5-fold between 320 and 500W (red solid

squares in Fig. 5.4). If half of this increase is due to fragmentation of etching products, then a remaining factor of ~3.2 is attributed to an increase in etching rate. This is somewhat in excess of the ~1.9 fold increase in the product of VUV (using the 750.4 nm Ar line as surrogate) and Cl fluxes determined from Figs. 5.2 and 5.3, respectivelyGiven the large mismatch in energies of the levels involved in Ar and Si emission (13.5 [121] and 5 eV [122], respectively), the remaining unexplained factor of ~1.8 increase with power is perhaps not surprising.

The dependence of I_{Si}/I_{Ar} on power is much stronger with increasing Cl_2 percentage. This trend can be qualitatively explained as a transition from chlorine-starved conditions at 10% Cl_2 addition, where etching is limited by the flux of Cl and Cl_2, and is nearly independent of VUV flux, to chlorine-saturated conditions at 70% Cl_2 addition, where etching is limited by photon flux and depends less on chlorine flux. Additional complications in relating I_{Si}/I_{Ar} to etching rate at higher Cl_2 percentages, due to changes in the electron energy distribution and the mismatch in threshold energies to excite the Ar and Si emitting levels (see above), precludes quantitative interpretations. The trends in I_{SiCl}/I_{Ar} as a function of power and gas composition are very similar to those in I_{Si}/I_{Ar} vs. power and gas composition (Fig. 5.5). This implies that I_{SiCl}/I_{Ar} is also proportional to the Si etching rate.

5.3.2 Silicon Etching in Cl_2/Ar plasmas with pulsed power

The results presented above would be consistent with either the lattice damage or carrier mediated processes discussed earlier. To distinguish between these two mechanisms, Si was etched in a power-modulated plasma. Power delivered to the ICP

coil was switched between 500 and 300 W at a frequency of 1 kHz and 50% duty cycle at 60 mTorr without substrate bias. The etching rate at 400 W was reported to be 330 nm/min at 60 mTorr in a previous publication [118]. During the 500 μs period at 500 W, approximately 0.00275 nm of Si is removed, which is about 1% of a monolayer. The density of any defects created by the VUV photons would not be altered during this period. In addition, the chlorine coverage on the surface would not change significantly (see below). Therefore, photo-assisted etching due to a photon-induced damage mechanism would not be modulated. Conversely, for a carrier-mediated etching mechanism, the etching rate would be modulated in proportion to the VUV flux, and therefore power, since the carrier lifetime is << 500 μs [117].

Time resolved emission intensities of Ar, Si, SiCl, Cl, and Cl_2 were recorded during etching of a Si sample (Fig. 5.6). As the plasma power is modulated from 500W to 300W, emissions were also found to modulate. At 500W, Ar emission intensity rises quickly and reaches a quasi-steady state level which is about twice that at 300W. This modulation in intensity is comparable to the factor of 1.66 (500/300) modulation in the plasma power, and is attributed to the change in electron density with plasma power. Similar behavior is observed for the Cl emission. Si and SiCl emissions rise and fall at slower rates, relative to Ar and Cl emissions. This is ascribed to the slower modulation in the population of low energy electrons capable of exciting Si and SiCl emissions.

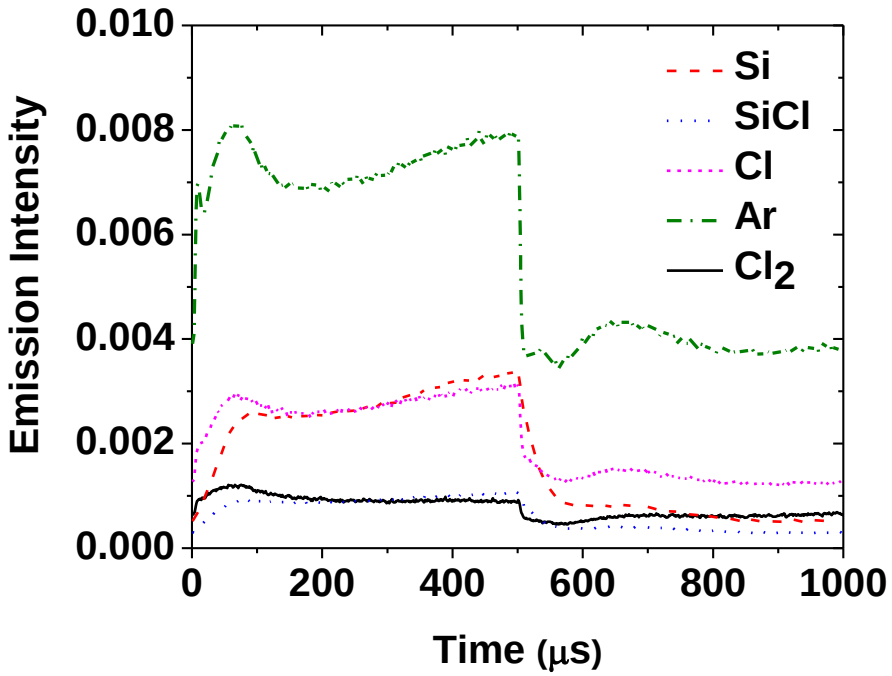

Figure 5.6: Time resolved optical emission of Ar, Cl, Si, SiCl and Cl_2 recorded while etching Si in a 50%Cl_2/50%Ar pulsed plasma.

Time-resolved emission intensities for Cl, Si and SiCl, normalized to Ar emission, are presented in Fig. 5.7. I_{Cl}/I_{Ar} exhibits small spikes when power first changes, but then settles to values that are nearly equal at high and low power. Conversely, when power drops from 500 W to 300 W, I_{Si}/I_{Ar} spikes but finally settles to a quasi-steady value that is about 25% of that at 500W. I_{SiCl}/I_{Ar} exhibits similar but less pronounced trends, settling to a value at the end of the 300W period that is about 0.6 that at 500 W. The more pronounced spikes accompanying power switching are due to the lower-energy emitting levels of Si and SiCl being less sensitive to rapid transients in T_e, compared with Ar. The modulation in I_{Si}/I_{Ar} and I_{SiCl}/I_{Ar} suggests that the Si etching rate is also modulated.

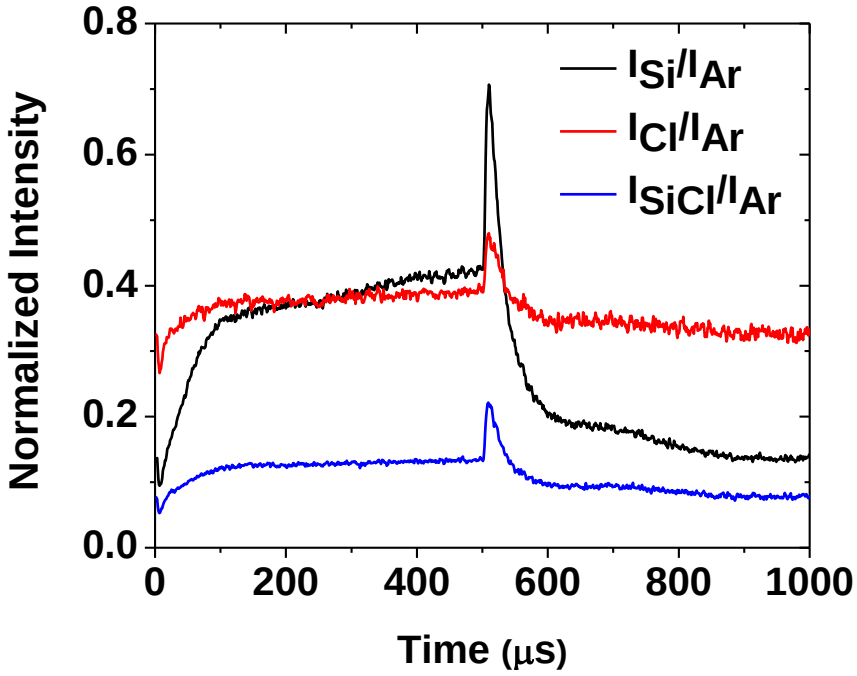

Figure 5.7: Time resolved normalized emission intensities recorded during Si etching in a 50%Cl_2/50%Ar pulsed plasma.

The time response of the normalized emission intensities may be understood by considering the localized and global Si production and loss mechanisms. For an etching rate of 330 nm/min (measured under similar conditions [118]), the flux of Si-containing products is f_{SiClx} = 2.78 x 10^{16} $cm^{-2}s^{-1}$. For the 1.5 cm^2 sample, this corresponds to a flow rate of 0.092 sccm. For the Cl_2 and Ar feed gas flow rates of 25 and 25 sccm (50%Cl_2/50%Ar), the total flow rate through the reactor is between 50 sccm (if no Cl_2 dissociation) and 75 sccm (for complete dissociation in Cl atoms). Taking the average of the two, the mole fraction of Si etching products released into the reactor is 0.092/67 = 1.37 x 10^{-3}. An upper limit to the partial pressure in the reactor (if no Si products deposit on the walls) is then 0.08 mTorr at the total pressure of 60 mTorr. If the gas temperature

is 600 K, then this corresponds to a number density of about 1.4 x 10^{12} cm^{-3} for the background etching product gas in the chamber.

The number density above the sample will be enriched in primary products of Si etching. The mean free path at 60 mTorr is ~0.1 cm, thus at a distance of l = 1 cm from the surface, desorbing products will be escaping by ordinary diffusion. An effective diffusion coefficient D_{eff} was estimated from [123]

$$D_{eff}^{-1} = D_{bin}^{-1} + \frac{3}{\Lambda v_{th}}, \tag{5.1}$$

where D_{bin} is the binary diffusion coefficient for the species of interest in Ar and v_{th} is mean thermal velocity. Λ is the characteristic diffusion length given by

$$\frac{1}{\Lambda^2} = \left(\frac{\pi}{L}\right)^2 + \left(\frac{2.405}{R}\right)^2, \tag{5.2}$$

where L = 0.178 m is the length and R = 0.043 m is the radius of the plasma chamber. Λ was calculated to be 0.017 m. At 600K and 60mTorr, D_{bin} for $SiCl_3$, $SiCl_2$, SiCl and Si in Ar was estimated to be 0.357, 0.408, 0.523, and 0.448 m^2/s, respectively, from Chapman-Enskog theory [124], using Lennard Jones parameters [125].

The steady state concentration of products at a distance of 1 cm from the substrate surface is roughly $f_{SiClx}\, l/D_{bin}$ = 6.2 x $10^{12}cm^{-3}$, where the diffusion coefficient, D_{bin} for Si is ~4480cm^2s^{-1} at 60 mTorr. This product number density is therefore 4.4 times larger than the product concentration in the background gas. In addition, the time it takes for products to reach the 1 cm distance from the surface is l^2/D =225 μs, or about the time it takes for I_{Si}/I_{Ar} and I_{SiCl}/I_{Ar} in Fig. 7 to reach quasi-steady state after power changes from 500 to 300 W. The conclusion that the Si and SiCl concentration is enriched near the

surface is also supported by the fact that only 0.092 sccm of the equivalent product flow rate from etching in a 50%Cl_2/50%Ar plasma at 320 W produces the same I_{SiCl}/I_{Ar} value as that obtained from the addition of 0.3 sccm of $SiCl_4$ background gas, as discussed above. The calculated ratio is 0.3/0.092=3.3, which is comparable to the factor of 4.4 found above.

The loss of silicon etch products in the plasma is due to pumping, as well as reactions on the walls. At 60 mTorr and 50 sccm, the gas residence time within the combined ~10 *l* volume of the plasma chamber and tubing above the pump is ~1s, much longer than the modulation period. For a cylindrical chamber, the loss to the walls by diffusion and reaction is given by [126]

$$\frac{1}{k_d} = \frac{\Lambda^2}{D_{eff}} + \frac{V}{A}\frac{2(2-\gamma)}{\gamma v_{th}}, \tag{5.3}$$

where, *V/A* is the volume to surface area ratio of the chamber, γ is the probability that the species (etch product) sticks to the wall. Si and SiCl have a wall sticking probability greater than the higher chlorides of the silicon etch product [127], [128]. Assuming that they are lost at the walls (and probably converted to higher chlorides that subsequently desorb) with a 50% probability (i.e., γ = 0.5), then $1/k_d$ is estimated to be ~ 14 and 9 s for Si and SiCl, respectively. Since this is much longer than the modulation period, the etch products in the background gas would not be modulated. This was verified by monitoring the emission signals (Fig. 9) through a window on the boundary electrode that is about 10 cm away from the sample stage. I_{Si}/I_{Ar} was recorded while etching silicon in a pulsed plasma. The signal modulated by a factor of 1.67 (≈ power ratio) which is similar to the modulation of the signal recorded with a trace amount of $SiCl_4$, where the Si emission is

solely due to the dissociation of $SiCl_4$. Also, this modulation in Si emission intensity is less compared to modulation in the intensity as observed in the vicinity of the substrate (Fig. 5.7). This also serves as strong evidence that the region close to the surface is locally enriched in Si etch products as discussed earlier.

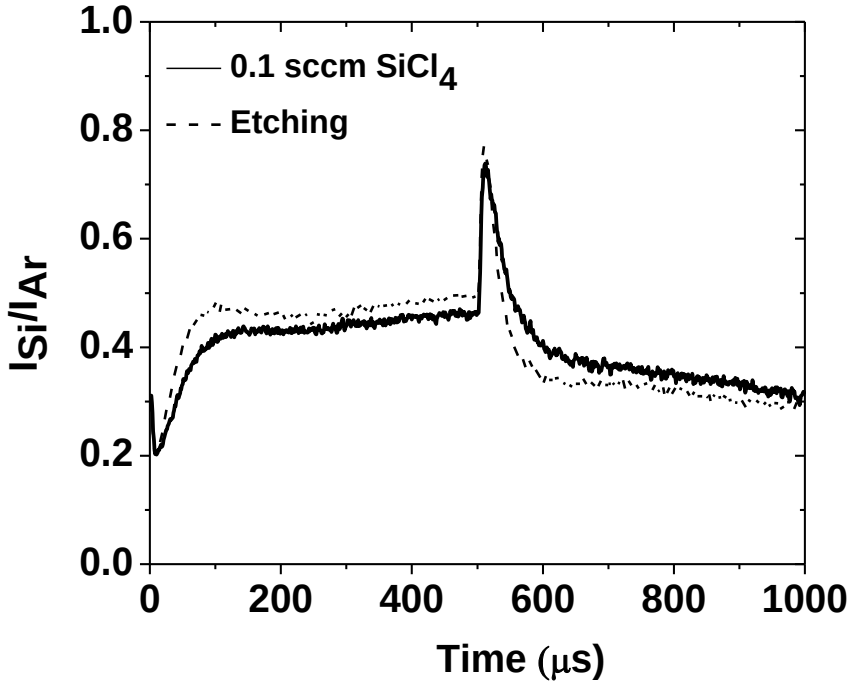

Figure 5.8: I_{Si}/I_{Ar} recorded from a window on the top flange. The modulation of the signal in the background gas (thicker line) is due to the dissociation of the etch products alone (no Si sample present).

The rate constant for the loss of Cl atoms to the walls by diffusion and recombination was also estimated from equation (3) to be 0.32 s^{-1} for a recombination coefficient of γ=0.1. This gives a time constant for this loss process of ~3 s, much greater than the 1 ms pulse period. Therefore, the I_{Cl}/I_{Ar} intensity ratio (proportional to the Cl atom density) recorded in the pulsed plasma is hardly modulated (Fig. 5.7).

Assuming that the Si and SiCl emission signals are mostly coming from species that have not reached the walls and become part of the background gas, we can finally determine how the instantaneous etching rate scales with instantaneous power. As given above (Fig. 5.7), I_{Si}/I_{Ar} is 3.8 times higher at 500 W than at 300 W. To remove the portion of this increase that is due to increased fragmentation of $SiCl_x$ products at higher power, we note that I_{Si}/I_{Ar} produced by adding a trace of $SiCl_4$ to the Cl_2/Ar feed gas with no Si substrate present is 2.2 times higher at 500 W, compared with 300 W (derive from a linear least squares fit to the open red squares in Fig. 4). Thus the corrected increase in I_{Si}/I_{Ar}, which is expected to reflect the relative change in instantaneous etching rate, is 3.8/2.2 = 1.7, which is comparable to the ratio of powers (1.67), as well as the ratio of Ar emission at 750.4 nm (2.0 from Fig. 5.6) that is assumed to be proportional to the VUV flux. Similarly for I_{SiCl}/I_{Ar}, the corrected rise is 1.7 between 300 and 500 W (using the data in Figs. 5.5 and 5.7). Therefore, it appears that the instantaneous etching rate is proportional to the instantaneous VUV flux.

Lastly, it has to be mentioned that the ratio of I_{Si}/I_{Ar} (Fig. 4) in a continuous wave (cw) plasma at 500 W to that at 300 W ($0.491/0.076 \approx 6.5$), is higher than the ratio of the quasi-steady state values of I_{Si}/I_{Ar} (Fig. 7) in a pulsed plasma operating between 500 and 300 W ($0.43/0.13 \approx 3.4$). This implies that, under the conditions used, the modulation period of the pulsed plasma is not long enough to reach the plateau that would be obtained in a cw plasma, under otherwise the same operating conditions. This in turn suggests that a long time scale process (e.g. changing wall conditions) may be at play.

5.3.3 Global Model

A 0-D (global) model was developed based on the work of Gudmundsson et al. [129], [130]. Particle and energy balance equations were setup based on the particle creation and loss processes. These equations were solved to obtain the electron temperature (assuming Maxwellian EEDF) and number densities of various species in the plasma. Details of the model including the reaction set used are discussed in appendix B.

Simulation results as a function of plasma power were compared the optical emission signals recorded experimentally. Assuming that the excited state is produced solely by e-impact excitation of the species of interest (e.g., no dissociative excitation), the emission intensity (I) is proportional to the electron density (n_e), neutral density of the species of interest ($n_{x,}$ x= Ar, Cl), and excitation cross sections (see equation 3.1). Therefore, a comparison between the product of the calculated neutral and electron densities with the recorded emission intensity is reasonable, i.e., $I = \beta\, n_e\, n_x$ where β is a constant. Also, the ratio of emission intensities is proportional to the ratio of absolute number densities, provided the excitation thresholds and cross section shapes of the two species are similar. Figure 5.9 shows that the simulation results (n_e x n_{Ar}) and the Ar emission intensity observed experimentally match quite well. With n_{Ar} decreasing slightly with power, the increase in I_{Ar} is mainly due to increasing electron density (Fig 5.10) as explained earlier (section 5.3.1).

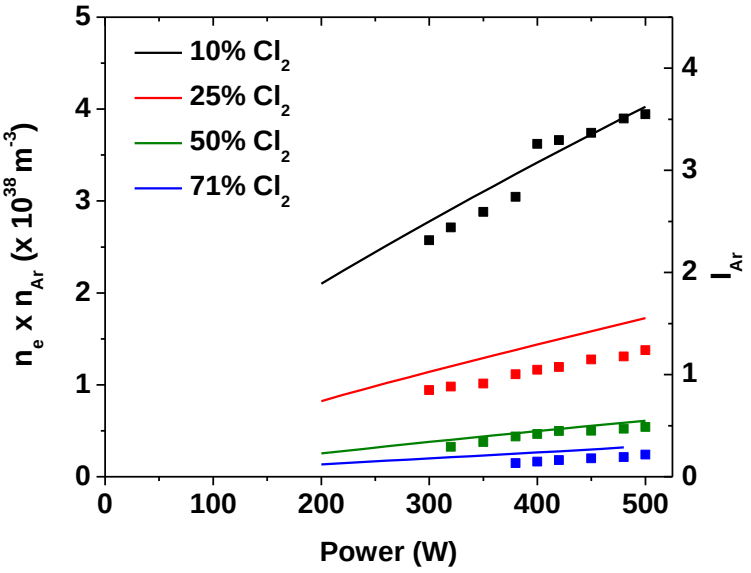

Figure 5.9: A comparison of experimental Ar emission intensities (solid symbols) with values calculated from the model (lines) as a function of plasma power for different feed gas compositions.

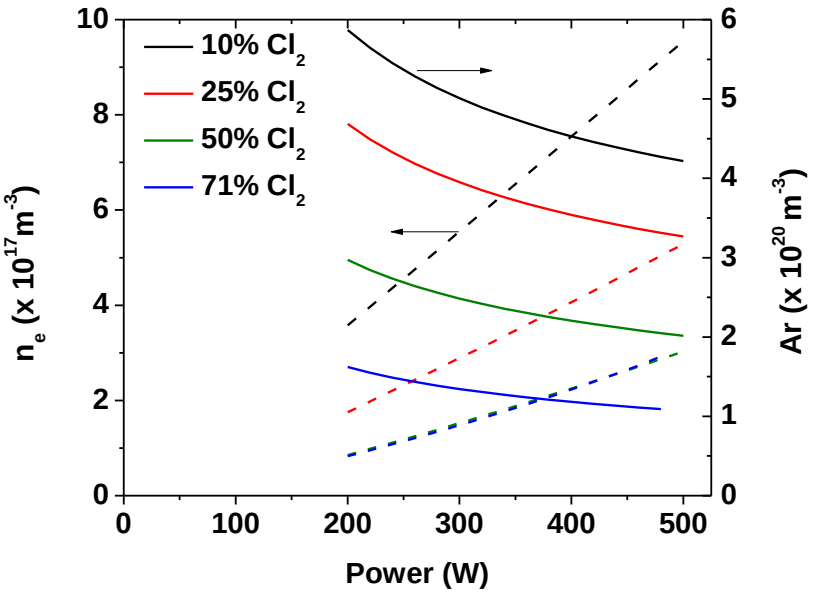

Figure 5.10: Calculated electron density (dashed lines), and neutral argon density (solid lines) as a function of plasma power for different feed gas compositions.

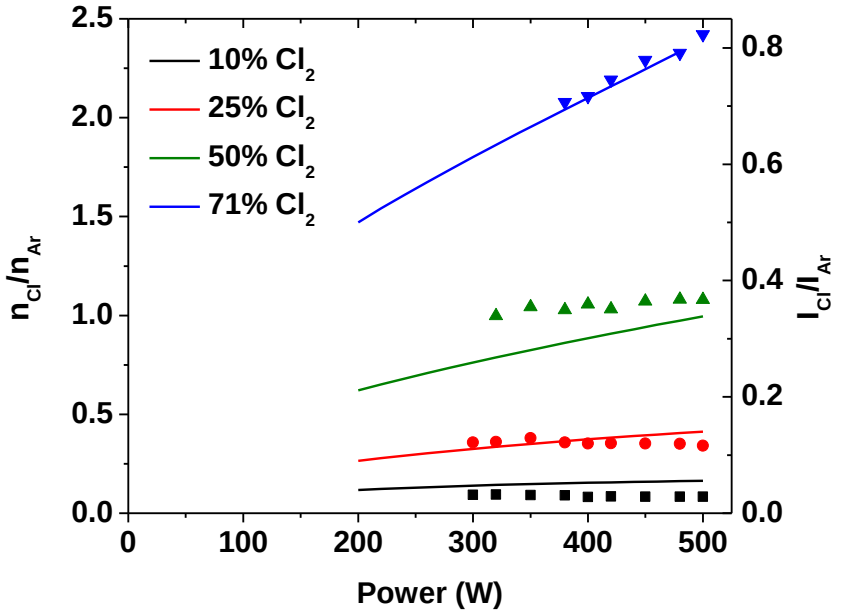

Figure 5.11: A comparison between the ratio of emission intensities (I_{Cl}/I_{Ar}) observed experimentally (solid symbols) and the calculated ratio (lines) of number densities (n_{Cl}/n_{Ar}), as a function of plasma power for different feed gas compositions.

Figure 5.11 shows that the measured ratio of emission intensities (I_{Cl}/I_{Ar}) matches the calculated ratio of the corresponding number densities (n_{Cl}/n_{Ar}). With n_{Ar} being nearly constant (Fig. 5.10), I_{Cl}/I_{Ar} tracks n_{Cl} in the plasma. It was assumed in the experiments that the contribution to Cl emission due to dissociative excitation of Cl_2 was negligible (Fig 5.3). This assumption was validated through the calculations, which revealed that dissociation increased with power (Fig. 5.12). For low Cl_2 fraction in the gas mixture, Cl was the dominant neutral species (Fig. 5.13). As Cl_2 content in the gas mixture increased, the dominant neutral species depends on plasma power. However, for the range of powers employed in the experiments (300 – 500W), n_{Cl} was higher than n_{Cl2} except for 71% Cl_2, where Cl is the dominant species for powers greater than 400W. Nevertheless,

n_{Cl} and n_{Cl2} are comparable for all the experimental conditions, and contribution to Cl emission from dissociative excitation of Cl_2 will be negligible.

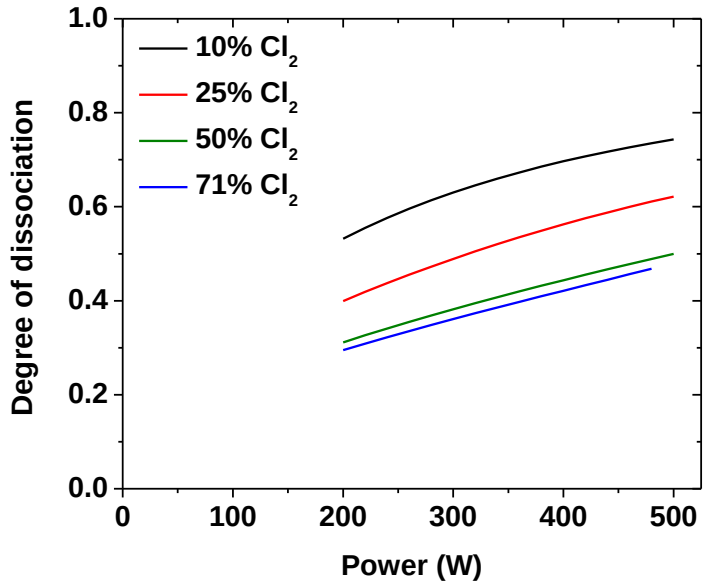

Figure 5.12: Degree of dissociation of Cl_2 into Cl as a function of power.

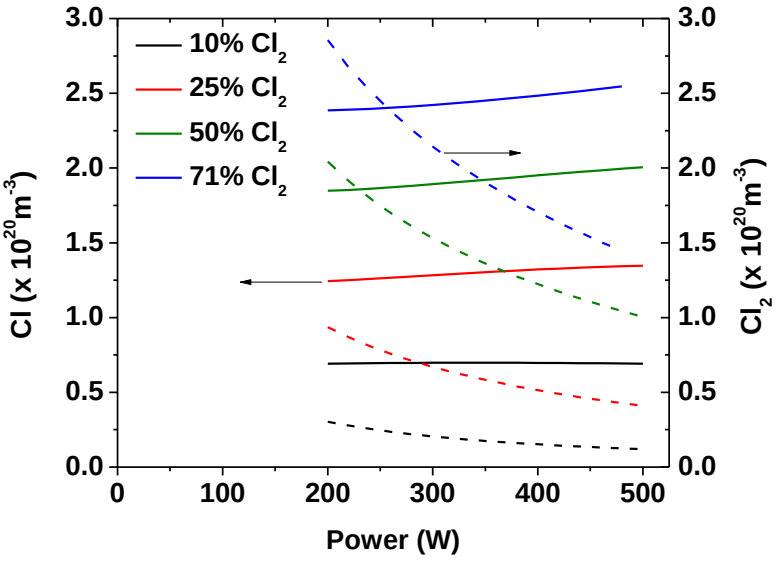

Figure 5.13: n_{Cl} (solid lines) and n_{Cl2} (dashed lines) for different gas compositions.

The number density of radiatively coupled levels (Ar $1s_4$ and $1s_2$) which de-excite to emit VUV photons were also calculated using the model (Fig, 5.14). The density of the radiative states (n_{rad}) increased with power by a factor of 1.6 between 300W and 500W in 71%Cl_2/29%Ar and 50% Cl_2/50% Ar plasmas, and was nearly a constant in the range 300 - 500 W for the 10%Cl_2/90%Ar plasma. These results correlate well with trends in I_{Si}/I_{Ar} observed in Fig. 5.4, where the emission ratio increased by a factor of 3.2, after accounting for dissociation of etching products. The discrepancy in the increase in I_{Si}/I_{Ar} to the increase in the VUV photon flux may be due to the mismatch in the excitation thresholds for Si compared to Ar, as described earlier. Also, the 0-D model may not be a good representation of the actual radiation transport occurring in the actual system.

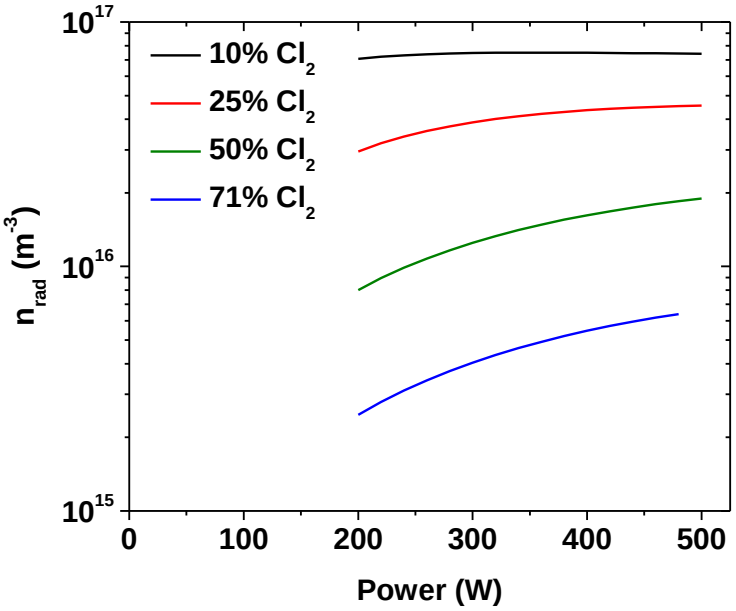

Figure 5.14: Density of radiative states (Ar $1s_4$ and Ar $1s_2$) computed from the model at different powers and gas composition.

In a pulsed plasma where power was modulated between 500 W and 300 W, the density of radiative states modulated by a factor of ~ 1.5 (Fig. 5.15), which is nearly equal to the modulation of Si emission intensity observed experimentally after accounting for the dissociation of etch product. The computed Cl number density did not modulate during the pulsing period and was nearly a constant. Hence, any enhancement in the observed Si emission with power while etching in a pulsed plasma must be due to photo-assisted etching.

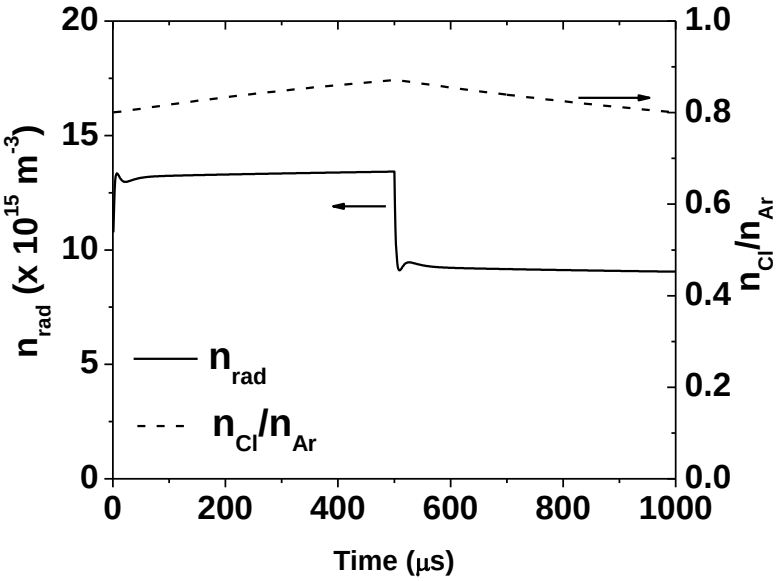

Figure 5.15: Density of radiative states in a pulsed plasma where power is modulated between 500W and 300W. Also shown is the ratio n_{Cl}/n_{Ar} which is representative of I_{Cl}/I_{Ar} observed in the experiments (Fig. 5.7)

Chapter 6 – Summary, Conclusions, and Future Directions

6.1 Summary and Conclusions

Etching of p-type Si was studied in different halogen containing plasmas. At ion energies below the ion assisted etching threshold, etching persisted. This sub-threshold etching was determined to be due to photo-assisted etching caused by VUV photons generated in the plasma; some isotropic chemical etching was detected in HBr containing plasmas and was attributed to Si etching by H atoms. Photo-assisted etching was found to be lowest in Br_2/Ar (~ 100 nm/min) and highest for HBr/Cl_2/Ar (~ 400 nm/min). The photo-assisted etching rates was proportional to the product of halogen coverage on the surface and the VUV photon flux indicated by the Ar 750.4 nm emission intensity.

Etching was also studied under different window materials with different light transmission characteristics. Fused silica, MgF_2, and opaque windows were used. A 50% Cl_2/50% Kr plasma was used for this experiment as the window materials are opaque to the Ar VUV lines at 104.8 nm and 106.4 nm. Etching was found to be minimal under the opaque window as most of the light was blocked. Etching rates observed under a fused silica window were comparable to those observed under the opaque window. This similarity suggests that etching is important for wavelengths lower than the fused s transmission cut-off. Higher etching rates were measured under the MgF_2 window which confirmed that high energy photons (low wavelength) were more efficient in inducing etching.

Etching rates were also measured as a function of the substrate bias under the different windows. A dependence of the ion assisted etching threshold on the window material was found. The etching threshold was found to be lower for opaque and fused silica windows and a similar higher threshold was observed for etching under MgF_2 window and without a window. At high values of substrate bias (ion energies greater than 60eV), etching rates under the different window materials were comparable, suggesting that photo-assisted etching was unimportant and ion assisted etching was dominant. These results obtained for etching underneath windows imply a negative synergy between ion bombardment and photo-assisted etching. It is postulated that increasing ion bombardment produces defect sites on the surface which acts as recombination centers for photo-generated carriers, thus reducing photo-assisted etching.

The morphology of the etched Si substrates was studied using Atomic Force Microscope. Generally, the surface of the etched substrates was rough, especially in bromine containing plasmas. The roughness was attributed to residual contaminants on the surface which act as micro-masks and prevent etching of underlying Si. On the other hand, etching in a Cl_2/Ar plasma was found to be relatively smooth, but interspersed with pyramid-shaped features. Analysis of line profiles showed that [110] planes made the four sides of the pyramid with the base of the pyramid along the <100> direction.

Based on the measured photo-assisted etching rates, the etching yield for silicon in a chlorine plasma was found to be approximately one Si atom per incident photon. Such high etching yields have never been reported for UV laser induced etching of Si using Cl_2. (no plasma). Comparing the high etching yields with those reported in the literature

[75]–[81] it is apparent that the photo generated carriers play a major role in enhancing etching. The exact nature of interaction between the photo induced carriers and the substrate can be very complicated, especially in a plasma environment. Various factors such as VUV light intensity, substrate doping level, electric fields (sheath potential), presence of an electronegative adsorbate at the surface, and ion bombardment can influence the electronic band structure which in turn affects the carrier generation, diffusion and recombination processes. Thus a careful study on the influence of the various parameters is necessary to understand their effect on etching.

In addition to the role of photo generated carriers, other mechanisms such as photon-induced damage (breaking of Si-Si bonds) [84] have been proposed to explain etching enhancement due to photons. To gain insight on the importance of this mechanism in PAE, the light intensity from key species (Si, Ar, Cl, SiCl) was monitored in both continuous wave (cw) and pulsed plasmas. The emission intensity ratio I_{Si}/I_{Ar} (proportional to the silicon number density), was found to increase with plasma power during silicon etching in cw plasmas. In order to account for the contribution to this signal from the dissociation of silicon etch products, a trace amount of $SiCl_4$ gas was introduced into the plasma (without Si substrate present) to simulate the emission of etch product. With added $SiCl_4$, it was found that the ratio I_{Si}/I_{Ar} increased roughly by a factor of two, which was smaller compared to the six fold increase observed while etching silicon (no added $SiCl_4$). This super-linear increase in the signal may be attributed to the addition of silicon etch products into the plasma due to PAE that increases with power. The increase in PAE with power is due to the corresponding increase in the VUV photon flux to the substrate.

Time resolved emission was also recorded during Si etching in a pulsed plasma where the power was modulated between 500W and 300W. The time evolution of the signal (I_{Si}/I_{Ar}) over the pulse period was explained based on the rate of production and loss of the silicon etch products. It was found that the region in the immediate vicinity of the sample, where the emission signals were recorded, was enriched with the etching products in comparison to the reactor bulk. The contribution to the signal due to back diffusion of the etching products was minimal, and any modulation of the signal was mainly due to the modulation of the PAE rate with power. The observation of a substantially modulated I_{Si}/I_{Ar} signal rules out a damage-induced mechanism of in-plasma PAE since, if this mechanism was dominant, I_{Si}/I_{Ar} would not be modulated.

A global model was developed to validate the experimental observations. Experimentally observed ratios of emission intensities were found to scale with the ratio of number densities. Density of the radiative states (n_{rad}) was also calculated with the global model which correlated well with the enhancement of Si emission. In a pulsed plasma, modulation of n_{rad} was similar to modulation of experimentally observed Si emission after accounting for dissociation of Si etch products. This provides further evidence supporting photo-assisted etching.

6.2 Future work

6.2.2 PAE mechanisms

Photo-assisted etching has been studied extensively and has been attributed mainly to creation of electron-hole pairs and the ensuing surface reactions induced by these carriers.

These studies were performed in the absence of a plasma, however. The mechanistic details of photo-assisted etching in a plasma environment are still not clear. In particular, there may be synergetic (or anti-synergetic) effects among ions, electrons, neutrals and photons that can only happen in the presence of a plasma. For example, lattice defects due to ion bombardment can act as recombination centers for photon-generated carriers, thus reducing the efficiency of photo-assisted etching. Such loss of carriers to recombination was observed in the reduction of laser-induced photoluminescence of GaAs etched in BCl_3 plasma [109]. A similar effect also seems to be occurring in Fig. 4.5, where there is an apparent shift in the threshold for ion- assisted etching under a MgF_2 window. Ion bombardment at energies above the ion-assisted etching threshold disrupts the silicon lattice producing defect sites which enhance carrier recombination, in turn reducing the PAE rate. At ion energies just above threshold, PAE is suppressed further; the suppression of PAE may be nearly balanced by the increasing ion-assisted etching. Eventually, the PAE rates goes to zero and ion-assisted etching dominates. The net effect of the gradual suppression of PAE due to ion bombardment results in an apparent shift in the threshold for ion-assisted etching under MgF_2 window.

This anti-synergistic effect will be explored further by applying a pulsed bias on the substrate stage. Relative etching rates will be monitored over the bias pulse duration through the Si emission signal at 288.1 nm. When the bias is turned on, ion bombardment may disrupt the lattice producing carrier recombination centers. Just after the bias is turned off (0V), the carriers will not be effective in inducing etching due to recombination at these defect sites. Thus, etching will proceed at a much lower rate. For sufficiently long bias-off period, the etching rate would increase to the prevailing PAE rate. The creation of defects due to ion bombardment will also be studied using GaN by monitoring the photoluminescence generated by light from a laser or plasma source. A decrease in the intensity of photoluminescence would suggest increased rate of non-radiative recombination of carriers at defect sites.

6.2.3 Synergy with Plasma - Band bending due to external field

Surface states induced pinning of Fermi level results in band bending. Bands bend downward for p-type and upward for n-type semiconductors. When a semiconductor substrate is immersed in plasma, the plasma sheath combined with the substrate bias imposes an external field on the semiconductor which further affects band bending [39]. This would in turn influence the electric field in the chlorinated silicon layer, and hence affect the transport properties of charged species/carriers. For example, Electrons that arrive at the silicon interface tunnel through the energy barrier and are accelerated by fields in the sheath to be injected into plasma. Electrons may attach on to chlorine atoms to form Cl- ions which then diffuse into silicon lattice due to the electric field and enhance etching. Band bending due to externally applied field also depends on plasma parameters (substrate bias, plasma potential), doping and nature of the surface which changes with increasing ion bombardment. This may be verified by measuring etch rate for substrates with different dopant levels. Changes in band bending due to ion bombardment may be monitored by photoluminescence spectroscopy.

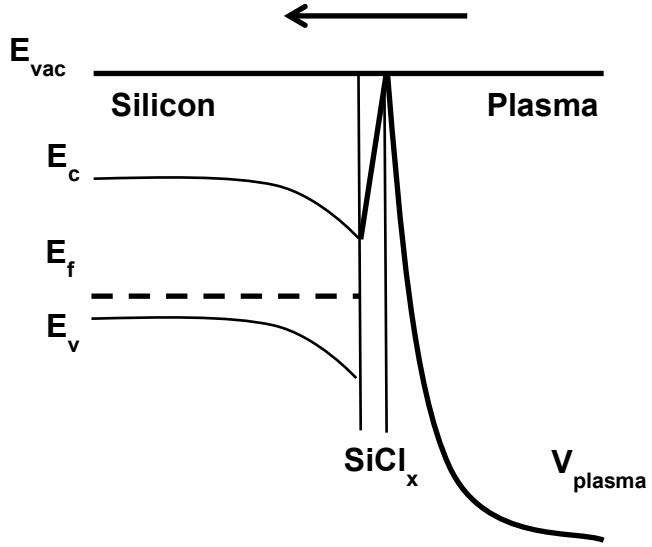

Figure 6.1: Semiconductor band bending in plasma

6.2.4 Tandem Plasmas

A tandem ICP reactor (Fig. 6.2) is being designed to study photo-assisted etching. It consists of two faraday shielded plasma sources separated by grids/UV transmitting window. The new reactor also includes a movable stage that can be used to vary the distance of the sample from the plasma, thus varying the flux of VUV photons striking the substrate. A pinhole on the stage also enables communication between the plasma source and a differentially pumped chamber that may be connected to a VUV spectrometer/ion energy analyzer. The VUV spectrometer in addition to the existing UV-Vis spectrometer would enable recording of the full spectrum of plasma emission from 30 – 900nm.

The auxiliary source acts as a lamp that produces light, spectrum of which can be measured. Experiments with different window materials (CaF_2, LiF, MgF_2, fused silica) separating the two plasma sources may be carried out to study the etching in different range of wavelengths. Different inert gases (Ar, Xe, Kr, Ne) may be used to generate different wavelengths of light striking the substrate, which in combination with the different window materials can be used to study the efficiency of etching at different wavelengths. Experiments may also be carried out without any window material and using biased grids instead, that would prevent ions/electrons from reaching the substrate. This offers the advantage of transmitting all wavelengths in the VUV region due to absence of transmitting windows which generally have a cutoff transmission wavelength ~ 100nm.

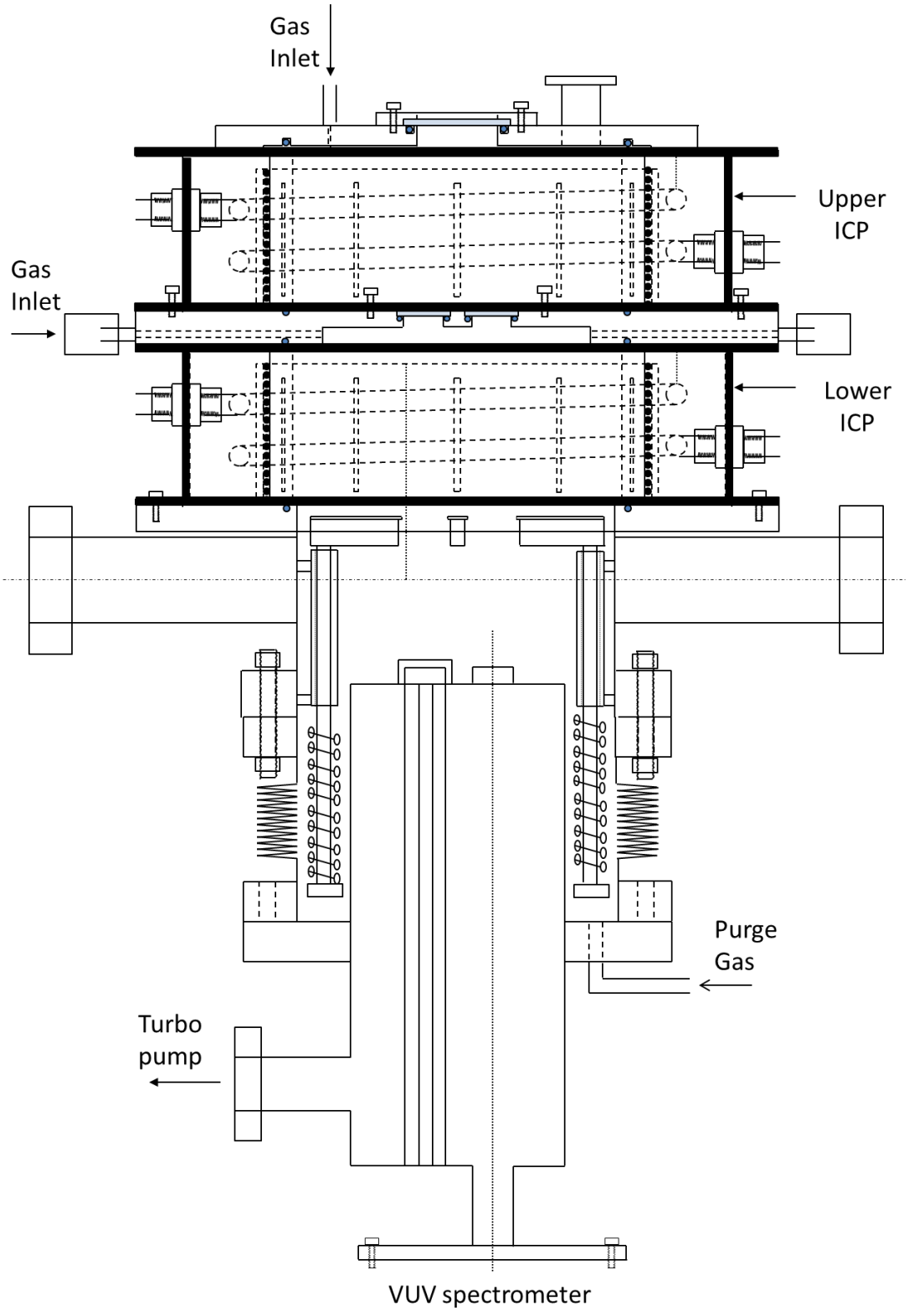

Figure 6.2: Tandem Inductively Coupled Plasma.

References

[1] H. Jansen, H. Gardeniers, M. de Boer, M. Elwenspoek, and J. Fluitman, "A Survey on the Reactive Ion Etching of Silicon in Microtechnology," *J. Micromechanics Microengineering*, vol. 6, no. 1, pp. 14–28, Mar. 1996.

[2] G. E. Moore, "Cramming More Components onto Integrated Circuits," *Proc. IEEE*, vol. 86, no. 1, pp. 82–85, 1998.

[3] S. D. Athavale and D. J. Economou, "Realization of Atomic Layer Etching of Silicon," *J. Vac. Sci. Technol. B*, vol. 14, no. 6, 1996.

[4] G. S. Oehrlein, D. Metzler, and C. Li, "Atomic Layer Etching at the Tipping Point: An Overview," *ECS J. Solid State Sci. Technol.*, vol. 4, no. 6, pp. N5041–N5053, Mar. 2015.

[5] L. Xu, D. J. Economou, V. M. Donnelly, and P. Ruchhoeft, "Extraction of a Nearly Monoenergetic Ion Beam Using a Pulsed Plasma," *Appl. Phys. Lett.*, vol. 87, no. 4, pp. 28–30, 2005.

[6] B. A. Smith and L. J. Overzet, "Ion Energy Control in an Insulating Inductively Coupled Discharge Reactor," *Appl. Phys. Lett.*, vol. 70, no. 15, pp. 1950–1952, 1997.

[7] S.-B. Wang and A. E. Wendt, "Control of Ion Energy Distribution at Substrates During Plasma Processing," *J. Appl. Phys.*, vol. 88, no. 2, p. 643, 2000.

[8] H. Shin, W. Zhu, L. Xu, V. M. Donnelly, and D. J. Economou, "Control of Ion Energy Distributions Using a Pulsed Plasma with Synchronous Bias on a

Boundary Electrode," *Plasma Sources Sci. Technol.*, vol. 20, no. 5, p. 055001, 2011.

[9] H. Shin, W. Zhu, V. M. Donnelly, and D. J. Economou, "Surprising Importance of Photo-Assisted Etching of Silicon in Chlorine-Containing Plasmas," *J. Vac. Sci. Technol. A*, vol. 30, no. 2, 2012.

[10] L. J. Richter and R. R. Cavanagh, "Mechanistic Studies of Photoinduced Reactions at Semiconductor Surfaces," *Prog. Surf. Sci.*, vol. 39, no. 2, pp. 155–226, 1992.

[11] T. J. Chuang, "Laser-Induced Gas-Surface Interactions," *Surf. Sci. Rep.*, vol. 3, no. 1, pp. 1–105, 1983.

[12] Y. Horiike, N. Hayasaka, M. Sekine, T. Arikado, M. Nakase, and H. Okano, "Excimer-Laser Etching on Silicon," *Appl. Phys. A Solids Surfaces*, vol. 44, no. 4, pp. 313–322, Dec. 1987.

[13] W. Sesselmann, E. Hudeczek, and F. Bachmann, "Reaction of Silicon with Chlorine and Ultraviolet Laser Induced Chemical Etching Mechanisms," *J. Vac. Sci. Technol. B*, vol. 7, no. 5, 1989.

[14] E. J. Heilweil, M. P. Casassa, R. R. Cavanagh, and J. C. Stephenson, "Picosecond Vibrational Energy Transfer Studies of Surface Adsorbates," *Annu. Rev. Phys. Chem.*, vol. 40, no. 1, pp. 143–171, Oct. 1989.

[15] C. T. Rettner, D. J. Auerbach, J. C. Tully, and A. W. Kleyn, "Chemical Dynamics at the Gas−Surface Interface," *J. Phys. Chem.*, vol. 100, no. 31, pp. 13021–13033, Jan. 1996.

[16] T. J. Chuang, "Multiple Photon Excited SF_6 Interaction with Silicon Surfaces," *J.*

Chem. Phys., vol. 74, no. 2, p. 1453, 1981.

[17] A. L. Linsebigler, A. L. Linsebigler, J. T. Yates Jr, G. Lu, G. Lu, and J. T. Yates, "Photocatalysis on TiO_2 Surfaces: Principles, Mechanisms, and Selected Results," *Chem. Rev.*, vol. 95, no. 3, pp. 735–758, 1995.

[18] D. K. Schroder, R. N. Thomas, and J. C. Swartz, "Free Carrier Absorption in Silicon," *IEEE Trans. Electron Devices*, vol. 25, no. 2, pp. 254–261, 1978.

[19] R. R. L. Zucca and Y. R. Shen, "Wavelength-Modulation Spectra of Some Semiconductors," *Phys. Rev. B*, vol. 1, no. 6, pp. 2668–2676, Mar. 1970.

[20] H. R. Philipp and E. A. Taft, "Optical Constants of Silicon in the Region 1 to 10 eV," *Phys. Rev.*, vol. 120, no. 1, pp. 37–38, Oct. 1960.

[21] H. A. Weakliem and D. Redfield, "Temperature Dependence of the Optical Properties of Silicon," *J. Appl. Phys.*, vol. 50, no. 3, pp. 1491–1493, 1979.

[22] A. Sabbah and D. Riffe, "Femtosecond Pump-Probe Reflectivity Study of Silicon Carrier Dynamics," *Phys. Rev. B*, vol. 66, no. 16, pp. 1–11, 2002.

[23] F. E. Doany and D. Grischkowsky, "Measurement of Ultrafast Hot-Carrier Relaxation in Silicon by Thin-Film-Enhanced, Time-Resolved Reflectivity," *Appl. Phys. Lett.*, vol. 52, no. 1, pp. 36–38, 1988.

[24] C. Li, T. Sjodin, and H. Dai, "Photoexcited Carrier Diffusion Near a Si(111) Surface: Non-Negligible Consequence of Carrier-Carrier Scattering," *Phys. Rev. B*, vol. 56, no. 23, pp. 15252–15255, Dec. 1997.

[25] J. Dziewior and D. Silber, "Minority-Carrier Diffusion Coefficients in Highly Doped Silicon," *Appl. Phys. Lett.*, vol. 35, no. 2, pp. 170–172, 1979.

[26] M. Born, R. J. Blin-Stoyle, and J. M. Radcliffe, *Atomic Physics*. Courier Corporation, 1989.

[27] R. Brunetti, C. Jacoboni, F. Nava, L. Reggiani, G. Bosman, and R. J. J. Zijlstra, "Diffusion Coefficient of Electrons in Silicon," *J. Appl. Phys.*, vol. 52, no. 11, pp. 6713–6722, 1981.

[28] W. Shockley and W. T. Read, "Statistics of the Recombinations of Holes and Electrons," *Phys. Rev.*, vol. 87, no. 5, pp. 835–842, Sep. 1952.

[29] W. van Roosbroeck and W. Shockley, "Photon-Radiative Recombination of Electrons and Holes in Germanium," *Phys. Rev.*, vol. 94, no. 6, pp. 1558–1560, Jun. 1954.

[30] A. Richter, S. W. Glunz, F. Werner, J. Schmidt, and A. Cuevas, "Improved Quantitative Description of Auger Recombination in Crystalline Silicon," *Phys. Rev. B - Condens. Matter Mater. Phys.*, vol. 86, no. 16, pp. 1–14, Oct. 2012.

[31] S. C. Baker-Finch, "Recombination Calculator," 2014. [Online]. Available: https://www2.pvlighthouse.com.au/calculators/recombination calculator/recombination calculator.aspx.

[32] T. Trupke, M. A. Green, P. Würfel, P. P. Altermatt, A. Wang, J. Zhao, and R. Corkish, "Temperature Dependence of the Radiative Recombination Coefficient of Intrinsic Crystalline Silicon," *J. Appl. Phys.*, vol. 94, no. 8, 2003.

[33] S. Selberherr, *Analysis and Simulation of Semiconductor Devices*. Springer Science & Business Media, 2012.

[34] Y. J. Chabal, "Infrared Spectroscopy of Si(111) and Si(100) Surfaces after HF

Treatment: Hydrogen Termination and Surface Morphology," *J. Vac. Sci. Technol. A Vacuum, Surfaces, Film.*, vol. 7, no. 3, p. 2104, May 1989.

[35] E. Yablonovitch, D. L. Allara, C. C. Chang, T. Gmitter, and T. B. Bright, "Unusually Low Surface-Recombination Velocity on Silicon and Germanium Surfaces," *Phys. Rev. Lett.*, vol. 57, no. 2, pp. 249–252, Jul. 1986.

[36] G. Kumaravelu, M. M. Alkaisi, D. MacDonald, J. Zhao, B. Rong, and A. Bittar, "Minority Carrier Lifetime in Plasma-Textured Silicon Wafers for Solar Cells," *Sol. Energy Mater. Sol. Cells*, vol. 87, no. 1–4, pp. 99–106, 2005.

[37] H. Lüth, *Solid surfaces, Interfaces and Thin Films*, vol. 4. Springer, 2001.

[38] A. Zangwill, *Physics at Surfaces*. Cambridge university press, 1988.

[39] Z. Zhang and J. T. Yates, "Band Bending in Semiconductor Chemical and Physical Consequences at Surfaces and Interfaces," *Chem. Rev.*, vol. 112, pp. 5520–5551, 2012.

[40] E. O. Johnson, "Large-Signal Surface Photovoltage Studies with Germanium," *Phys. Rev.*, vol. 111, no. 1, pp. 153–166, Jul. 1958.

[41] Z. Zhang and J. T. Yates, "Direct Observation of Surface-Mediated Electron-Hole Pair Recombination in TiO2(110)," *J. Phys. Chem. C*, vol. 114, no. 7, pp. 3098–3101, 2010.

[42] K. Ozawa, M. Emori, S. Yamamoto, R. Yukawa, S. Yamamoto, R. Hobara, K. Fujikawa, H. Sakama, and I. Matsuda, "Electron–Hole Recombination Time at TiO_2 Single-Crystal Surfaces: Influence of Surface Band Bending," *J. Phys. Chem. Lett.*, pp. 1953–1957, 2014.

[43] G. Agostinelli, A. Delabie, P. Vitanov, Z. Alexieva, H. F. W. Dekkers, S. De Wolf, and G. Beaucarne, "Very Low Surface Recombination Velocities on p-type Silicon Wafers Passivated with a Dielectric with Fixed Negative Charge," *Sol. Energy Mater. Sol. Cells*, vol. 90, no. 18–19, pp. 3438–3443, 2006.

[44] Z. Zhang and J. T. Yates, "Electron-Mediated CO Oxidation on the TiO_2 (110) Surface during Electronic Excitation," *J. Am. Chem. Soc.*, vol. 132, no. 37, pp. 12804–12807, Sep. 2010.

[45] Z. Zhang, W. Tang, M. Neurock, and J. John T. Yates, "Electric Charge of Single Au Atoms Adsorbed on TiO_2(110) and Associated Band Bending," *J. Phys. Chem. C*, vol. 115, no. 48, pp. 23848–23853, 2011.

[46] D. Menzel and R. Gomer, "Desorption from Metal Surfaces by Low Energy Electrons," *J. Chem. Phys.*, vol. 41, no. 11, 1964.

[47] P. A. Redhead, "Interaction of Slow Electrons with Chemisorbed Oxygen," *Can. J. Phys.*, vol. 42, no. 5, pp. 886–905, May 1964.

[48] P. R. Antoniewicz, "Model for Electron- and Photon-Stimulated Desorption," *Phys. Rev. B*, vol. 21, no. 9, pp. 3811–3815, May 1980.

[49] P. Avouris and R. E. Walkup, "Fundamental Mechanisms of Desorption and Fragmentation Induced by Electronic Transitions at Surfaces," *Annu. Rev. Phys. Chem.*, vol. 40, no. 1, pp. 173–206, Oct. 1989.

[50] F. A. Houle, "Photostimulated Desorption in Laser-Assisted Etching of Silicon," *Phys. Rev. Lett.*, vol. 61, no. 16, pp. 1871–1874, Oct. 1988.

[51] Z. Ying and W. Ho, "Photogenerated-Charge-Carrier-Induced Surface Reaction:

NO on Si(111)7×7," *Phys. Rev. Lett.*, vol. 60, no. 1, pp. 57–60, Jan. 1988.

[52] T. Rhodin, "Photochemical Desorption from Chlorinated Si(100) and Si(111) Surfaces — Mechanisms and Models," *Prog. Surf. Sci.*, vol. 50, no. 1–4, pp. 131–146, Dec. 1995.

[53] T. N. Rhodin and C. Paulsen-Boaz, "Energetics of Photoexcited Desorption from Chlorinated Si(100) and Si(111)," *Surf. Sci.*, vol. 363, no. 1–3, pp. 240–246, Aug. 1996.

[54] T. Baller, D. J. Oostra, A. E. de Vries, and G. N. A. van Veen, "Laser-Induced Etching of Si with Chlorine," *J. Appl. Phys.*, vol. 60, no. 7, p. 2321, 1986.

[55] K. Hattori, K. Shudo, T. Iimori, F. Komori, and Y. Murata, "Laser-Induced Desorption from Silicon (111) Surfaces with Adsorbed Chlorine Atoms," *J. Phys. Condens. Matt.*, vol. 8, pp. 6543–6551, 1996.

[56] S. Sakurai and T. Nakayama, "Electronic Structures and Etching Processes of Chlorinated Si(111) Surfaces," *Jpn. J. Appl. Phys.*, vol. 41, no. Part 1, No. 4A, pp. 2171–2175, 2002.

[57] X. H. Chen, J. C. Polanyi, and D. Rogers, "Photoetching of Si(111)-(7 × 7) Studied by STM," *Surf. Sci.*, vol. 376, no. 1–3, pp. 77–86, Apr. 1997.

[58] T. Kirimura, K. I. Shudo, Y. Hayashi, Y. Tanaka, T. Ishikawa, and M. Tanaka, "Photon-stimulated desorption from chlorinated Si(111): Etching of SiCl by picosecond-pulsed laser irradiation," *Phys. Rev. B - Condens. Matter Mater. Phys.*, vol. 73, no. 8, pp. 1–6, 2006.

[59] H. Okano, Y. Horiike, and M. Sekine, "Photo-Excited Etching of Poly-Crystalline

and Single-Crystalline Silicon in Cl_2 Atmosphere," *Jpn. J. Appl. Phys.*, vol. 24, no. Part 1, No. 1, pp. 68–74, Jan. 1985.

[60] C. J. Mogab and H. Levinstein, "Anisotropic Plasma Etching of Polysilicon," *J. Vac. Sci. Technol.*, vol. 17, no. 3, p. 721, 1980.

[61] G. C. Schwartz, "The Effects of Arsenic Doping in Reactive Ion Etching of Silicon in Chlorinated Plasmas," *J. Electrochem. Soc.*, vol. 130, no. 9, p. 1898, 1983.

[62] S. Berg, C. Nender, R. Buchta, and H. Norström, "Dry Etching of n- and p-type Polysilicon: Parameters Affecting the Etch Rate," *J. Vac. Sci. Technol. A*, vol. 5, no. 4, 1987.

[63] D. L. Flamm, P. L. Cowan, and J. A. Golovchenko, "Etching and Film Formation in CF_3Br Plasmas: Some Qualitative Observations and their General Implications," *J. Vac. Sci. Technol.*, vol. 17, no. 6, 1980.

[64] E. A. Ogryzlo, D. E. Ibbotson, D. L. Flamm, and J. A. Mucha, "Doping and Crystallographic Effects in Cl-atom Etching of Silicon," *J. Appl. Phys.*, vol. 67, no. 6, p. 3115, 1990.

[65] D. L. Flamm and V. M. Donnelly, "The Design of Plasma Etchants," *Plasma Chem. Plasma Process.*, vol. 1, no. 4, pp. 317–363, 1981.

[66] H. F. Winters and D. Haarer, "Influence of Doping on the Etching of Si(111)," *Phys. Rev. B*, vol. 36, no. 12, pp. 6613–6623, Oct. 1987.

[67] R. Kullmer and D. Bäuerle, "Laser-Induced Chemical Etching of Silicon in Chlorine Atmosphere," *Appl. Phys. A*, vol. 43, no. 3, pp. 227–232, 1987.

[68] P. Mogyorosi, K. Piglmayer, R. Kullmer, and D. Bäuerle, "Laser-Induced

Chemical Etching of Silicon in Chlorine Atmosphere," *Appl. Phys. A Solids Surfaces*, vol. 45, no. 4, pp. 293–299, Apr. 1988.

[69] R. B. Jackman, H. Ebert, and J. S. Foord, "Reaction Mechanisms for the Photon-Enhanced Etching of Semiconductors: An Investigation of the UV-Stimulated Interaction of Chlorine with Si(100)," *Surf. Sci.*, vol. 176, no. 1–2, pp. 183–192, Oct. 1986.

[70] F. A. Houle, "Photoeffects on the Fluorination of Silicon. I. Influence of Doping on Steady-State Phenomena," *J. Chem. Phys.*, vol. 79, no. 9, p. 4237, 1983.

[71] F. A. Houle, "Photoeffects on the Fluorination of Silicon. II. Kinetics of the Initial Response to Light," *J. Chem. Phys.*, vol. 80, no. 10, p. 4851, 1984.

[72] F. A. Houle, "A Reinvestigation of the Etch Products of Silicon and XeF_2: Doping and Pressure Effects," *J. Appl. Phys.*, vol. 60, no. 9, pp. 3018–3027, 1986.

[73] F. A. Houle, "Photochemical Etching of Silicon: The Influence of Photogenerated Charge Carriers," *Phys. Rev. B*, vol. 39, no. 14, pp. 10120–10132, May 1989.

[74] H. F. Winters and F. A. Houle, "Gaseous Products from the Reaction of XeF_2 with Silicon," *J. Appl. Phys.*, vol. 54, no. 3, pp. 1218–1223, 1983.

[75] U. Streller, A. Krabbe, and N. Schwentner, "Reaction Products in Synchrotron Radiation Induced Dry Etching of Ga and Cu," *Appl. Surf. Sci.*, vol. 110, no. June 1996, pp. 442–448, 1997.

[76] H. Raaf, M. Groen, and N. Schwentner, "Amplification in Light-Induced Reaction of Cu with Cl_2 in the VUV," *Appl. Surf. Sci.*, vol. 154, pp. 536–541, 2000.

[77] U. Streller, H. Raaf, and N. Schwentner, "Light-Induced Dry Etching of

Semiconductors in the Vacuum Ultraviolet," 1998, vol. 3274, no. 100, pp. 112–120.

[78] U. Streller, A. Krabbe, and N. Schwentner, "Selectivity in Dry Etching of Si(100) with XeF_2 and VUV Light," *Appl. Surf. Sci.*, vol. 106, pp. 341–346, 1996.

[79] B. Li, U. Streller, H. P. Krause, I. Twesten, and N. Schwentner, "Efficient Dry Etching of Si with Vacuum Ultraviolet Light and XeF_2 in a Buffer Gas," *J. Appl. Phys.*, vol. 77, no. 1, p. 350, 1995.

[80] U. Streller, B. Li, A. Krabbe, and N. Schwentner, "Photon-Induced Dry Etching of Si(100) in the VUV," *Appl. Surf. Sci.*, vol. 96–98, pp. 448–452, 1996.

[81] B. Li, I. Twesten, and N. Schwentner, "Photochemical Etching of GaAs with Cl_2 Induced by Synchrotron Radiation," *Appl. Phys. A Solids Surfaces*, vol. 57, no. 5, pp. 457–467, Nov. 1993.

[82] U. Streller, H. Raaf, and N. Schwentner, "Light-induced Dry Etching of Semiconductors in the Vacuum Ultraviolet," 1998, vol. 3274, no. 100, pp. 112–120.

[83] H. Dersch, J. Stuke, and J. Beichler, "Light-Induced Dangling Bonds in Hydrogenated Amorphous Silicon," *Appl. Phys. Lett.*, vol. 38, no. 6, pp. 456–458, 1981.

[84] S. Samukawa, B. Jinnai, F. Oda, and Y. Morimoto, "Surface Reaction Enhancement by UV irradiation during Si Etching Process with Chlorine Atom Beam," *Jpn. J. Appl. Phys.*, vol. 46, no. 1L, p. L64, 2007.

[85] R. J. Powell and G. F. Derbenwick, "Vacuum Ultraviolet Radiation Effects in

SiO_2," *IEEE Transactions on Nuclear Science*, vol. 18, no. 6. pp. 99–105, 1971.

[86] T. Yunogami, T. Mizutani, K. Suzuki, S. Nishimatsu, K. Tsujimoto, K. Suzuki, and S. Nishimatsu, "Radiation Damage in SiO_2/Si Induced by VUV Photons," *Jpn. J. Appl. Phys.*, vol. 28, no. Part 1, No. 10, pp. 2172–2176, Oct. 1989.

[87] T. Tatsumi, S. Fukuda, and S. Kadomura, "Radiation Damage of SiO_2 Surface Induced by Vacuum Ultraviolet Photons of High-Density Plasma," *Jpn. J. Appl. Phys.*, vol. 33, no. Part 1, No. 4B, pp. 2175–2178, 1994.

[88] S. Samukawa, Y. Ishikawa, S. Kumagai, and M. Okigawa, "On-Wafer Monitoring of Vacuum-Ultraviolet Radiation Damage in High-Density Plasma Processes," *Jpn. J. Appl. Phys.*, vol. 40, no. Part 2, No. 12B, pp. L1346–L1348, Dec. 2001.

[89] T. Yunogami and T. Mizutani, "Radiation Damage in SiO_2/Si Induced by Low-Energy Electrons Via Plasmon Excitation," *J. Appl. Phys.*, vol. 73, no. 12, pp. 8184–8188, 1993.

[90] S. Uchida, S. Takashima, M. Hori, M. Fukasawa, K. Ohshima, K. Nagahata, and T. Tatsumi, "Plasma Damage Mechanisms for Low- k Porous SiOCH Films due to Radiation, Radicals, and Ions in the Plasma Etching Process," *J. Appl. Phys.*, vol. 103, no. 7, pp. 0–5, 2008.

[91] J. Shoeb, M. M. Wang, and M. J. Kushner, "Damage by Radicals and Photons During Plasma Cleaning of Porous Low-k SiOCH. I. Ar/O_2 and He/H_2 plasmas," *J. Vac. Sci. Technol. A*, vol. 30, no. 4, 2012.

[92] J. Lee and D. B. Graves, "Synergistic Damage Effects of Vacuum Ultraviolet Photons and O2 in SiCOH Ultra-Low- k Dielectric Films," *J. Phys. D. Appl. Phys.*,

vol. 43, no. 42, p. 425201, 2010.

[93] E. Pargon, L. Azarnouche, M. Fouchier, K. Menguelti, R. Tiron, C. Sourd, and O. Joubert, "HBr Plasma Treatment Versus VUV Light Treatment to Improve 193 nm Photoresist Pattern Linewidth Roughness," *Plasma Process. Polym.*, vol. 8, no. 12, pp. 1184–1195, 2011.

[94] M. J. Titus, D. Nest, and D. B. Graves, "Absolute Vacuum Ultraviolet Flux in Inductively Coupled Plasmas and Chemical Modifications of 193 nm Photoresist," *Appl. Phys. Lett.*, vol. 94, no. 17, pp. 0–3, 2009.

[95] D. Nest, T. Y. Chung, D. B. Graves, S. Engelmann, R. L. Bruce, F. Weilnboeck, G. S. Oehrlein, D. Wang, C. Andes, and E. A. Hudson, "Understanding the Roughening and Degradation of 193 nm Photoresist During Plasma Processing: Synergistic Roles of Vacuum Ultraviolet Radiation and Ion Bombardment," *Plasma Process. Polym.*, vol. 6, no. 10, pp. 649–657, 2009.

[96] O. Auciello and D. L. Flamm, "Plasma Diagnostics, Volume 1: Discharge Parameters and Chemistry." Academic Press, Inc, New York, 1989.

[97] M. A. Lieberman and A. J. Lichtenberg, *Principles of Plasma Discharges and Materials Processing*. John Wiley & Sons, 2005.

[98] C. Steinbrüchel, "A New Method for Analyzing Langmuir Probe Data and the Determination of Ion Densities and Etch Yields in an Etching Plasma," *J. Vac. Sci. Technol. A Vacuum, Surfaces, Film.*, vol. 8, no. 3, p. 1663, 1990.

[99] M. Nakamura, K. Koshino, and J. Matsuo, "Mechanism of High Selectivity and Impurity Effects in HBr RIE: In-Situ Surface Analysis," *Jpn. J. Appl. Phys.*, vol.

31, no. 6S, p. 1999, 1992.

[100] T. D. Bestwick and G. S. Oehrlein, “Reactive Ion Etching of Silicon using Bromine Containing Plasmas,” *J. Vac. Sci. Technol. A,* vol. 8, no. 3, p. 1696, 1990.

[101] M. Haverlag, G. S. Oehrlein, and D. Vender, “Sidewall Passivation During the Etching of Poly-Si in an Electron Cyclotron Resonance Plasma of HBr,” *J. Vac. Sci. Technol. B,* vol. 12, no. 1, 1994.

[102] C. C. Cheng, K. V Guinn, and V. M. Donnelly, “Mechanism for Anisotropic Etching of Photoresist-masked, Polycrystalline Silicon in HBr Plasmas,” *J. Vac. Sci. Technol. B,* vol. 14, no. 1, 1996.

[103] C. Wang and V. M. Donnelly, “Effectiveness of dilute H_2 plasmas in removing boron from Si after etching of HfO_2 films in BCl_3 plasmas,” *J. Vac. Sci. Technol. A Vacuum, Surfaces, Film.,* vol. 24, no. 1, p. 41, 2006.

[104] A. Strass, W. Hansch, P. Bieringer, A. Neubecker, F. Kaesen, A. Fischer, and I. Eisele, “Etching Characteristics of Si and SiO_2 with a Low Energy Argon/Hydrogen D.C. Plasma Source,” *Surf. Coatings Technol.*, vol. 97, no. 1–3, pp. 158–162, 1997.

[105] A. P. Webb and S. Vepřek, “Reactivity of Solid Silicon with Hydrogen Under Conditions of a Low Pressure Plasma,” *Chem. Phys. Lett.*, vol. 62, no. 1, pp. 173–177, 1979.

[106] J. Abrefah and D. R. Olander, “Reaction of Atomic Hydrogen with Crystalline Silicon,” *Surf. Sci.*, vol. 209, no. 3, pp. 291–313, 1989.

[107] M. Ishii, K. Nakashima, I. Tajima, and M. Yamamoto, “Investigation of Hydrogen

Plasma Etched Si Surfaces," *Jpn. J. Appl. Phys.*, vol. 31, no. 12S, p. 4422, 1992.

[108] S. Veprek, C. Wang, and M. G. J. Veprek-Heijman, "Role of Oxygen Impurities in Etching of Silicon by Atomic Hydrogen," *J. Vac. Sci. Technol. A*, vol. 26, no. 3, 2008.

[109] A. Mitchell, R. A. Gottscho, S. J. Pearton, and G. R. Scheller, "Real-Time, Insitu Monitoring of GaAs and AlGaAs Photoluminescence During Plasma Processing," *Appl. Phys. Lett.*, vol. 56, no. 9, 1990.

[110] M. Taneya, Y. Sugimoto, and K. Akita, "Characterization of Subsurface Damage in GaAs Processed by Ga^+ Focused Ion-Beam-Assisted Cl_2 etching using photoluminescence," *J. Appl. Phys.*, vol. 66, no. 3, 1989.

[111] E. A. Ogryzlo, D. E. Ibbotson, D. L. Flamm, and J. A. Mucha, "Doping and Crystallographic Effects in Cl-Atom Etching of Silicon," *J. Appl. Phys.*, vol. 67, no. 6, 1990.

[112] J. R. Woodworth, M. E. Riley, V. A. Amatucci, T. W. Hamilton, and B. P. Aragon, "Absolute Intensities of the Vacuum Ultraviolet Spectra in Oxide Etch Plasma Processing Discharges," *J. Vac. Sci. Technol. A Vacuum, Surfaces, Film.*, vol. 19, no. 1, p. 45, 2001.

[113] B. E. A. Saleh, M. C. Teich, and B. E. Saleh, *Fundamentals of Photonics*, vol. 22. Wiley New York, 1991.

[114] S. O. Kasap, *Principles of Electronic Materials and Devices*. McGraw-Hill, 2006.

[115] J. M. Dorkel and P. Leturcq, "Carrier Mobilities in Silicon Semi-Empirically Related to Temperature, Doping and Injection Level," *Solid State Electron.*, vol.

24, no. 9, pp. 821–825, 1981.

[116] I. P. Herman, V. M. Donnelly, K. V. Guinn, and C. C. Cheng, “Laser-Induced Thermal Desorption as an In Situ Surface Probe During Plasma Processing,” *Phys. Rev. Lett.*, vol. 72, no. 17, pp. 2801–2804, Apr. 1994.

[117] S. Avasthi, G. Vertelov, J. Schwartz, and J. C. Sturm, “Reduction of Minority Carrier Recombination at Silicon Surfaces and Contacts Using Organic Heterojunctions,” *Conf. Rec. IEEE Photovolt. Spec. Conf.*, no. 1, pp. 001681–001685, 2009.

[118] W. Zhu, S. Sridhar, L. Liu, E. Hernandez, V. M. Donnelly, and D. J. Economou, “Photo-Assisted Etching of Silicon in Chlorine- and Bromine-Containing Plasmas,” *J. Appl. Phys.*, vol. 115, no. 20, 2014.

[119] N. C. M. Fuller, I. P. Herman, and V. M. Donnelly, “Optical Actinometry of Cl_2, Cl, Cl^+, and Ar^+ Densities in Inductively Coupled Cl_2–Ar Plasmas,” *J. Appl. Phys.*, vol. 90, no. 7, 2001.

[120] S. C. Deshmukh and D. J. Economou, “Factors Affecting the Cl Atom Density in a Chlorine Discharge,” *J. Appl. Phys.*, vol. 72, no. 10, pp. 4597–4607, 1992.

[121] A. R. Striganov and N. S. Sventitskii, *Tables of Spectral Lines of Neutral and Ionized Atoms*. Springer Science & Business Media, 2013.

[122] W. F. Meggers, B. F. Scribner, and C. H. Corliss, *Tables of Spectral Line Intensities*. US. Nat. Bureau Stand., 1975.

[123] C. Lee and M. A. Lieberman, “Global model of Ar, O_2, Cl_2, and Ar/O_2 high-density plasma discharges,” *J. Vac. Sci. Technol. A*, vol. 13, no. 2, p. 368, 1995.

[124] R. B. Bird, E. N. Lightfoot, and W. E. Stewart, *Transport Phenomena*. Wiley, 2002.

[125] T. Moore, B. Brady, and L. R. Martin, "Measurements and Modeling of SiCl4 Combustion in a Low-Pressure H2/O2 Flame," *Combust. Flame*, vol. 146, no. 3, pp. 407–418, 2006.

[126] G. Cunge, P. Bodart, M. Brihoum, F. Boulard, T. Chevolleau, and N. Sadeghi, "Measurement of Free Radical Kinetics in Pulsed Plasmas by UV and VUV Absorption Spectroscopy and by Modulated Beam Mass Spectrometry," *Plasma Sources Sci. Technol.*, vol. 21, no. 2, p. 024006, 2012.

[127] C. Lee, D. B. Graves, and M. A. Lieberman, "Role of Etch Products in Polysilicon Etching in a High-Density Chlorine Discharge," *Plasma Chem. Plasma Process.*, vol. 16, no. 1, pp. 99–120, Mar. 1996.

[128] G. Cunge, M. Kogelschatz, and N. Sadeghi, "Influence of Reactor Walls on Plasma Chemistry and on Silicon Etch Product Densities During Silicon Etching Processes in Halogen-based Plasmas," *Plasma Sources Sci. Technol.*, vol. 13, no. 3, p. 522, 2004.

[129] E. G. Thorsteinsson and J. T. Gudmundsson, "A Global (Volume Averaged) Model of a Chlorine Discharge," *Plasma Sources Sci. Technol.*, vol. 19, no. 1, p. 015001, 2009.

[130] E. G. Thorsteinsson and J. T. Gudmundsson, "A Global (Volume Averaged) Model of a Cl_2/Ar Discharge: I. Continuous Power," *J. Phys. D. Appl. Phys.*, vol. 43, no. 11, p. 115201, Mar. 2010.

[131] J. Guha, V. M. Donnelly, and Y.-K. Pu, "Mass and Auger Electron Spectroscopy Studies of the Interactions of Atomic and Molecular Chlorine on a Plasma Reactor Wall," *J. App. Phys.*, vol. 103, no. 1, p. 13306, 2008.

[132] V. M. Donnelly and M. V. Malyshev, "Diagnostics of Inductively Coupled Chlorine Plasmas: Measurements of the Neutral Gas Temperature," *Appl. Phys. Lett.*, vol. 77, no. 16, p. 2467, 2000.

[133] S. Kim, M. A. Lieberman, A. J. Lichtenberg, and J. T. Gudmundsson, "Improved Volume-Averaged Model for Steady and Pulsed-Power Electronegative Discharges," *J. Vac. Sci. Technol. A Vacuum, Surfaces, Film.*, vol. 24, no. 6, p. 2025, 2006.

[134] N. Layadi, V. M. Donnelly, and J. T. C. Lee, "Cl_2 Plasma Etching of Si(100): Nature of the Chlorinated Surface Layer Studied by Angle-Resolved X-Ray Photoelectron Spectroscopy," *J. Appl. Phys.*, vol. 81, no. 10, p. 6738, 1997.

[135] K. H. A. Bogart and V. M. Donnelly, "On the Constant Composition and Thickness of the Chlorinated Silicon Surface Layer Subjected to Increasing Etching Product Concentrations During Chlorine Plasma Etching," *J. Appl. Phys.*, vol. 86, no. 4, p. 1822, 1999.

[136] A. F. Molisch and B. P. Oehry, *Radiation trapping in atomic vapours*. Oxford University Press, 1998.

Appendices

Appendix A: Cl_2/Ar global model

A 0-D (global) model was developed based on the work of Gudmundsson et al. [129], [130] to calculate various plasma parameters by solving particle and energy balance equations described below. The global model assumes the plasma to be spatially homogenous, i.e. plasma parameters are volume averaged.

Particle Balance:

The particle balance equation for a species *X* in the plasma is given by

$$\frac{dn}{dt} = \sum R^X_{generation} - \sum R^X_{loss}, \tag{A-1}$$

where $R^X_{generation}$ and R^X_{loss} are the reaction rates of formation and loss of the species *X* [128]. The reaction rates are generally expressed as a product of the reaction rate constant *k* and the number density of each species involved in the reaction. Gudmundsson et al. [129], [130] expressed rate constants for various electron impact reactions (summarized in the table below) in Arrhenius form by integrating the collision cross sections ($\sigma(\varepsilon)$) over an assumed Maxwellian electron energy distribution function ($f(\varepsilon)$)

$$k(T_e) = \frac{2e}{m_e}\int_0^{\infty} \sigma(\varepsilon)\varepsilon^{0.5} f(\varepsilon) d\varepsilon, \tag{A-2}$$

where e is electronic charge, m_e is electron mass, T_e is electron temperature and ε is electron energy. The various plasma species included in the model are: neutral species (Cl, Cl_2, Ar), charged species (Cl^+, Cl_2^+, Ar^+, Cl^-, electrons), Ar metastables ($1s_5$ and $1s_3$),

excited argon Ar(4p) and radiative states of Ar ($1s_4$ and $1s_2$). The reaction set along with the corresponding rate constants used for Cl_2/Ar plasma is summarized below.

Reaction	**Rate constant (m^3s^{-1})**
$e + Cl_2 \rightarrow Cl + Cl + e$	$1.04 \times 10^{-13} T_e^{-0.29} e^{-8.84/T_e}$
$e + Cl_2 \rightarrow Cl_2^+ + 2e$	$5.12 \times 10^{-14} T_e^{0.48} e^{-12.34/T_e}$
$e + Cl_2 \rightarrow Cl + Cl^+ + 2e$	$2.14 \times 10^{-13} T_e^{-0.07} e^{-25.26/T_e}$
$e + Cl_2 \rightarrow Cl^+ + Cl^+ + 3e$	$2.27 \times 10^{-16} T_e^{-1.92} e^{-21.26/T_e}$
$e + Cl_2 \rightarrow Cl + Cl^-$	$3.43 \times 10^{-15} T_e^{-1.18} e^{-3.98/T_e} + 3.05 \times 10^{-16} T_e^{-1.33} e^{-0.11/(T_e+0.014)}$
$e + Cl_2 \rightarrow Cl^+ + Cl^- + e$	$2.94 \times 10^{-16} T_e^{-0.19} e^{-18.79/T_e}$
$e + Cl_2^+ \rightarrow Cl + Cl$	$9.0 \times 10^{-14} T_e^{-0.5}$
$e + Cl \rightarrow Cl^+ + 2e$	$3.17 \times 10^{-14} T_e^{0.53} e^{-13.29/T_e}$
$e + Cl^- \rightarrow Cl + 2e$	$9.02 \times 10^{-15} T_e^{0.92} e^{-4.88/T_e}$
$e + Cl^- \rightarrow Cl^+ + 3e$	$3.62 \times 10^{-15} T_e^{0.72} e^{-25.38/T_e}$
$Cl_2 + Cl^+ \rightarrow Cl + Cl_2^+$	5.4×10^{-16}
$e + Ar \rightarrow Ar^+ + 2e$	$2.39 \times 10^{-14} T_e^{0.57} e^{-17.43/T_e}$
$e + Ar^m \rightarrow Ar^+ + 2e$	$2.71 \times 10^{-13} T_e^{0.26} e^{-4.59/T_e}$
$e + Ar^r \rightarrow Ar^+ + 2e$	$2.7 \times 10^{-13} T_e^{0.29} e^{-4.24/T_e}$
$e + Ar \rightarrow Ar^m + e$	$9.73 \times 10^{-16} T_e^{-0.07} e^{-11.69/T_e}$
$e + Ar \rightarrow Ar^r + e$	$3.93 \times 10^{-15} T_e^{0.46} e^{-12.09/T_e}$
$e + Ar \rightarrow Ar^{4p} + e$	$8.91 \times 10^{-15} T_e^{-0.04} e^{-14.18/T_e}$
$e + Ar^{4p} \rightarrow Ar^+ + 2e$	$1.09 \times 10^{-12} T_e^{0.29} e^{-3.42/T_e}$
$e + Ar^m \rightarrow Ar^{4p} + e$	$2.39 \times 10^{-12} T_e^{-0.15} e^{-1.82/T_e}$
$e + Ar^m \rightarrow Ar^r + e$	3.7×10^{-13}
$e + Ar^r \rightarrow Ar^m + e$	9.1×10^{-13}
$Ar^m + Ar^m \rightarrow Ar + Ar$	2×10^{-13}
$Ar^r + Ar^m \rightarrow Ar + Ar^+ + e$	2.1×10^{-15}
$Ar(4p) + Ar(4p) \rightarrow Ar + Ar^+ + e$	5.0×10^{-16}
$Ar^m + Ar^m \rightarrow Ar + Ar^+ + e$	6.4×10^{-16}
$Ar^r \rightarrow Ar + h\nu$	$1 \times 10^5 s^{-1}$

Reaction	**Rate constant (m^3s^{-1})**
$Ar(4p) \rightarrow Ar + h\nu$	$3.2 \times 10^7 s^{-1}$
$Ar(4p) \rightarrow \{Ar^m, Ar^r\} + h\nu$	$3.0 \times 10^7 s^{-1}$
$Cl_2 + Ar^+ \rightarrow Cl_2^+ + Ar$	1.9×10^{-16}
$Cl_2 + Ar^+ \rightarrow Cl + Cl^+ + Ar$	5.7×10^{-16}
$Cl^- + Ar^+ \rightarrow Cl + Ar$	$5.0 \times 10^{-14}(300/T_g)^{0.5}$
$Cl_2 + \{Ar^m, Ar^r, Ar(4p)\} \rightarrow Cl_2^+ + Ar + e$	7.1×10^{-16}

Neutral chlorine atoms diffuse and stick to chamber walls where they can recombine with another atom. The rate coefficient for diffusional loss is given by equation 5.3. The values for recombination coefficient (γ_{rec}) was taken from published experimental values as a function of Cl:Cl_2 number density ratio [131].

Malyshev and Donnelly measured neutral gas temperatures as a function of plasma power and pressure in a chlorine and argon plasmas [132]. Gas temperatures used in the simulation were obtained through a pressure (p) and power (P_{abs}) dependent fit of experimental measurements [129]

$$T_g(P_{abs}, p) = 300 + (1250(1 - e^{-0.091p}) + 400e^{-0.337p})\frac{log_{10}(P_{abs}/40)}{log_{10}40}. \quad \text{(A-3)}$$

The ion temperature (T_i) was calculated by setting the ion temperature equal to 0.5 eV at 1 mTorr and decreasing the ion temperature (relative to thermal temperature) at a rate proportional to $1/p$ [123].

Power Balance:

The power balance equation is given by

$$V\frac{d}{dt}\left(\frac{3}{2}en_eT_e\right) = P_{abs} - eVn_e\sum n^X\epsilon_c^X k_{iz}^X - eu_bn_iA_{eff}(\in_i+\in_c), \quad \text{(A-4)}$$

where P_{abs} is the power delivered to the plasma, n^X is the number density of neutral species, V is the chamber volume, n_e is electron density, u_b is the Bohm velocity, $\in_c^X$ is the collisional energy loss during creation of an electron-ion pair, $\in_i = V_{plasma} + V_{sheath}$ is the mean kinetic energy lost per ion lost to the walls, and $\in_c = 2T_e$ is the mean electron energy lost per electron lost to walls [128]. For chlorine containing plasmas, electronegativity ($\alpha = n^-/n_e$) is often larger than unity. Various formulae used to calculate plasma parameters have to be modified to include this factor. The Bohm velocity is calculated by

$$u_b = \left[\frac{eT_e(1+\alpha_s)}{m_i(1+\alpha_s\gamma_-)}\right]^{0.5}, \quad \text{(A-5)}$$

where α_s is the electronegativity at the sheath edge, γ_- is the ratio of electron temperature to ion temperature, and m_i is ion mass [97]. α_s is obtained by solving the non-linear equation shown below [97]

$$\frac{\alpha_s}{\alpha_b} = exp\left[\frac{(1+\alpha_s)(1-\gamma_-)}{2(1+\alpha_s\gamma_-)}\right]. \quad \text{(A-6)}$$

The plasma potential (V_{plasma}) is calculated as [97]

$$V_{plasma} = \frac{1}{2}\frac{1+\alpha_s}{1+\alpha_s\gamma_-}T_e\,. \quad \text{(A-7)}$$

Plasma quasi neutrality requires the positive ion flux to the walls to match the sum of negative ion and electron fluxes [97] , i.e.,

$$\sum n_{+s}\,u_b = \sum 0.25n_{-s}v_-\exp\left(\frac{\gamma_-V_{sheath}}{T_e}\right) + 0.25n_{es}v_e exp\left(\frac{V_{sheath}}{T_e}\right), \quad \text{(A-8)}$$

where v denotes mean thermal velocity, and the subscript "s" denotes sheath edge. This

equation can then be solved to obtain the sheath potential (V_{sheath}). The edge to center positive ion density ratio (wall loss factor) can be used to calculate the density of positive ions near the sheath edge. A modified expression for the loss factors which included the effect of plasma electronegativity was proposed by Kim et al. [133]

$$h_l = \left[\left(\frac{0.86}{\left(3+{}^{L}/_{2\lambda}\right)^{0.5}(1+\alpha_0)}\right)^2 + {h_c}^2\right]^{0.5} \text{ and} \tag{A-9}$$

$$h_R = \left[\left(\frac{0.8}{\left(4+{}^{R}/_{\lambda}\right)^{0.5}(1+\alpha_0)}\right)^2 + {h_c}^2\right]^{0.5}, \tag{A-10}$$

where λ is ion mean free path. The terms h_c and n_* are given by

$$h_c \cong \frac{1}{\gamma_-^{0.5}+\gamma_+^{0.5}\left[n_*^{0.5}n_+/n_-^{0.5}\right]} \text{ and} \tag{A-11}$$

$$n_* = 0.63 \times {}^{v_i}/_{k_{rec}\lambda}\,, \tag{A-12}$$

where $k_{rec} = 5\times10^{-14}\,(300/T_g)^{0.5}$, and v_i is the ion mean thermal velocity.

Appendix B: XPS analysis of the chlorinated surface layer

X-ray photoelectron spectroscopy has been used to study the nature of chlorinated surface of silicon etched by energetic ion bombardment [134], [135]. Similarly, the chlorinated surface layer formed during photo assisted etching can also be studied using XPS. The surface chemical composition of Si can give clues about probable surface reactions that occur during photo-assisted etching.

In a preliminary study, Si was etched in a Cl_2 plasma at 350W with applied RF substrate bias (V_{DC} = -70V) for 60 seconds. Two reactor configurations were used for etching, in which the position of the Si sample with respect to the plasma was different: (a) the sample was immersed into the plasma, and (b) sample was placed about 12 cm downstream from the lower edge of the plasma. Survey spectra of the sample etched using reactor (a) revealed lower chlorine coverage: ~ 14% Cl on the surface, compared to over 24% Cl for sample etched in reactor (b). High resolution spectra of the Si 2p peak (binding energy ~ 99eV) showed a pronounced tail towards the higher binding energy side of the Si 2p peak for the sample etched in reactor (b). The high resolution spectra of the sample etched in reactor (b) were deconvoluted to identify the various silicon chlorides. A Shirley shaped background was subtracted and 4 sets of two peaks (to account for the Si $2p_{1/2}$ spin orbit component) were used to fit the spectrum. Deconvolution shows peaks at 100.3, 101.2, 102.2 eV corresponding to SiCl, $SiCl_2$, and $SiCl_3$ in addition to the bulk Si peak at 99.5 eV. This is in contrast to the sample etched in reactor (a) which contained only SiCl and no other chlorides.

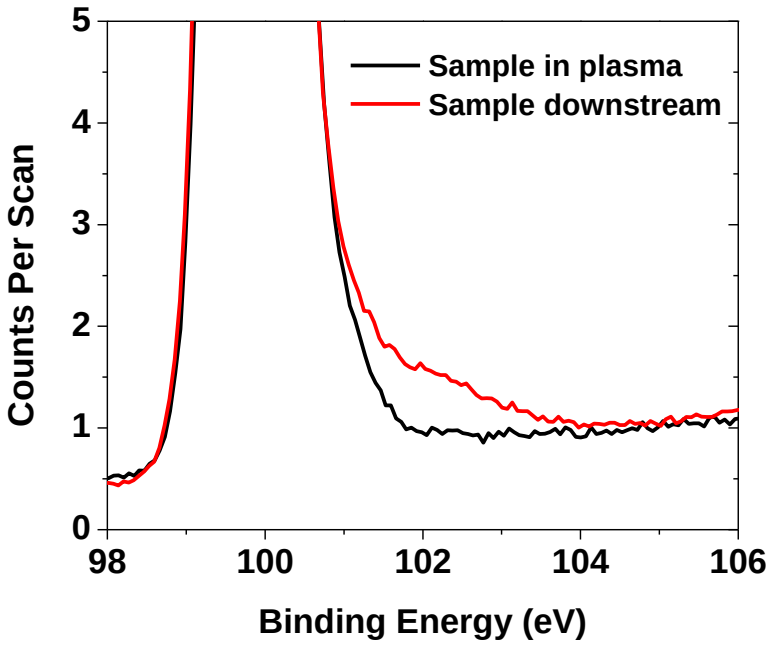

Figure B-1: Si (2p) High resolution spectra of samples etched in a Cl2 plasma (a) sample is placed in the plasma, and (b) sample is placed downstream of the plasma.

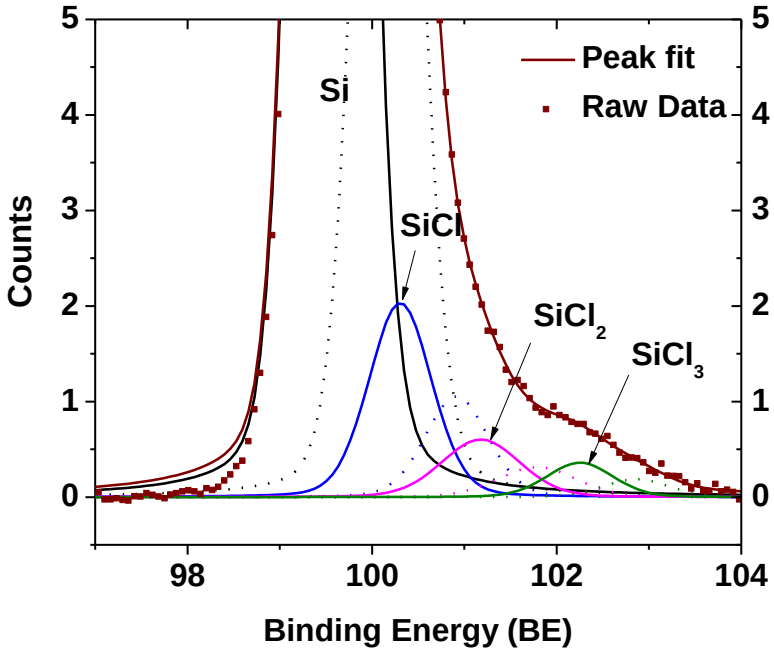

Figure B-2: High resolution peak fitting of Si (2p) spectrum for the sample etched in reactor (b)

The difference in the XPS spectrum can be due the effect of photons. For sample etched in reactor (a), it is possible that the photons are very efficient in altering the surface chemistry due to the proximity of the sample to the light source. As the sample is etched at some distance away from the plasma (reactor (b)), it is likely that the photon is absorbed by another atom/molecule in the gas phase. VUV photons are emitted as a result of resonant electronic transitions from a high energy state to the ground state. Such photons have just the right energy to induce the opposite transition, i.e. excite a ground state atom to a high energy state. Thus, the photon can be easily reabsorbed by other ground state atoms. The process of emission, absorption and re-emission continues several times before the photon finally escapes. This process is referred to as "radiation trapping" [136]. Radiation trapping can lead to longer "lifetimes" for the photon to escape gas phase and reach the substrate. If photons are effectively trapped and very few photons make it to the surface, then photo-assisted etching could be negligible when the sample is downstream of the plasma. The high resolution spectrum of sample etched in reactor (b) is quite similar to that observed for ion assisted etching in a similar reactor configuration [134].

More work needs to be done to separate the effects of simultaneous photon irradiation and ion bombardment on surface chemistry. For example, the ions can be completely blocked from reaching the surface by using a set of grids above the substrate. The grids can be biased such that it repels all the ions and prevents it from reaching the substrate. This would conclusively show the effect of photon irradiation alone (no ion bombardment) on the surface chemistry.